Collisional Mechanics in Solid-Liquid Flows

Thesis by

José Roberto Zenit Camacho

In Partial Fulfillment of the Requirements

for the Degree of

Doctor of Philosophy

California Institute of Technology

Pasadena, California

1998

(Submitted October 3, 1997)

Acknowledgements

I would like to express my deepest gratitude to Professor Melany Hunt for being a great advisor. I am fortunate to have had the opportunity to work for the group under her supervision. Her guidance, encouragement and understanding were essential during my entire graduate life. I immensely thank Professor Chris Brennen for his mentorship. His example and advice were of great importance to me. I am grateful to Professor Charlie Campbell. His willingness to discuss my projects and other topics was of invaluable help. I would like to acknowledge Professors John Brady and Ron Scott for serving in my thesis committee and for their helpful suggestions. I thank the people in the granular flows group for their great help, immense patience and true friendship: Carl Wassgren, Anna Karion, Venkata Natarajan and Douglas Varela. My gratitude to Robert Uy, Yi-Chun Wang, Clancy Rowley and Chantal Morgan for their help in the lab, in the office, and during the writing of my thesis.

I am thankful to the National Council for Science and Technology of Mexico (CONACyT) for initially granting me a full scholarship to come to Caltech and for the continued support during the pursuit of my graduate studies.

I am grateful to Professor Baltasar Mena for initiating me into a career in science. His encouragement and advice were of great value before and during my graduate studies. I thank Professor Francisco Ávila for his encouragement during my studies.

I cannot enumerate here the long list of great friends and coworkers who made my stay in Caltech pleasant and unforgettable. I thank them all, truly from the bottom of my heart.

I dedicate this work to my parents. Dedico este trabajo a mis padres. Gracias por todo.

Abstract

Experimental measurements of the particle pressure were obtained for a liquid fluidized bed and for a vertical gravity driven liquid-solid flow. The particle, or granular, pressure is defined as the extra pressure generated by the action of particles in a particulate multi-phase flow. Using a high-frequency-response pressure transducer, individual collisions of particles were collected and measured to obtain a time-averaged particle pressure. Results were obtained for a number of different particles and for two different test section diameters. Results show that the particle pressure experiences a maximum at intermediate concentrations, and that its magnitude is scaled with the particle density and the square of the terminal velocity of the particles. The particle pressure was found to be composed of two main contributions: one from pressure pulses generated by direct collisions of particles against the containing walls (direct component), and a second one from pressure pulses due to collisions between individual particles that are transmitted through the liquid (radiated component).

The direct component of the particle pressure was studied by an analysis of particle collisions submerged in a liquid. A simple pendulum experiment provides controlled impacts in which measurements are made of the particle trajectories for different particles immersed in water. The velocity of the approaching particle is measured using a high speed digital camera; the magnitude of the collision is quantified using a high frequency response pressure transducer at the colliding surface. The measurements show that most of the particle deceleration occurs at less than half a particle diameter away from the wall. The measured collision pressure appears to increase with the impact velocity. Comparisons are drawn between the measured pressures and the predictions by Hertzian theory. A simple control-volume model is proposed to account for the effects of fluid inertia and viscosity. The pressure profile is estimated, and then integrated over the surface of the particle to obtain a force. The model predicts a critical Reynolds number at which the particle reaches the wall with zero velocity.

Comparisons between the proposed model and the experimental measurements show qualitative agreement.

Experiments involving binary collisions of particles were performed to investigate the radiated component of the particle pressure. This component results from the pressure front generated by the impulsive motion of a fluid resulting from a collision of particles in a liquid. When the two particles come into contact, the impulsive acceleration due to the elastic rebound produces a pressure pulse, which is transmitted through the fluid. A simple dual pendulum experiment was set up to generate controlled collisions. Measurements were obtained for a range of impact velocities, angles of incidence, and distances away from the wall for different pairs of particles. The magnitude of the impulse pressure appears to scale with the particle impact velocity and the density of the fluid. Based on the impulse pressure theory, a prediction for pressure generated due to the collision can be obtained. The model appears to agree well with the experimental measurements.

The fluctuating component of the solid fraction was studied, as one of the sources of the particle pressure. The instantaneous cross-sectional averaged solid fraction was measured using an impedance meter. The root-mean square fluctuation of the solid fraction signal was measured in a liquid fluidized bed and a vertical gravity-driven flow, for different particle sizes and densities. Two types of fluctuations were identified: low-frequency large-scale fluctuations which dominate at high concentrations, and high-frequency small-scale fluctuations which are dominant at intermediate solid fractions. The effect of each type was isolated by filtering. When the large-scale fluctuations were present, the magnitude of the rms fluctuation was found to scale with particle diameter, but when eliminated the mean fluctuation appeared to scale with the particle mass instead.

Contents

Acknowledgements iii

Abstract iv

1 Introduction 1

1.1 Motivation and general background 1

1.2 Complexity of multi-phase flows, the coupling of the phases 2

1.3 Modeling of solid-liquid flows 3

1.4 Thesis outline 4

2 Particle pressure in liquid-solid flows 6

2.1 Introduction 6

2.1.1 Particle pressure models 7

2.2 Experimental setup 11

2.3 Results 18

2.3.1 Liquid fluidized bed experiments 18

2.3.2 Vertical gravity driven flow 24

2.4 Discussion 27

2.5 Comparison with existing models 29

2.6 Probability density functions 33

2.6.1 PDF for other particles 37

2.7 Components of the collisional particle pressure 47

3 Mechanics of immersed particle collisions 54

3.1 Introduction 54

3.1.1 The impact paradox 55

3.2 Experimental measurement of immersed collision properties 56

3.2.1 Experimental setup 57
3.3 Particle-wall collisions 62
3.3.1 Approach velocities 62
3.3.2 Rebound and coefficient of restitution 64
3.3.3 Collision impulses 71
3.4 Modeling 74
3.4.1 Results of the model 79
3.4.2 Comparisons with experiments 83
3.5 Binary collisions 84

4 Liquid pressure front generated by particle-particle collisions 90
4.1 Introduction 90
4.1.1 Pressure-impulse theory 91
4.2 Experimental setup 94
4.3 Results 99
4.4 Comparisons with impulse-pressure theory 105
4.5 Discussion 109

5 Solid fraction fluctuations in liquid-solid flows 112
5.1 Introduction 112
5.1.1 Modeling random fluctuations in liquid-solid flows 113
5.2 Experiments 114
5.3 Results 117
5.3.1 Liquid fluidized beds 117
5.3.2 Vertical gravity driven flow 124
5.4 Low and high frequency fluctuations 126
5.5 Comparisons 127
5.6 Discussion 129

6 Conclusions 134
6.1 Summary of results 134

6.2 Comments on general issues 138

Bibliography **140**

List of Figures

2.1 Typical pressure pulse generated by a particle collision. 12

2.2 Experimental setup. 13

2.3 Experimental setup, instrumentation. 14

2.4 Calibration of the pressure transducer. Direct comparison of experimental collision in air (o) against Hertzian prediction (−). u_i =75 mm/s. 18

2.5 Calibration of the pressure transducer. Impact pressure as a function of impact velocity and particle diameter. Experimental (in air): (×) 3 mm glass bead, (∗) 4.2 mm glass bead. Hertzian predictions: 2 mm glass bead = · · ·, 3 mm glass bead = − − , 4.2 mm glass bead = − · −. 19

2.6 Calibration of the pressure transducer. Duration of collision as a function of impact velocity and particle diameter. Experimental (in air): (×) 3 mm glass bead, (∗) 4.2 mm glass bead. Hertzian predictions: 2 mm glass bead = · · ·, 3 mm glass bead = − − , 4.2 mm glass bead = − · −. 19

2.7 Particle pressure P_p as a function of the solid fraction ν for fluidized glass particles in the 5.1 cm test section. 20

2.8 Particle pressure P_p as a function of the superficial fluid velocity u_s for fluidized glass particles in the 5.1 cm test section. 21

2.9 Calculated impact velocity u_i, normalized by u_t, as a function of the solid fraction ν for fluidized glass particles in the 5.1 cm test section. For symbol identification see Table 1. 22

2.10 Particle pressure P_p as a function of the solid fraction ν. A comparison of the pressures measured in a 10.2 cm test section (TS) and a 5.1 cm TS. Fluidized glass particles. For symbol identification see Table 1. . 23

2.11 Calculated impact velocity u_i, normalized by u_t, as a function of the solid fraction ν. A comparison of the calculated impact velocities in a 10.2 cm test section (TS) and a 5.1 cm TS. Fluidized glass particles. For symbol identification see Table 1. 23

2.12 Particle pressure P_p as a function of the solid fraction ν. A comparison of particles with different densities for fluidized steel and glass particles in the 5.1 cm test section. 24

2.13 Particle pressure P_p as a function of the solid fraction ν. A comparison of particles with different densities for fluidized plastic and glass particles in the 10.2 cm test section. 25

2.14 Particle pressure P_p as a function of the solid fraction ν. Vertical gravity driven flow of 3 mm glass particles. $\times$ cocurrent flow in 5.1 cm TS, $*$ countercurrent flow in 5.1 cm TS. $\otimes$ cocurrent flow in 10.2 cm TS, $+$ countercurrent flow in 10.2 cm TS. 26

2.15 Calculated impact velocity u_i, normalized by u_t, as a function of the solid fraction ν. Vertical gravity driven flow of 3 mm glass particles. $\times$ cocurrent flow in 5.1 cm TS, $*$ countercurrent flow in 5.1 cm TS. $\otimes$ cocurrent flow in 10.2 cm TS, $+$ countercurrent flow in 10.2 cm TS. . 26

2.16 Non-dimensional particle pressure $\hat{P}_p$ as a function of solid fraction ν. Pressures normalized by $\frac{1}{2}\rho_p u_t^2$. Results for all particles and tests sections in a fluidized bed. 28

2.17 Comparison of the experimental results with theoretical models. Experimental results for 3 mm glass particles in a fluidized bed: $\times$. Pressures normalized by $\frac{1}{2}\rho_p u_t^2$. 30

2.18 Comparison of the experimental results with theoretical models. Experimental results for 3 mm glass particles in a fluidized bed: $\times$. Pressures normalized by $\frac{1}{2}\rho_p u_t^2$. 30

2.19 Probability density function of individual collision pressure. Fluidized glass 3 mm particles in a 10.2 cm test section. $(—)$ $\nu = 0.503, (--)$ $\nu = 0.438, (- \cdot -)$ $\nu = 0.318, (\cdots)$ $\nu = 0.194$. 34

2.20 Probability density function of collision duration. Fluidized glass 3 mm particles in a 10.2 cm test section. (—) $\nu = 0.503$, (– –) $\nu = 0.438$, (– · –) $\nu = 0.318$, (· · ·) $\nu = 0.194$. 35

2.21 Probability density function of collision impulse. Fluidized glass 3 mm particles in a 10.2 cm test section. (—) $\nu = 0.503$, (– –) $\nu = 0.438$, (– · –) $\nu = 0.318$, (· · ·) $\nu = 0.194$. 36

2.22 Probability density function of individual collision pressure. Fluidized glass 2 mm particles in a 10.2 cm test section. (—) $\nu = 0.4435$, (– –) $\nu = 0.327$, (– · –) $\nu = 0.243$, (· · ·) $\nu = 0.181$. 37

2.23 Probability density function of collision duration. Fluidized glass 2 mm particles in a 10.2 cm test section. (—) $\nu = 0.4435$, (– –) $\nu = 0.327$, (– · –) $\nu = 0.243$, (· · ·) $\nu = 0.181$. 38

2.24 Probability density function of collision impulse. Fluidized glass 2 mm particles in a 10.2 cm test section. (—) $\nu = 0.4435$, (– –) $\nu = 0.327$, (– · –) $\nu = 0.243$, (· · ·) $\nu = 0.181$. 38

2.25 Probability density function of individual collision pressure. Fluidized glass 4 mm particles in a 10.2 cm test section. (—) $\nu = 0.481$, (– –) $\nu = 0.361$, (– · –) $\nu = 0.251$, (· · ·) $\nu = 0.115$. 39

2.26 Probability density function of collision duration. Fluidized glass 4 mm particles in a 10.2 cm test section. (—) $\nu = 0.481$, (– –) $\nu = 0.361$, (– · –) $\nu = 0.251$, (· · ·) $\nu = 0.115$. 40

2.27 Probability density function of collision impulse. Fluidized glass 4 mm particles in a 10.2 cm test section. (—) $\nu = 0.481$, (– –) $\nu = 0.361$, (– · –) $\nu = 0.251$, (· · ·) $\nu = 0.115$. 40

2.28 Probability density function of individual collision pressure. Fluidized steel 4.5 mm particles in a 5.1 cm test section. (—) $\nu = 0.568$, (– –) $\nu = 0.455$, (– · –) $\nu = 0.350$, (· · ·) $\nu = 0.172$. 41

2.29 Probability density function of collision duration. Fluidized steel 4.5 mm particles in a 5.1 cm test section. (—) $\nu = 0.568$, (– –) $\nu = 0.455$, (– · –) $\nu = 0.350$, (· · ·) $\nu = 0.172$. 42

2.30 Probability density function of collision impulse. Fluidized steel 4.5 mm particles in a 5.1 cm test section. (—) $\nu = 0.568$, (– –) $\nu = 0.455$, (– · –) $\nu = 0.350$, (· · ·) $\nu = 0.172$. 42

2.31 Probability density function of individual collision pressure. Fluidized nylon 6.35 mm particles in a 10.2 cm test section. (—) $\nu = 0.589$, (– –) $\nu = 0.434$, (– · –) $\nu = 0.2237$, (· · ·) $\nu = 0.134$. 43

2.32 Probability density function of collision duration. Fluidized nylon 6.35 mm particles in a 10.2 cm test section. (—) $\nu = 0.589$, (– –) $\nu = 0.434$, (– · –) $\nu = 0.2237$, (· · ·) $\nu = 0.134$. 44

2.33 Probability density function of collision impulse. Fluidized nylon 6.35 mm particles in a 10.2 cm test section. (—) $\nu = 0.589$, (– –) $\nu = 0.434$, (– · –) $\nu = 0.2237$, (· · ·) $\nu = 0.134$. 44

2.34 Probability density function of individual collision pressure. Fluidized PVC 3.4 mm rods in a 10.2 cm test section. (—) $\nu = 0.444$, (– –) $\nu = 0.341$, (– · –) $\nu = 0.2945$, (· · ·) $\nu = 0.771$. 45

2.35 Probability density function of collision duration. Fluidized PVC 3.4 mm rods in a 10.2 cm test section. (—) $\nu = 0.444$, (– –) $\nu = 0.341$, (– · –) $\nu = 0.2945$, (· · ·) $\nu = 0.771$. 45

2.36 Probability density function of collision impulse. Fluidized PVC 3.4 mm rods in a 10.2 cm test section. (—) $\nu = 0.444$, (– –) $\nu = 0.341$, (– · –) $\nu = 0.2945$, (· · ·) $\nu = 0.771$. 46

2.37 Particle pressure as a function of solid fraction, a comparison between the total particle pressure (—) and the particle pressure generated solely by the long duration collisions (– –). Fluidized glass 3 mm particles in the 10.2 cm test section. 47

2.38 Schematic of experimental setup used to obtain the images of the moving particles and pressure pulses simultaneously. 49

2.39 Sequence of images of pressure transducer obtained through view window. A typical long duration pressure pulse: a direct collision of a particle on the surface of the transducer. 3 mm glass fluidized particles in 5.1 cm test section. $\nu \approx 0.05$. 50

2.40 Sequence of images of pressure transducer obtained through view window. A typical short duration pressure pulse: impulsive acceleration of a particle near the transducer. 3 mm glass fluidized particles in 5.1 cm test section. $\nu \approx 0.05$. Note that at zero time the particle is not in contact with the transducer. 52

2.41 Types of pressure pulses that contribute to the particle pressure. Sketch of the collisions and type of pressure pulse recorded. The solid arrows represent the motion before contact, and the dashed arrows, the motion after contact. 53

3.1 Experimental setup. 58

3.2 Typical collision (picture). 4.5 mm steel particle in water. Only approach shown. 58

3.3 Typical collision (pressure pulse). 4.5 mm steel particle in water. . . . 59

3.4 Comparison of the phase plot predicted by Mei (1994) and experimental measurements. 61

3.5 Comparison of the pressure pulse generated by a steel particle with the prediction from Hertzian theory. Data for a 4.5 mm steel particle, immersed in water. 62

3.6 Phase plot for a 6 mm glass particle immersed in water. (+) $\theta_i = 16^o$; ($\times$) $\theta_i = 12^o$. 63

3.7 Phase plot for a 4.5 mm steel particle immersed in water. (+) $\theta_i = 13.7^o$; ($\times$) $\theta_i = 8.5^o$. 64

3.8 Phase plot for a 6.4 mm nylon particle immersed in water. (+) $\theta_i = 18.5^o$. ($\times$) $\theta_i = 13.5^o$. 65

3.9 Typical time history of a 6 mm glass particle position colliding and rebounding against a flat surface, immersed in water. 66
3.10 Typical time history of a 6 mm glass particle velocity colliding and rebounding against a flat surface, immersed in water. 67
3.11 Particle position and velocity as a function of time for a 4.5 mm steel particle in water, for various initial release angles. 67
3.12 Particle position and velocity as a function of time for a 6 mm glass particle in water, for various initial release angles. 68
3.13 Particle position and velocity as a function of time for a 4 mm glass particle in water, for various initial release angles. 69
3.14 Particle position and velocity as a function of time for a 3 mm glass particle in water for various initial angles of release. 70
3.15 Particle position as a function of time for a 6.35 mm nylon particle in water for various initial angles of release. 71
3.16 Plot of the total coefficient of restitution, ϵ_{tot} as a function of impact velocity, for all particles. See Table 3.1 for symbol identification. . . . 72
3.17 Plot of the contact coefficient of restitution, ϵ_{con} as a function of impact velocity, for all particles. See Table 3.1 for symbol identification. . . . 72
3.18 Measured collision impulse as a function of impact velocity. Glass particles in water. The dashed lines represent the Hertzian theory prediction. 73
3.19 Measured collision impulse as a function of impact velocity. Steel, nylon and glass particles in water. The dashed lines represent the Hertzian theory prediction. 74
3.20 Normalized collision impulses as a function of predicted impact velocity. 75
3.21 Schematic of the problem and coordinate system. 76
3.22 Control volume : Momentum and mass fluxes. 77
3.23 Phase plot of non-dimensional velocity vs. non-dimensional distance, inviscid case. 80

3.24 Phase plot of non-dimensional velocity vs. non-dimensional distance, viscous case for a density ratio of 2.5 ($C_o = 0.04$). 81

3.25 Critical Reynolds number Re_c as a function of the density ratio, ρ_p/ρ_f, for different values of the proportionality constant C_o. 82

3.26 Critical Reynolds number Re_c as a function of the Stokes number, St_p, for different values of the proportionality constant C_o. 82

3.27 Collisional Impulse as a function of predicted impact velocity. Comparison between the 6 mm glass particle experimental measurements and the predictions from the model for different values of the proportionality constant C_o. 84

3.28 Collisional Impulse as a function of predicted impact velocity. Comparison between the 4.5 steel particle experimental measurements and the predictions from the model for different values of the proportionality constant C_o. 85

3.29 Typical time history of the position of two 6 mm glass particles undergoing a binary collision immersed in water. 86

3.30 Typical time history of the velocity of two 6 mm glass particles undergoing a binary collision immersed in water. $\epsilon_{bin} = 0.52$, $(u_i)_o = 88mm/s$. 87

3.31 Typical time history of the velocity of two 4 mm glass particles undergoing a binary collision immersed in water. $\epsilon_{bin} = 0.10$, $(u_{imp})_a = 78mm/s$. 88

3.32 Typical time history of the velocity of two 3 mm glass particles undergoing a binary collision immersed in water. $\epsilon_{bin} = 0.01$, $(u_{imp})_a = 25mm/s$. 88

3.33 Typical time history of the velocity of two 4.5 mm steel particles undergoing a binary collision immersed in water. $\epsilon_{bin} = 0.43$, $(u_{imp})_a = 116mm/s$. 89

3.34 Typical time history of the velocity of two 6.35 mm nylon particles undergoing a binary collision immersed in water. $\epsilon_{bin} = 0.37$, , $(u_{imp})_a = 20mm/s$. 89

4.1 Schematic of the impulsive motion of a sphere near a wall in an inviscid irrotational flow. 93

4.2 Impulse distribution for different b/d ratios. The impulse is normalized by $\rho_f u_\tau d$. 95

4.3 Impulse distribution for different angles of incidence ϕ, for $b/d = 1.5$ 96

4.4 Experimental setup of the dual pendulum to measure the impulse pressure produced by a collision. 97

4.5 Typical pressure pulse impulse pressure produced by a collision of two 4.5 mm steel particles in water. 98

4.6 Measured impulse-pressure as a function of normalized distance from the wall, b/d. Acceleration of the particle produced by the collision of a particle of the same diameter and density. 6 mm glass particles immersed in water. Velocity of the target particle after impact $\approx$ 0.0704 m/s. 100

4.7 Measured maximum pressure as a function of normalized distance from the wall, b/d. Acceleration of the particle produced by the collision of a particle of the same diameter and density. 6 mm glass particles immersed in water. Velocity of the target particle after impact $\approx$ 0.0704 m/s. 101

4.8 Measured pressure pulse duration as a function of normalized distance from the wall, b/d. Acceleration of the particle produced by the collision of a particle of the same diameter and density. 6 mm glass particles immersed in water. Velocity of the target particle after impact ≈ 0.0704 m/s. 101

4.9 Measured impulse pressure as a function of impact velocity. Distance from the wall, $b/d = 0.625$. 6 mm glass particles immersed in water. The solid line shows the power law fit of the data. 102

4.10 Measured impulse pressure as a function of incidence angle ϕ. Distance from the wall, $b/d = 0.65$, and impact velocity = 0.1093 m/s. 6 mm glass particles immersed in water. The solid line shows the best fit of the data. 103

4.11 Comparison of the measured impulse-pressure as a function of normalized distance from the wall, b/d, for different diameter glass particles immersed in water: 6 mm glass ($\circ$), $u_\tau = 0.0704$ m/s; 4.1 mm glass ($*$), $u_\tau = 0.0596$ m/s; 3 mm glass ($\times$), $u_\tau = 0.0544$ m/s. 104

4.12 Comparison of the measured impulse-pressure as a function of normalized distance from the wall, b/d, for different density particles immersed in water: 4.1 mm glass ($*$), $u_\tau = 0.0596$ m/s; 4.5 mm steel ($\oplus$), $u_\tau = 0.0934$ m/s; 6.35 mm nylon ($\otimes$), $u_\tau = 0.0249$ m/s. 105

4.13 Comparison of the normalized impulse-pressure, $\hat{I}$, as a function of normalized distance from the wall, b/d, for all tested particles. 6 mm glass ($\circ$), $u_\tau = 0.070$ m/s; 4.1 mm glass ($*$), $u_\tau = 0.059$ m/s; 3 mm glass ($\times$), $u_\tau = 0.054$ m/s; 4.5 mm steel ($\oplus$), $u_\tau = 0.093$ m/s; 6.25 mm nylon ($\otimes$), $u_\tau = 0.025$ m/s. 106

4.14 Comparison between theory and experiments of the normalized impulse-pressure, $\hat{I}$, as a function of normalized distance from the wall, b/d. 6 mm glass ($\circ$), $u_\tau = 0.0704$ m/s. Equation 4.9 ($- - -$); equation 4.11 ($- \cdot -$). 107

4.15 Comparison between theory and experiments of the normalized impulse-pressure, $\hat{I}$, as a function of angle of incidence ϕ. 6 mm glass ($\circ$), $u_\tau = 0.109$ m/s. Equation 4.12 ($- - -$); equation 4.14 ($- \cdot -$). . . . 109

5.1 Experimental setup to measure the fluctuations of the solid fraction signal in a liquid solid flow. 115

5.2 Typical calibration of the impedance volume fraction meters. 3 mm glass particles in a 10.18 cm test section liquid fluidized bed. 116

5.3 Time and frequency domain volume fraction traces for a liquid fluidized 3 mm glass particles in a 5.08 cm diameter test section. 118

5.4 Time and frequency domain volume fraction traces for liquid fluidized 6 mm glass particles in a 5.08 cm diameter test section. 120

5.5 Time and frequency domain volume fraction traces for liquid fluidized 6.35 mm nylon particles in a 5.08 cm diameter test section. 121

5.6 Time and frequency domain volume fraction traces for liquid fluidized 4.5 mm steel particles in a 5.08 cm diameter test section. 122

5.7 Mean solid fraction fluctuation as a function of the solid fraction. Liquid fluidized particles in a 5.08 cm test section: 3 mm glass particles (+), 6 mm glass particles (∘), 4.5 mm steel particles (⊕), 6.35 mm nylon particles (⊗), and 3.41 mm PVC cylinders (⊙). 123

5.8 Mean solid fraction fluctuation as a function of the solid fraction. Liquid fluidized 3 mm glass particles in the 5.08 cm (+) and the 10.16 cm (□) test sections. 124

5.9 Mean solid fraction fluctuation as a function of the solid fraction. Vertical flow of 3 mm glass particles in both test sections. × cocurrent flow in 5.08 cm TS, ∗ countercurrent flow in 5.08 cm TS. ⊗ cocurrent flow in 10.2 cm TS, + countercurrent flow in 10.2 cm TS. 125

5.10 Mean solid fraction fluctuation as a function of the fluid velocity. × cocurrent flow in 5.1 cm TS, ∗ countercurrent flow in 5.1 cm TS. ⊗ cocurrent flow in 10.2 cm TS, + countercurrent flow in 10.2 cm TS. . 126

5.11 Effect of the filtering. High pass 4^{th} order Butterworth digital filter, with cut-off frequency of 3 Hz. The original signal is shown on the left column, the resulting signal after the filtering. The mean solid fraction added again after filtering. 128

5.12 Mean solid fraction fluctuation as a function of the solid fraction, before filtering (+) and after high-pass filtering (□). Results for 3 mm glass particles in the 5.08 cm and the 10.16 cm test sections. 129

5.13 Mean solid fraction fluctuation after high pass filtering as a function of the solid fraction. All from a 5.08 cm test section fluidized bed. Compare with the unfiltered measurements in figure 5.7. The lines are the predictions from equation 5.1 (solid line), equation 5.2 (dashed line).130

A.1 Time and frequency domain pressure traces (left and right columns respectively) for a direct collision of a 6 mm glass particle in water. . 147

A.2 Time and frequency domain pressure traces (left and right columns respectively) for a direct collision of a 4.5 mm steel particle in water. 148

A.3 Time and frequency domain pressure traces (left and right columns respectively) for a fluid pressure pulse due to a collision of two 6 mm glass particles in water. 149

A.4 Time and frequency domain pressure traces (left and right columns respectively) for a fluid pressure pulse due to a collision of two 4.5 mm glass particles in water. 150

B.5 The Hertz impact problem, $u_i = V_1 - V_2$. 152

B.6 Ratio of duration of collisions, τ_{p-p}/τ_{p-w}, as a function of ratio of elastic properties, E_p/E_w (solid line), and ratio of maximum compression forces F_{p-p}/F_{p-w} as a function of ratio of elastic properties (dashed line).155

List of Tables

2.1 Properties of particles used in experiments. 15

3.1 Properties of particles used in direct collisions experiments. 59

4.1 Properties of particles used in pressure front measurements experiments. 99

Nomenclature

a	particle radius, m
A_{tr}	Area of transducer, m^2
Ba	Bagnold number
C_o	proportionality constant (equation 3.18)
d_p	particle diameter, m
E	Young's modulus, GPa
F_m	maximum compression collision force, N
$F(t)$	hydrodynamic force, N
$f(t)$	unsteady drag force, N (equation 3.1)
g	gravitational constant, 9.81 m/s^2
$h(r)$	particle profile, m
$\dot{h}$	particle approach velocity, m/s
$\ddot{h}$	particle acceleration, m/s^2
H	distance between wall and particle surface, m
I	collision impulse, Pa s
I_f	force impulse $I_f = IA_{tr}$, N s
k	elastic property parameter, $(1+\alpha^2)/(\pi E)$
K	coefficient in equation 3.15
L	length of string of pendulum, m
m	mass of a particle, kg
n	empirical exponent of Richardson-Zaki relation
$p\{x\}$	probability function
$P(t)$	pressure, Pa
P_f	fluid pressure
P_p	particle pressure
Re_p	Reynolds number, $\frac{\rho_f v_p d_p}{\mu_f}$

$\dot{s}$	event rate, events/s
St_p	Stokes number, $\frac{mu_p}{6\pi\mu a^2}$
T	particle granular temperature, m^2/s^2
u_a	approach velocity, m/s
u_f	velocity of the fluid phase
u_i	impact velocity
u_o	superficial fluid velocity
u_p	velocity of the particle phase
u_r	radial velocity of the fluid in the gap
u_t	terminal velocity
u_τ	post-collision velocity, rebound velocity

Greek letters

α	Poisson's ratio
δ	thickness of viscous layer
ϵ	coefficient of restitution
ϕ	angle of incidence
Γ	density ratio (ρ_p/ρ_f)
μ	viscosity of the fluid, N/m^2 s
ν	solid fraction
ν'	solid fraction fluctuation
ν_*	close packed solid fraction = 0.62
ρ_f	density of the fluid, kg/m^3
ρ_p	density of the particle, kg/m^3
τ	duration of a collision, s
τ_w	wall shear stress, Pa
θ_i	initial release angle, degrees

Chapter 1 Introduction

1.1 Motivation and general background

A particulate flow is a two-component flow in which one of the phases, the dispersed phase, is a solid in the form of particles; the second component, the continuous phase, is a gas or a liquid. Examples of such flows can be found in many natural processes like snow avalanches, slides of rock debris, erosion, submarine debris flows, sand storms, dune formation, planetary rings, etc. Such flows can also be found in many new technologies in the fields of mechanical, petroleum, mining, chemical and nuclear engineering. In chemical industries alone it is estimated that 50% of the products and 75% of the raw materials are in the form of particulates (Nedderman, 1992).

Despite the prominence of this type of flows, a poor understanding remains of how multi-phase materials behave. Most of the industrial applications are designed empirically and there is no general approach to study these flows. The lack of basic understanding of such mixtures represents the most important limitation to better designs of systems that handle two or multi-phase flows. Due to their prevalence, even small improvements in the performance of these technologies could have an important economic impact.

A granular material consists of discrete solid particles dispersed in a fluid. However, the term "granular material" has been adopted by researchers mainly to refer only to dry granular materials. A distinguishing feature of a dry granular material is that the direct interaction between particles plays the dominant role in the flow mechanics. In this case, the effect of the interstitial fluid is negligible. In the case of liquid-solid mixtures these simplifying assumption cannot be taken. The interstitial fluid has a density of comparable magnitude to that of the solid phase, and its non-negligible viscosity adds an extra mechanism for energy dissipation. The dimensionless parameter defined by Bagnold (1954) is generally used to determine the

importance of interstitial fluid effects. Similar to the Reynolds number, the "Bagnold number" denotes the ratio of the inertia force to the viscous force, and is defined as

$$Ba = \frac{\Lambda^{\frac{1}{2}} \rho_p d_p^2 \left(\frac{\partial u_x}{\partial y}\right)}{\mu_f} \tag{1.1}$$

where Λ is a function of the solid fraction, ρ_p is the particle density, d_p is the particle diameter, $\partial u_x / \partial y$ is the local shear rate, and μ_f is the dynamic viscosity of the fluid. Three regimes of granular flow were identified by Bagnold: the macroviscous, the transitional, and the grain inertia regime. For $Ba < 40$, the flow is in the macroviscous regime where the viscosity of the interstitial fluid is dominant in the flow. For $Ba > 450$, the flow corresponds to the grain inertia regime, where the direct interaction between particles dominate the mechanics of the flow. The flows with a Bagnold number between the two limits are within the transitional regime, where both interstitial fluid and collisions between particles are important. The flows investigated in this study lie mostly in the transitional regime.

1.2 Complexity of multi-phase flows, the coupling of the phases

To illustrate the complexity associated with solid-liquid flows, the case of a liquid fluidized bed can be considered. For example, to predict the mixing coefficients, many factors have to be taken into account. Consider a simple case, in which the particles are mono-dispersed, no attraction or repulsion forces are experienced between particles, the fluid and the particle properties are constant, and there is no heat or mass transfer in between the phases or with the boundaries. To estimate the mixing, a measure of the random-type motion in the mixture is needed. In such a system, random motions can be produced by either of two mechanisms: the interactions between particles, or the interactions between particles and fluid. In the case of a dry granular flow the random motions are generated only due to collisions between par-

ticles and with the wall. The amount of random motions in such a case will also be a function of the particle concentration and of the particle properties (Campbell, 1990). In the case of a liquid-solid system, the collisions of particles will not only generate random motions of the discrete phase, but will also generate random-type motions in the fluid (Keening, 1997). The fluid phase itself may or may not have, depending on the Reynolds number of the flow, an inherent hydrodynamic random motion (Clift *et al.* , 1978). Whether or not the presence of the particle will enhance or reduce the levels or turbulence in the fluid is a function of the Stokes number of the particles (Hestroni, 1989). In either case, the turbulence in the continuous phase will affect the nature of the motion of the particles (Clift *et al.* , 1978). The modified rate of particle collisions will, therefore, affect the entire cycle of production of random motions. The prediction of the amount of mixing becomes untractable early on, even for simple systems. This kind of coupling between the phases is one of the reasons for the complexity associated with multi-phase systems.

1.3 Modeling of solid-liquid flows

Solid-liquid flows are usually modeled using a continuum approach that considers the solid and fluid phases as inter-penetrating mixtures, which are coupled through interaction terms. Separate sets of conservation equations are written for each one of the phases that are either postulated or derived by an averaging technique. A number of different averaging techniques have been used, such as ensemble averages (Zhang & Prosperetti, 1995), mass weighted averages (Hwang & Shen, 1993), time averages (Ishii, 1975) and volume averages (Prosperetti & Jones, 1984). The use of different averaging techniques results in different interpretations of the obtained terms and constitutive equations. This approach results in an incomplete set of equations, posing a problem of closure. To close the equations the constitutive relations and the form of the interactions terms have to be postulated or chosen in an *ad hoc* manner. Only recently, a few 'simple' cases have been attacked in a more systematic way. Those cases include Zhang & Prosperetti (1995) for inviscid dispersed two-phase flow, Nott

& Brady (1994) for viscous dominated suspensions, and Sangani *et al.* (1996) for dilute gas-solid suspensions.

A different approach to model liquid-solid mixtures is to model the particle phase as the primary subject and to account for the fluid phase only through its interaction to the particle phase (Batchelor, 1988). Although this approach reduces the number of the unknown expressions, it also leads to terms that have to be postulated.

1.4 Thesis outline

The primary aim of this thesis is to investigate the mechanics of particulate solid-liquid systems. The emphasis has been focused on the mechanics in the particle-level scale, rather than in the bulk behavior of the flow. A series of simple experiments was performed with the purpose of improving our basic understanding of individual particle interactions. A clear understanding of these basic phenomena may help explain the behavior of systems of greater degree of complexity.

A technique to measure the particle pressure was developed. The particle pressure is the pressure exerted on the containing walls of a particulate system due to the action of particles in the mixture. Hence, it can be considered a measure of the momentum transport attributed to the motion of particles and their interactions. A great deal of information can be extracted from the measurement of the particle pressure: momentum and energy exchange between phases, mixing coefficients, constitutive behavior of the mixture, generation of the random motions of particles, etc. The experimental setup and procedures for measuring the particle pressure are presented in Chapter 2. A discussion and analysis of the obtained results is included.

Chapter 3 presents a study of particle collisions when immersed in a liquid. The dynamics of the approach, contact and rebound are presented. Experimental measurements of the velocities of approach and rebound, and the pressure pulses generated by collisions of particles, are presented. A model to account for the influence of the liquid on the particle deceleration prior to contact is proposed. The results of the model are compared with the experimental measurements.

In Chapter 4 the study of the fluid pressure front generated by a binary collision of particles is presented, along with a brief review of the pressure-impulse theory. An inviscid analysis is obtained for the sudden acceleration of a rigid particle near a wall. Experimental measurements are presented and compared with the predictions from impulsive pressure theory.

To further investigate the mechanisms of the particle pressure, an investigation of the fluctuating component of the solid fraction in liquid-solid systems was performed. The use of a high-frequency-response impedance volume fraction meter allowed the measurement of the fluctuating component of the solid fraction in a liquid fluidized bed and a vertical gravity driven flow. Comparisons between the measurements and predictions are presented. The results of this investigation are presented in Chapter 5.

Chapter 6 summarizes and discusses the results obtained from this investigation. Topics of possible future interest are discussed as well.

Chapter 2 Particle pressure in liquid-solid flows

2.1 Introduction

The particle pressure can be defined as the pressure exerted on the containing walls due to the presence of particles. Hence, it can be considered a measure of the momentum transport attributed to the motion of particles and their interactions. In analogy with kinetic theory of gases, the particle pressure resembles the thermodynamic pressure.

In many theoretical models of multi-phase flows, a separate set of equations is usually written for each of the phases, which are coupled through an interaction term. Pressures, P_f on the dispersed phase and P_p in the discrete phase, are defined and the corresponding pressure gradient terms are included in the momentum conservation equation. While $\partial P_f/\partial x_i$ does not impose any conceptual difficulty, the physical meaning of $\partial P_p/\partial x_i$ is less clear because of the discrete nature of the solid phase. Modeling such a pressure is problematic, due to the uncertainty in its definition and the difficulties involved in its measurement.

The particle pressure can be defined from the trace of the particle phase stress tensor. Hence, the physical mechanisms incorporated into the particle pressure can be gleaned from components of the stress tensor. From rapid granular flows (Campbell, 1990), in which the effect of the interstitial fluid is negligible, two contributions to the stress can be identified: the 'streaming' or Reynolds stress and the collisional contribution to the stress. The streaming component of the stress appears as a result of the momentum transfer due to the fluctuating velocity of the particle phase. The collisional stress reflects the momentum transfer between particles during a collision. In concentrated mixtures, stresses can also be generated due to enduring contacts

between particles. Force chains appear and stresses are transmitted through the bulk of the mixture over distances of many particles (Liu *et al.* , 1995). When the interstitial fluid is not negligible, a hydrodynamic contribution to the particle stress tensor is added to account for the drag or added mass of the particles (Nott & Brady, 1994; Balthius *et al.* , 1995; Tsao & Koch, 1995; Sangani *et al.* , 1996). Contributions to the stress due to non-hydrodynamic interactions can occur when there are other inter-particle forces such as colloidal forces or those due to electrostatic charging.

This Chapter describes a new technique for measuring the particle pressure in particulate solid-liquid systems using a high-frequency-response dynamic pressure transducer that measures the collisions of individual particles with the walls. Time averaged pressures are measured for various flow conditions and concentrations and for different particle sizes and densities. An estimate of the particle impact velocity is calculated from the measurement of the collisional impulse.

2.1.1 Particle pressure models

For the past thirty years there have been several attempts to model the constitutive behavior of two-phase mixtures including the particulate phase pressure. Early attempts simply assumed the particle pressure to be equal to the fluid pressure (Wallis, 1969), or equated it to zero due to its supposed negligible effect (Jackson, 1963).

More recently, the significance of this quantity has been encountered in the context of stability of fluidized beds. Studies have shown that the gradient of the particle pressure is a dominant factor in determining the stability of the mixture (Jackson, 1985; Batchelor 1988; Foscolo & Gibilaro 1987; Jin 1996) because of its dependence on the local concentration gradients within the flow. Some researchers recognized that it could be generated by particle collisions (Needham & Merkin, 1983), but due to a lack of experimental evidence, they assumed it to be a simple function of the void fraction,

$$P_p = P_o \nu \tag{2.1}$$

where P_o is a constant and ν is the solid volume fraction of the mixture.

In the work by Batchelor (1988), the governing equations for the mean motion of particles in a fluidized bed are formulated based on one-dimensional control volume analysis. All of the parameters within the model are linked on physical arguments to the two dependent variables - the local solids concentration, ν, and the superficial fluid velocity, u_o (referred to by Batchelor as the local mean particle velocity according to the frame of reference used in his paper). The volume-averaged model introduces a closure problem; hence, the term in the governing equation that involves the square of the velocity fluctuations, $\langle v^2 \rangle$, must be related to the local mean velocity and the solids concentration. Batchelor assumes that in a homogeneous bed, $\langle v^2 \rangle = F(\nu) u_o^2$, where $F(\nu)$ is some function of solids fraction. The function $F(\nu)$ is assumed to approach 0 for two limiting cases: as ν approaches 0, and as ν approaches the close-packed limit. The first limit is due to the absence of velocity fluctuations as the number of particles approaches zero; the second limit for high solids concentration results from the decrease of fluctuations as particles approach a dense state. Batchelor also argued that the representation for $\langle v^2 \rangle$ would depend on the local gradients of solids concentration and mean velocity for non-homogeneous flows. In the governing equations the term $mn\langle v^2 \rangle$, where m and n are the particle mass and number density, corresponds to the mean normal stress in an ideal gas of molecules. Hence, Batchelor's representation for the collisional particle pressure in a homogeneous bed is

$$P_p = \nu \rho_p F(\nu) u_o^2 \tag{2.2}$$

where ρ_p is the density of the particles. Using the simplest representation for $F(\nu)$ to satisfy the limiting conditions on ν, Batchelor suggested the following representation,

$$F(\nu) \approx \frac{\nu}{\nu_*} \left(1 - \frac{\nu}{\nu_*} \right)$$

where ν_* is the closed packed solid fraction ($\nu_* \approx 0.62$ for a randomly packed bed of uniform sized particles).

Besides the work of Batchelor, the stability work by Foscolo & Gibilaro (1988)

can also be used to find a representation for the particle pressure. They introduce a force that is applied to the particles due to the particulate nature of the fluidized bed. This force depends on the 'particle phase pressure' and is calculated from fluid dynamic considerations. The value of the particle phase pressure can be determined by integrating the particle phase pressure gradient given by Foscolo and Gibilaro. Using their terminology the pressure is written as

$$P_p = \nu^2 \rho_p u_e^2 \tag{2.3}$$

where u_e is the 'elastic wave velocity' and is defined as

$$u_e = \left(3.2 g d_p \frac{\rho_p - \rho_f}{\rho_p} \right)^{\frac{1}{2}} \tag{2.4}$$

where ρ_f is the density of the fluid phase, g is the acceleration due to gravity and d_p is the diameter of a particle.

Koch (1990) and Kapbasov & Buyevich (1994) followed similar analyses to study fluidized systems based on modifications to kinetic theory to include the effects of the interstitial fluid. In the study by Koch, expressions for the particle phase stress, as a function of the particle Stokes number, are obtained for the case of dilute mixtures. The particle pressure is expressed as

$$P_p = \rho_p \nu T \tag{2.5}$$

where T is particle fluctuating 'temperature',

$$T = G(\nu)\ St^{-2/3}\ (u_p - u_f)^2$$

and St is the particle Stokes number defined as $St = m(u_p - u_f)/(6\pi\mu(\frac{d_p}{2})^2)$, u_p and u_f are the ensembled averaged particle and fluid velocities respectively, and $G(\nu)$ is a function of the solid fraction.

The fluidized bed work by Kapbasov & Buyevich (1994) introduces a volume-

averaged model. Similar to the work by Koch, the particle pressure is linked to the square of the velocity fluctuations, or the granular 'temperature'. Hence, similar to kinetic theory, the particle pressure is equated to the fluctuation temperature, T,

$$P_p = \rho_p T H(\nu) \tag{2.6}$$

where the function $H(\nu)$ is the particle distribution function used in dense-gas kinetic theory analyses, such as the Carnahan-Starling or the Enskog representations (Chapman, 1939). The authors solve explicitly for the normalized fluctuation temperature as a function of the solids concentration in a macroscopically uniform mixture. The particle pressure from this study can be written in a form similar to that developed by Batchelor,

$$P_p = \nu \rho_p H'(\nu) u_o^2 \tag{2.7}$$

where the function $H'(\nu)$ is determined from the choice of the particle distribution function and the calculations for the particle temperature.

In addition to the analyses for fluidized beds, the particle pressure term has also been encountered in studies involving turbulent solid-fluid mixtures (Abu-Zaid & Ahmadi 1995; Ahmadi & Ma 1990; Ahmadi 1985). In the dispersed mixture work by Abu-Zaid & Ahmadi (1995), the authors use the following relation for the mean particle pressure,

$$P_p = \frac{P_f \nu}{1 - \nu} \tag{2.8}$$

where P_f is the mean interstitial fluid pressure. This expression is applicable when the particles are not in direct contact except during short collisional periods.

Despite the theoretical studies described above, there have been few attempts to measure the particle pressure experimentally, primarily because of a lack of experimental techniques that provide a reliable measurement of this quantity. In a study of gas fluidized beds, Campbell & Wang (1990) used a capacitance probe, which measured the difference between the total pressure and the gas pressure, and hence measured the average pressure generated by the particles. They concluded that the

granular pressure results from agitation generated by the rising bubbles that appear in gas fluidized systems. The bubbles cause the movement of many particles towards the container walls, thus generating a pressure. This description would not hold for a liquid fluidized system since bubbles generally do not appear.

The first attempt to measure the particle pressure in a liquid fluidized bed was by Kumar *et al.* (1990). They used a flush mounted hydrophone to record the collisions of particles with the face of the hydrophone. The calibration of their hydrophone was not satisfactory. However, some of the qualitative phenomena were clearly captured in their results.

2.2 Experimental setup

Typically, collisions of particles against the wall have a duration of tens of microseconds; therefore, to record such events, it is necessary to use a device with a very high frequency response. The current experiments use a piezoelectric dynamic pressure transducer manufactured by PCB Piezotronics, which can respond to changes in pressure up to two microseconds. It has an active surface of 3.75 mm diameter. A typical signal resulting from a collision is shown in figure 2.1. It consists of a positive spike (of 22 μs of duration in this case), followed by a decaying oscillation, which is probably the result of the dynamics of the membrane. For the experimental measurements two different pressure transducers with similar characteristics were used.

Experiments were performed in the facility shown in figure 2.2. Two different circular test sections with internal diameters of 10.16 cm and 5.08 cm were used. The test section was fabricated out of transparent lucite to facilitate the visual observation of the flowing mixtures. Prior to an experiment the particles were stored in a bin on top of the working section. By setting the aperture of the controlling solids cylinder and the downstream water valves, different flow conditions could be generated. Both cocurrent and countercurrent flows were obtained for a wide range of solid fractions. Also, by installing a screen and a flow straightener at the bottom of the working

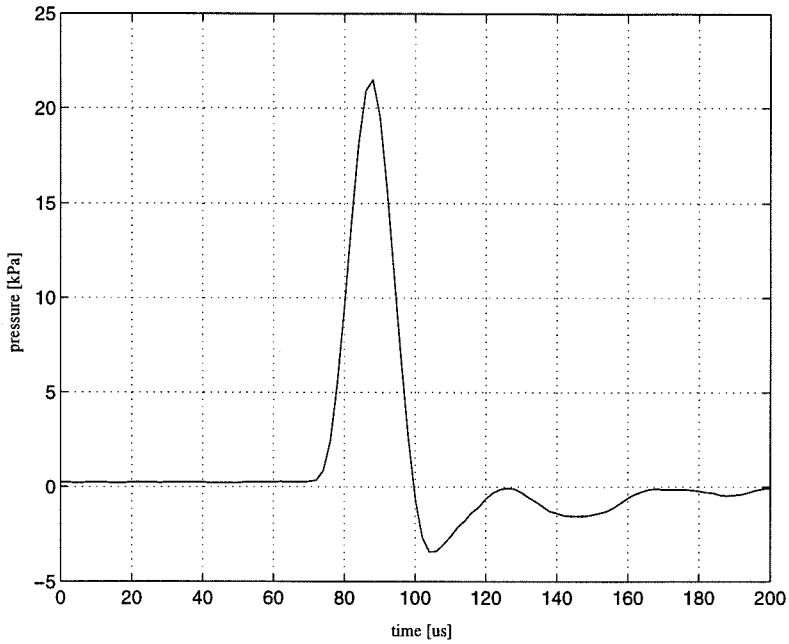

Figure 2.1: Typical pressure pulse generated by a particle collision.

section, the system was also operated as a fluidized bed. The particles employed were all nearly monodisperse spherical particles. Properties of the particles are listed in table 2.1. The solid fraction was monitored using an impedance volume fraction meter (IVFM) developed by Bernier (1982) and improved by Kytömaa (1985). This device measured the instantaneous impedance of the flowing mixture, which is proportional to the volume fraction of the non-conducting disperse phase averaged over the cross section; the calibration of this device was obtained as described by Kytömaa (1985). The instrumentation is shown in figure 2.3. The liquid used for all the experiments was filtered tap water.

The data acquisition system was started once the system had reached a steady state. The signal obtained from the transducer was high-pass filtered and amplified and then input to a trigger box and to a computerscope data acquisition system mounted in a PC. Pressure fluctuations below 1 kHz were filtered out completely, thus only the pressure pulses generated by the collisions of particles were detected with the present setup. To eliminate the collection of background noise, a threshold level had to be chosen, and this was set in the trigger box. When the signal from the transducer was higher than the threshold level, the trigger box activated the data

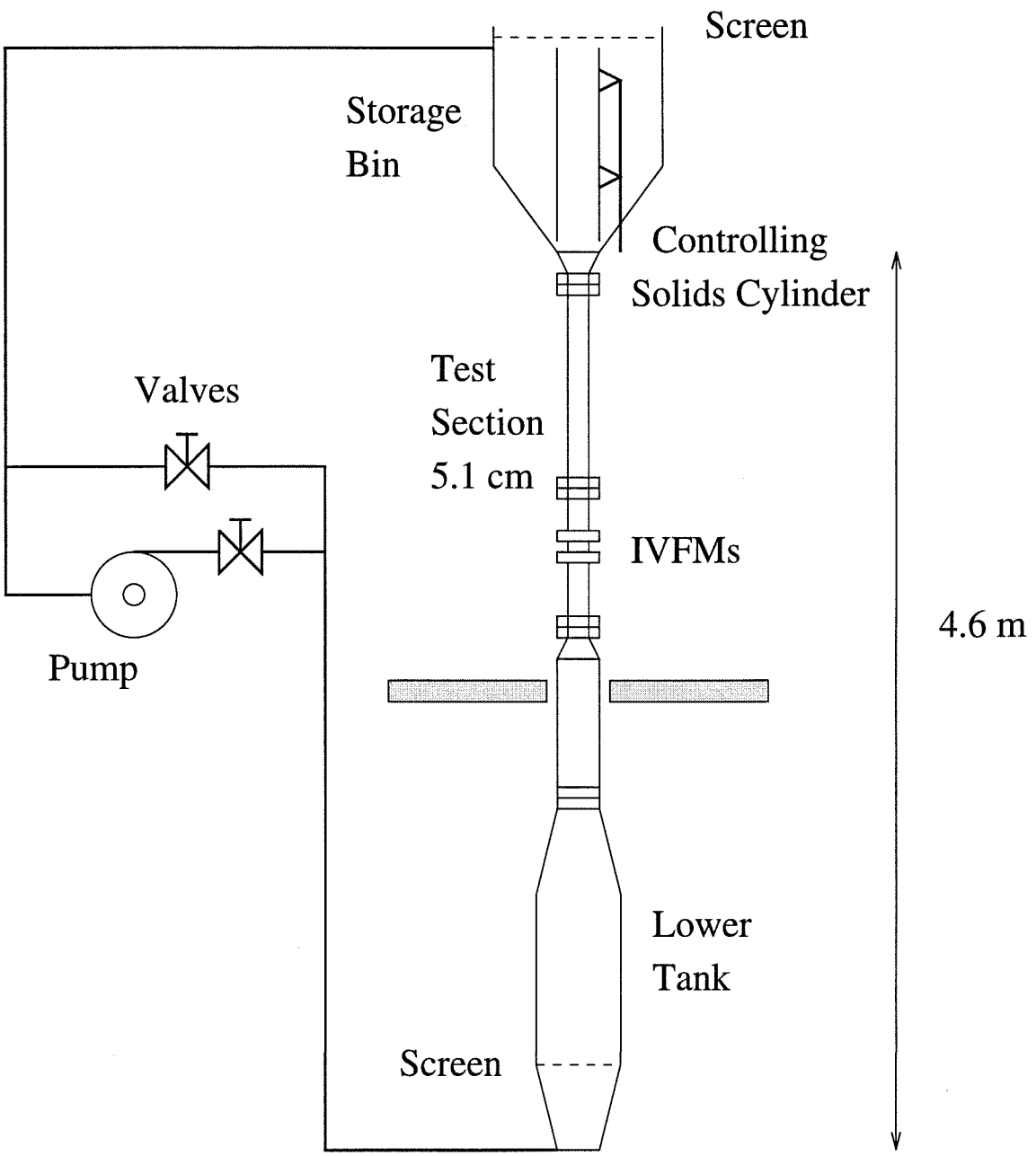

Figure 2.2: Experimental setup.

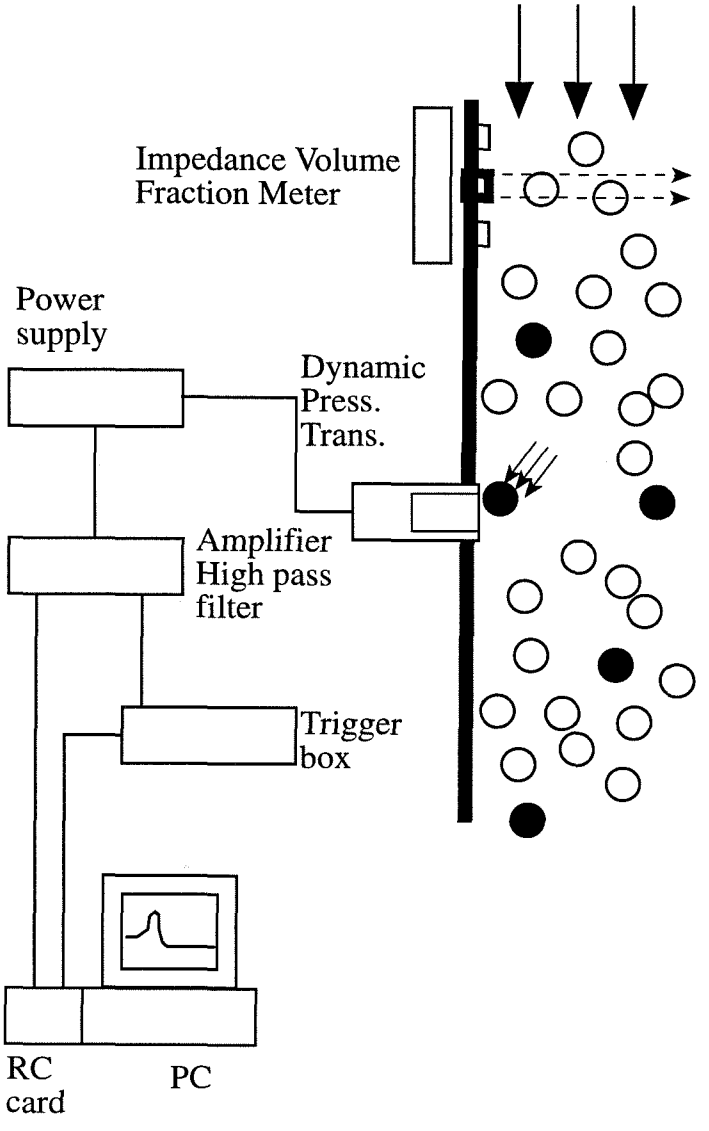

Figure 2.3: Experimental setup, instrumentation.

Material	d_p [mm]	ρ_p/ρ_f	u_t [cm/s]	Re_t	n
Glass +	2.06	2.54	22.7	452	2.39
Glass ×	3.00	2.54	31.8	954	2.40
Glass *	3.96	2.54	36.8	1338	2.40
Glass ○	6.00	2.54	47.4	2583	2.40
Steel ⊕	4.50	7.78	89.6	3665	2.40
Nylon ⊗	6.35	1.14	13.6	785	2.40
PVC ⊙	3.41[a]	1.43	29.69	440	2.44

[a] equivalent diameter, cylindrical shape

Table 2.1: Properties of particles used in experiments.

acquisition card and the signal was stored in the computer's memory. A software program then calculated, in real time, the maximum pressure, impulse and duration of the collision, stored the results on disk and reset the data acquisition card. This allowed the data acquisition system to take measurements in a continuous manner. The event rate was measured independently with a counter that indicated the number of times the signal exceeded the threshold level in a given time period.

As expected for large dense particles, the experiments exhibited important concentration fluctuations in the form of voidage waves (Harrison *et al.* , 1961). As the concentration of the bed decreased, the solid fraction fluctuations became more random, and the voidage waves were difficult to discern. A more extended analysis can be found in Chapter 5. These waves do not contribute directly to the granular pressure, though the shearing they imply may add to the production of random granular motions.

The time average particle pressure is calculated as

$$P_p = \dot{s} I_m \tag{2.9}$$

where $\dot{s}$ is the event rate and I_m is the average impulse. The impulse is

$$I = \int_0^\tau P(t) dt \tag{2.10}$$

where $P(t)$ is the pressure signal produced during an individual impact, and τ is the duration of the collision. An estimate of the impact velocity, u_i, can be calculated from

$$u_i = F_m \tau / m \tag{2.11}$$

where F_m is the maximum force exerted on the transducer during an individual collision and m is the mass of the particle. The maximum force is calculated by multiplying the measured maximum pressure P_m by the area of the sensitive surface of the transducer. Sets consisting of at least 100 collisions were used to calculate the average values of granular pressure and impact velocity, which were made over a time period in the order of hundreds of seconds.

The pressure transducers were installed at different axial locations in the working section to determine the axial variations in the particle pressure. No significant change with axial location was detected for the flowing mixture. In the case of the fluidized bed, some variation occurred when the transducer was less than one test section diameter above the bottom of the bed.

The accuracy and calibration of the pressure transducer were verified by comparing the output collision signals with predictions from the Hertzian theory of contact. Hertzian theory (see for example Goldsmith, 1960) predicts the duration and the maximum compression force during a collision as a function of impact velocity and particle properties. For a sphere impacting a flat surface, the maximum compression force is

$$F_m = 0.706 \left(\frac{u_i^6 m^3 d_p}{(k_1 + k_2)^2} \right)^{1/5} \tag{2.12}$$

where k_j is

$$k_j = \frac{1 + \alpha_j^2}{\pi E_j} \tag{2.13}$$

where u_i is the impact velocity, E_j is the Young's modulus of elasticity for material j, and α_j is the corresponding Poisson's ratio. The collision duration is

$$\tau = 7.894 \left(\frac{m^2 (k_1 + k_2)^2}{d_p u_i} \right)^{1/5} \tag{2.14}$$

Therefore, the collision impulse (as defined by 2.10) is

$$I = 2.047\frac{u_i m}{A_{tr}} \tag{2.15}$$

Hence, from Hertzian theory, the magnitude of the collision impulse does not depend on the elastic properties of the surfaces in contact. This result is in accordance with a simple momentum conservation analysis. From basic mechanics, the impulse can be defined as[1]

$$I_f = um$$

where u is velocity and m is mass. For the case of the impulse as a result of a collision,

$$I_f = m(u_i - u_\tau)$$

where u_τ is the rebound velocity. If the collision is perfectly elastic then $u_\tau = u_i$; therefore,

$$I_f = 2mu_i = IA_{tr}$$

which is in accordance with equation 2.15[2].

A simple calibration device was constructed involving a pendulum consisting of a glass particle and a fine string. The particle was positioned initially such that a controlled direction and velocity of impact could be applied to the transducer. The measured collision characteristics in air were compared with the Hertzian predicted values by calculating the impact velocity from the pendulum equation (neglecting the effect of air) and using tabulated material properties (Avalone *et al.* , 1986). Figure 2.4 shows a comparison of the compression pressure as a function of impact time for a 3 mm glass particle. The Hertzian predictions use a value of α=0.22 and E=40.4 GPa. Figures 2.5 and 2.6 present the calibration measurements of the impact pressure and duration of collision and the comparison with the predictions

[1]based on the force, not the on pressure.

[2]the difference in the constant is the result of the approximation made by Hertzian theory to obtain the duration of collision.

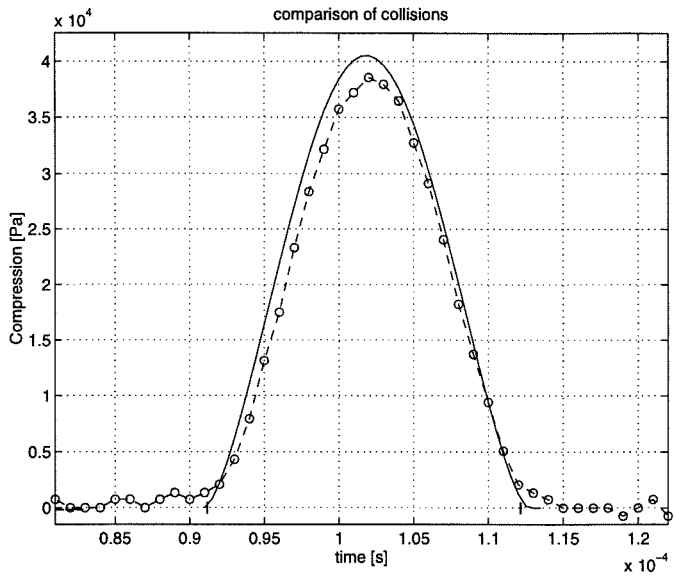

Figure 2.4: Calibration of the pressure transducer. Direct comparison of experimental collision in air (o) against Hertzian prediction (−). u_i =75 mm/s.

from Hertzian theory. A perfect match is not expected due to the many assumptions in the development of Hertzian theory. The Hertzian model was used to confirm the nature and magnitude of the forces occurring during a collision. Based on these comparisons the manufacturer's calibration was used in the subsequent analysis of the data.

2.3 Results

2.3.1 Liquid fluidized bed experiments

The granular pressures measured in the fluidized bed are shown in figure 2.7 as a function of the solid fraction for glass particles with four different diameters. These tests were all performed in the small diameter test section (5.1 cm). For a dilute system, at low concentrations, the value of the particle pressure is low. In this regime the particles are free to move and collide sporadically; therefore few particles collide with the transducer per unit of time, making the event rate small. On the other hand, at high solid fractions collisions are more likely to occur. However, due to the high concentration, these collisions occur at very small velocities producing low

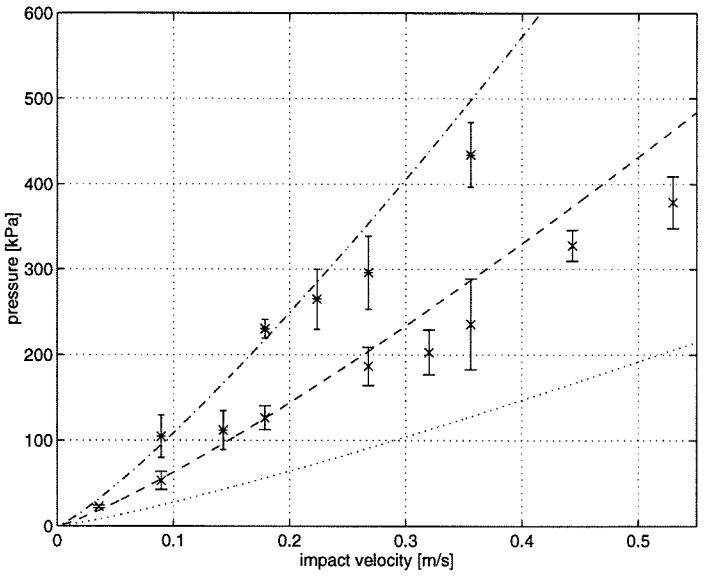

Figure 2.5: Calibration of the pressure transducer. Impact pressure as a function of impact velocity and particle diameter. Experimental (in air): ($\times$) 3 mm glass bead, ($*$) 4.2 mm glass bead. Hertzian predictions: 2 mm glass bead = $\cdots$, 3 mm glass bead = $- -$, 4.2 mm glass bead = $- \cdot -$.

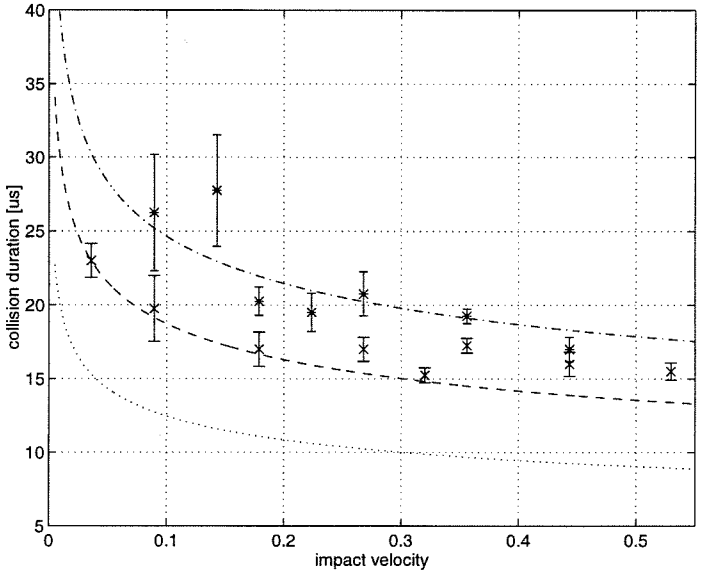

Figure 2.6: Calibration of the pressure transducer. Duration of collision as a function of impact velocity and particle diameter. Experimental (in air): ($\times$) 3 mm glass bead, ($*$) 4.2 mm glass bead. Hertzian predictions: 2 mm glass bead = $\cdots$, 3 mm glass bead = $- -$, 4.2 mm glass bead = $- \cdot -$.

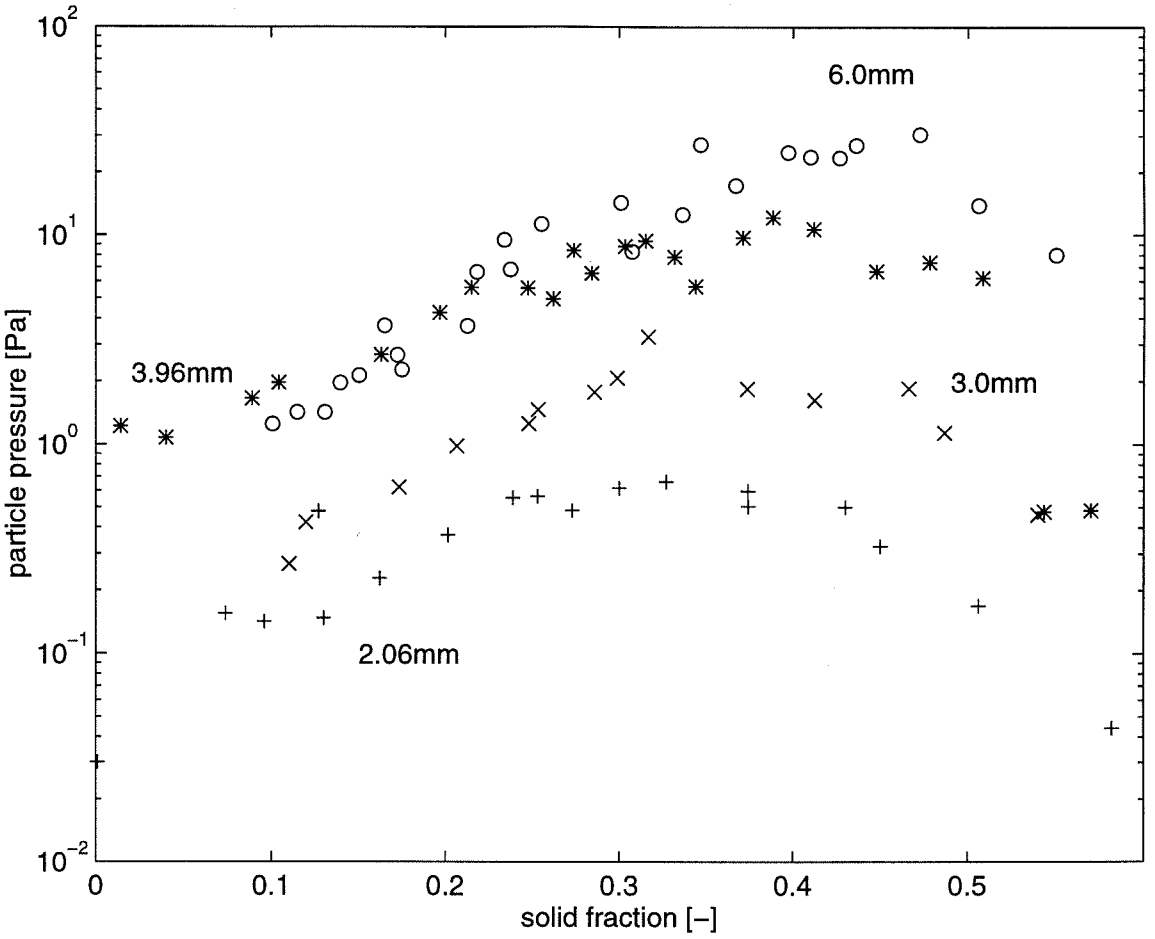

Figure 2.7: Particle pressure P_p as a function of the solid fraction ν for fluidized glass particles in the 5.1 cm test section.

impulse collisions, which result in a low value of the particle pressure. At intermediate concentrations (from 30 to 35%) the particle pressure reaches a maximum. In this range the impact velocity is higher than in the concentrated case, and the event rate is higher than in the dilute case. The combination of these two competing mechanisms results in a maximum particle pressure for these intermediate concentrations.

The value of the particle pressure is a function of the particle size, being higher for larger particle diameters. The maximum pressure is located at slightly higher concentrations for larger particles. Figure 2.8 shows the particle pressure as a function of the superficial velocity of the fluid u_o. The velocity u_o is calculated using the

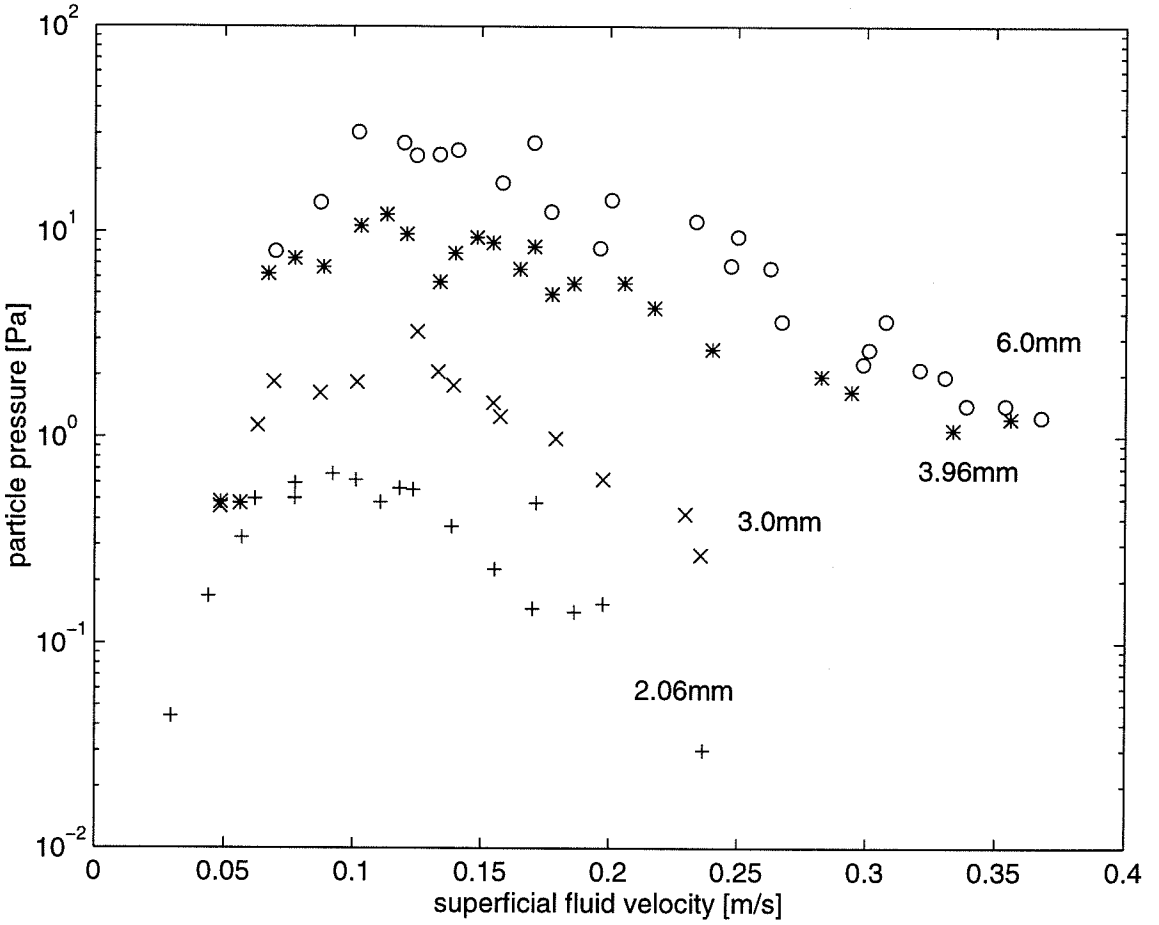

Figure 2.8: Particle pressure P_p as a function of the superficial fluid velocity u_s for fluidized glass particles in the 5.1 cm test section.

Richardson-Zaki relation

$$u_o = u_t(1-\nu)^n \tag{2.16}$$

where n is an empirically determined parameter which depends on the terminal Reynolds number of the particle, Re_t. Table 2.1 includes the values of n for the particles used in these experiments (Kwauk, 1965). As shown in the figure, above the minimum fluidization velocity the measured value of the particle pressure increases rapidly. After reaching a maximum value for some intermediate velocity, the granular pressure decreases again and tends to zero as the superficial velocity approaches the value of the terminal velocity.

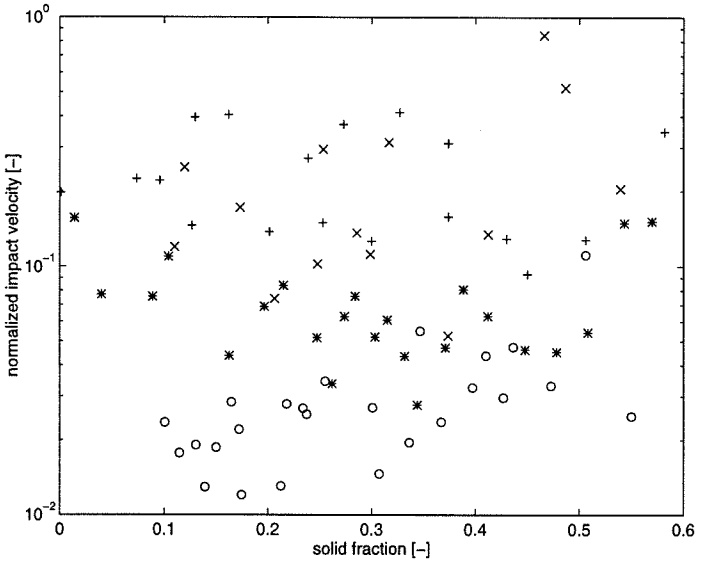

Figure 2.9: Calculated impact velocity u_i, normalized by u_t, as a function of the solid fraction ν for fluidized glass particles in the 5.1 cm test section. For symbol identification see Table 1.

A plot of the average impact velocity (normalized by the terminal velocity, u_t) as a function of the solid fraction is shown in figure 2.9 for glass particles in the 5.1 cm diameter test section. Even with substantial scatter, the smaller particles tend to collide at higher velocities than larger particles. The impact velocity does not appear to have a consistent trend when plotted as a function of the solid fraction. All collision velocities are consistently below the terminal velocity.

Some of the features of fluidized systems are believed to be determined by the geometry and dimensions of the container (Kytömaa & Brennen, 1986). To investigate the dependency of the granular pressure on the dimensions of the bed, tests were conducted in the two different test sections. A comparison of the granular pressures is presented in figure 2.10 as a function of the solid fraction. To enable the comparison the two plots are presented side by side, and only the results for glass spheres are shown. The difference between the two cases is not significant, although the amount of scatter is slightly higher for the larger test section. Figure 2.11 shows a comparison of the calculated impact velocity for the two test sections. The trends seem similar.

Experiments were also performed using particles of different densities. Figure 2.12

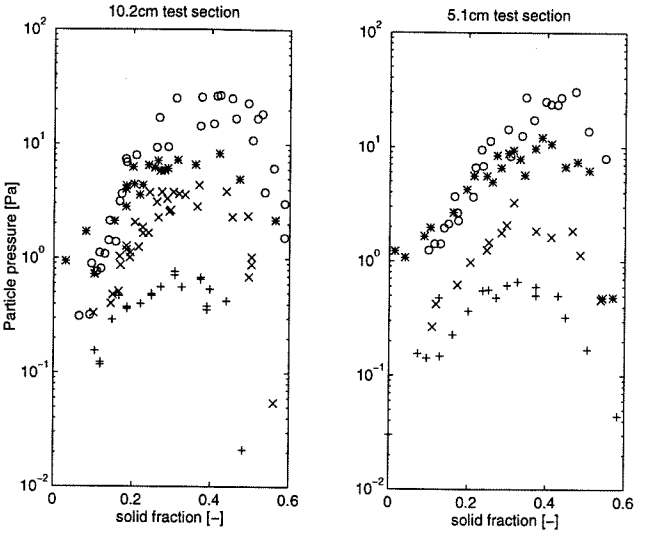

Figure 2.10: Particle pressure P_p as a function of the solid fraction ν. A comparison of the pressures measured in a 10.2 cm test section (TS) and a 5.1 cm TS. Fluidized glass particles. For symbol identification see Table 1.

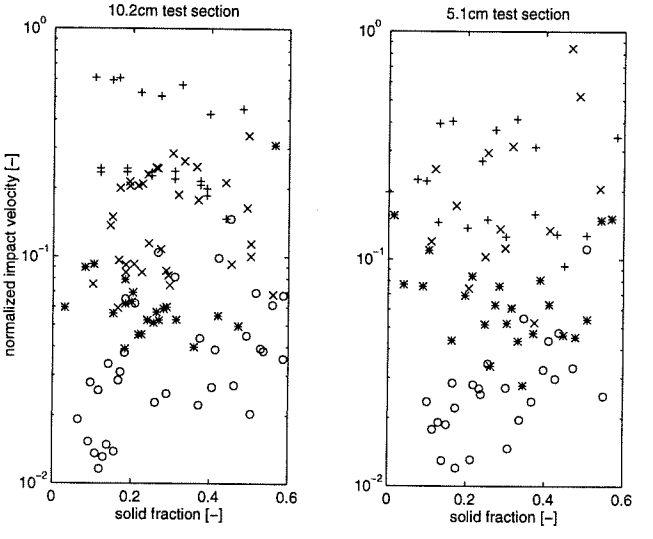

Figure 2.11: Calculated impact velocity u_i, normalized by u_t, as a function of the solid fraction ν. A comparison of the calculated impact velocities in a 10.2 cm test section (TS) and a 5.1 cm TS. Fluidized glass particles. For symbol identification see Table 1.

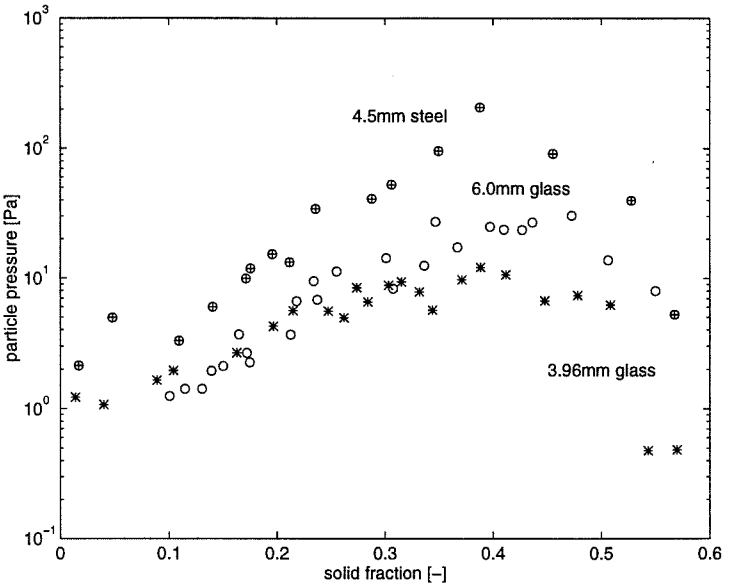

Figure 2.12: Particle pressure P_p as a function of the solid fraction ν. A comparison of particles with different densities for fluidized steel and glass particles in the 5.1 cm test section.

shows the particle pressure measured for steel particles of 4.5 mm diameter in a 5.1 cm test section. For comparison, the results are presented along with the measurements obtained for 3 mm and 4 mm diameter glass particles. Again, the more massive particles produce higher particle pressures. In figure 2.13 measurements for nylon spheres of 6.35 mm diameter and 3.43 cm PVC rods are shown along with the results for 6 mm, 3 mm and 4 mm glass spheres. Clearly, the granular pressure is higher for particles with greater density.

2.3.2 Vertical gravity driven flow

In a fluidized bed the net velocity of the particulate phase is zero and this lack of mean motion may affect the granular pressure. To investigate this possibility, measurements of the particulate pressure were also performed for a vertical flow in a mixture of glass particles in water. In all cases the net velocity of the solid phase is downwards. The motion of the liquid could be either downwards (cocurrent with the particles) or upwards (in a countercurrent configuration).

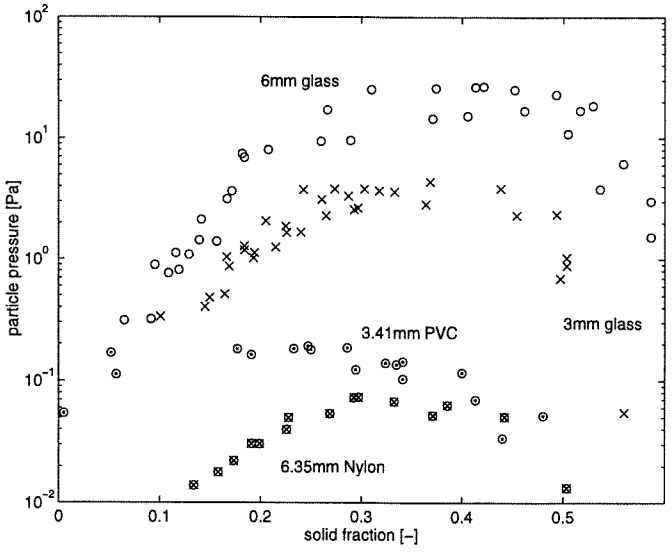

Figure 2.13: Particle pressure P_p as a function of the solid fraction ν. A comparison of particles with different densities for fluidized plastic and glass particles in the 10.2 cm test section.

Figure 2.14 presents the granular pressure measured for a flowing mixture under two flow conditions, cocurrent and countercurrent flows, and in both test sections. Figure 2.15 shows the calculated impact velocities. Both the impact velocities and the particle pressures obtained for these cases have a wider spread than in the case of fluidized beds. Therefore the variation of the particle pressure with respect to solid fraction is not as clear as in the case of a fluidized bed. In fact, the particle pressure remains fairly constant over the entire range of solid fraction, reaching a maximum around $\nu = 0.30$. Hence the net motion of the solid phase in the mixture causes different trends in the particle pressure. The magnitude of the pressures in the gravity driven flows is approximately the same as the maximum value found in the fluidized bed for the same particle size. Moreover, the direction of motion of the fluid phase does not appear to have significant influence on the magnitude of the measured particle pressure.

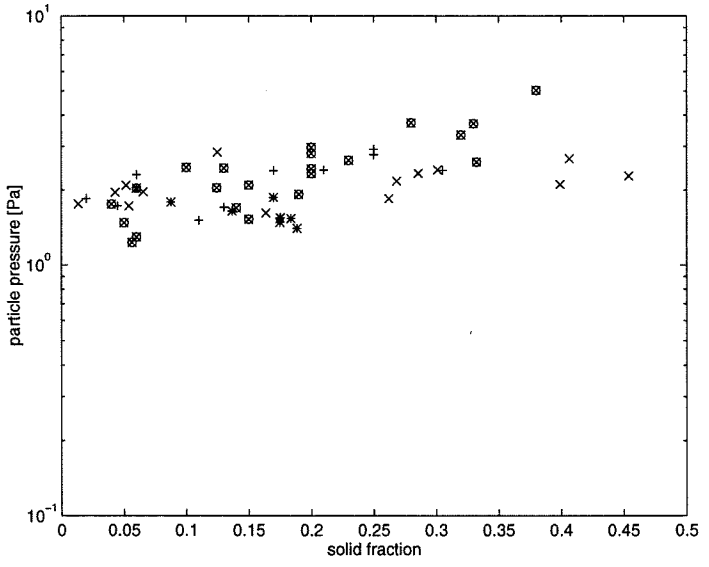

Figure 2.14: Particle pressure P_p as a function of the solid fraction ν. Vertical gravity driven flow of 3 mm glass particles. $\times$ cocurrent flow in 5.1 cm TS, $*$ countercurrent flow in 5.1 cm TS. $\otimes$ cocurrent flow in 10.2 cm TS, $+$ countercurrent flow in 10.2 cm TS.

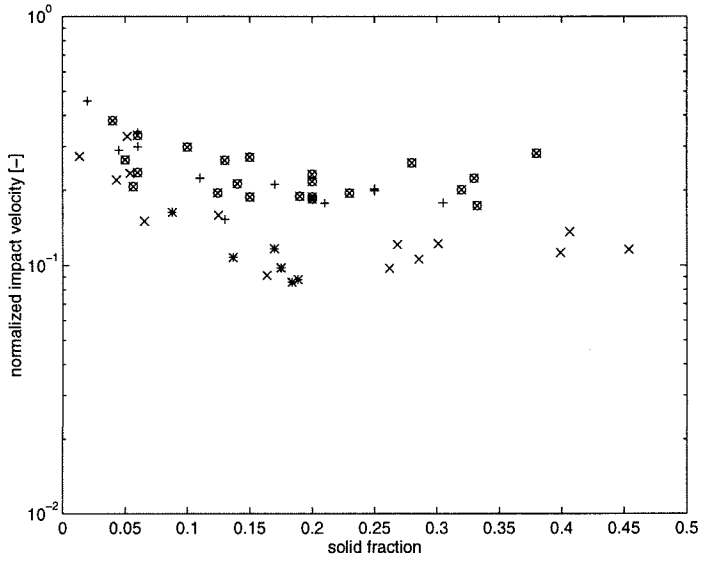

Figure 2.15: Calculated impact velocity u_i, normalized by u_t, as a function of the solid fraction ν. Vertical gravity driven flow of 3 mm glass particles. $\times$ cocurrent flow in 5.1 cm TS, $*$ countercurrent flow in 5.1 cm TS. $\otimes$ cocurrent flow in 10.2 cm TS, $+$ countercurrent flow in 10.2 cm TS.

2.4 Discussion

Figures 2.12 and 2.13 show the large differences in the magnitude of the particle pressure for particles of different density and size. For example, at a solid fraction of 0.4, the particle pressure for the 4.5 mm steel spheres is more than 3 orders of magnitude larger than the particle pressure for the 6.35 mm nylon spheres. Clearly the particle pressure must increase with the ratio of the density of the particles, ρ_p, to that of the surrounding fluid, ρ_f. In addition, the pressure must also depend on the velocity of the particles. Hence, an appropriate scaling of the particle pressure would be a particle dynamic pressure based on the particle density, ρ_p, and a characteristic velocity, u_t. Figure 2.16 presents a plot of the particle pressure normalized by $\frac{1}{2}\rho_p u_t^2$ for all of the types of particles as a function of the solid fraction. As observed from the figure, the difference between the normalized particle pressure for the 4.5 mm steel spheres and the 6.35 mm nylon spheres is less than an order of magnitude at a solid fraction of 0.4. Hence, the choice of the particle dynamic pressure appears to be the correct scaling for the particle pressure. However, there are still considerable differences in the normalized pressure for the different types of particles. One observation is that the higher the terminal Reynolds number, the greater the normalized pressure at a given solid fraction. The exception to this observation, however, is the steel spheres. This result may indicate that in addition to the solid fraction and the terminal Reynolds number, the normalized pressure may also depend on the ratio of the density of the solid phase to that of the fluid. This dependency is certainly suggested in the work by Batchelor (1988).

While the measurements obtained with the vertical flow have approximately the same magnitudes as in the fluidized bed, there are some notable differences. In addition, there were also some experimental limitations that may have influenced the results. It was not possible to generate highly concentrated flowing mixtures (>45%) in the present facility, and only low concentrations were possible for the case of countercurrent flows (< 25%). Furthermore, the number of individual collisions collected per test was limited by the running time of the experiment since only a

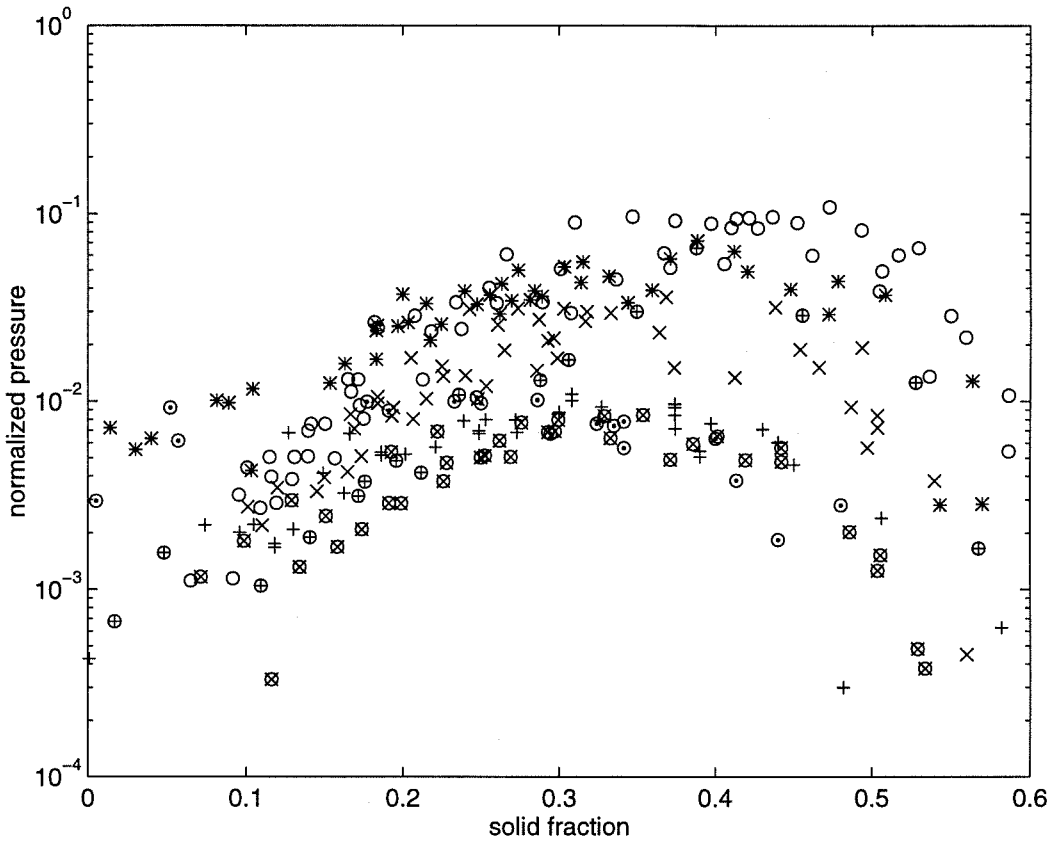

Figure 2.16: Non-dimensional particle pressure $\hat{P}_p$ as a function of solid fraction ν. Pressures normalized by $\frac{1}{2}\rho_p u_t^2$. Results for all particles and tests sections in a fluidized bed.

finite mass of particles could be stored in the bin. Therefore, for some conditions the experiment could only be operated for a few minutes. These factors contributed to the larger scatter encountered in particle pressures for the case of flowing mixtures. In addition, the particle pressure was not affected by the direction of the fluid flow.

The differences between the vertical flow and the fluidized beds measurements, for the same particles, are not completely understood. For concentrated mixtures the particle pressure does not decrease significantly, when compared to the results for fluidized beds. This The shear at the wall produced by the bulk motion of the mixture may be the responsible mechanism. The shearing at the wall can enhance the random motions of the particles; therefore, produce an increase of the particle pressure (shear pressure). The dilute regime vertical flow shows also that the particle pressure is higher than that of a fluidized bed. This difference can be attributed to an additional fluid turbulence effect. The bulk motion of the solid phase may generate the motion of the fluid phase in such a way that the mean random motion of the particles increases.

2.5 Comparison with existing models

Many models have been proposed for the particle pressure. Figures 2.17 and 2.18 present a direct comparison with some of these models. To facilitate the comparison only the results obtained for 3 mm particles in a fluidized bed are presented. The pressure data is presented in non-dimensional form, where the pressure is normalized by

$$\hat{P}_p = \frac{P_p}{\frac{1}{2}\rho_p u_t^2}$$

First, this comparison shows that five orders of magnitude are necessary to present the calculated particle pressures from the different models indicating the poor level of understanding of the phenomena. The qualitative behavior of the particle pressure for most of these models does not agree with the experimental measurements.

The model closest to the present experimental measurements is the one proposed

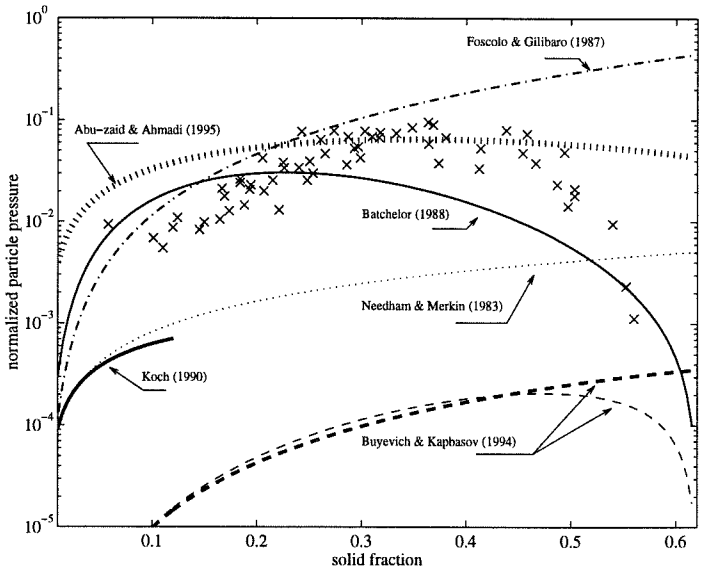

Figure 2.17: Comparison of the experimental results with theoretical models. Experimental results for 3 mm glass particles in a fluidized bed: $\times$. Pressures normalized by $\frac{1}{2}\rho_p u_t^2$.

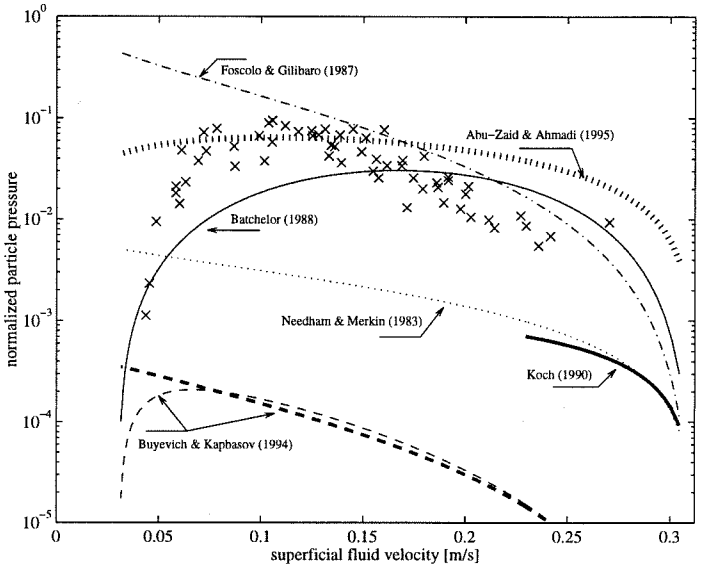

Figure 2.18: Comparison of the experimental results with theoretical models. Experimental results for 3 mm glass particles in a fluidized bed: $\times$. Pressures normalized by $\frac{1}{2}\rho_p u_t^2$.

by Batchelor (equation 2.2). This prediction works surprisingly well considering that the quadratic dependence on the solid fraction was chosen to fit the two known conditions on solid fraction.

The models proposed by Abu-Zaid & Ahmadi (equation 2.8) use the fluid pressure P_f as a reference. To compare, the reference fluid pressure is taken as $P_f = \frac{1}{2}\rho_f u_f^2$, where the velocity of the fluid phase u_f is calculated from the superficial fluid velocity, u_o, according to $u_f = u_o/(1-\nu)$. This expression overestimates the value of the particle pressure by a factor of 2 or 3 for low solid fractions ($\nu < 20\%$), and agrees well with the experimental measurements both in magnitude and slope for intermediate solid fractions ($25\% < \nu < 45\%$). However, it does not predict a significant decrease in the value of the pressure for concentrations greater than 45%. In their analysis, the particle pressure was considered to be only a fraction of the fluid pressure, which was not known accurately. The approximation given by $P_f = \frac{1}{2}\rho_f u_f^2$ may not be representative.

To compare with Koch's model (equation 2.5), the mean velocity of the solid phase, u_p, was assumed to be zero, and the fluid velocity $u_f = u_o/(1-\nu)$. Since the model is only for dilute systems, the predicted particle pressure is shown only for $\nu < 0.10$. Strictly speaking, the prediction is only valid for $\nu < St^{-2/3}$, which for the 3 mm particle corresponds to $\nu < 0.03$. Accurate measurements could not be obtained at such low concentrations; therefore, direct comparison is not possible. However, the model appears to agree with the other models at such small solid fractions.

The work of Buyevich & Kapbasov (equation 2.6) predicts a particle pressure that is considerably smaller than the experimental results. In this work the particle pressure was obtained following a modified kinetic theory. The particles are assumed to be massive enough to ensure that the exchange of momentum and energy is through direct collisions. Using two different expressions to account for the dependence on concentration, they obtain two curves, one which predicts a maximum at a concentration of approximately 50% (thin dashed line) and another that increases monotonically with solid fraction (thick dashed line). Although this approach is collision-based, some of the assumptions may not be appropriate, resulting in a poor correspondence

with the experiments.

The model of Foscolo *et al.* (equation 2.3) overestimates the granular pressure but has approximately the same slope as the measurements for solid fractions less than 30%. For all solid fractions the model predicts a monotonic increase of the particle pressure with increasing concentration and does not predict the existence of a maximum particle pressure at an intermediate solid fraction.

The appearance of a maximum at an intermediate solid fraction has important implications. The elasticity of the bed defined by Foscolo & Gibilaro (1989) would change sign at this maximum, going from positive for dilute mixtures to negative at high concentrations. A negative elasticity would imply a bed that is unstable to any perturbations, contradicting the experimental evidence in liquid-fluidized beds. In this particular case a direct comparison might not be valid. It is important to note that the definition of particle pressure given by Foscolo *et al.* differs essentially from the others. They define this quantity as a measure of the resistance to changes in concentration, a resistance which is visualized as result of a fluid interaction mechanism. Since the particle pressure measurements presented in this study are the direct result of particle collisions, it could be misleading to calculate the elasticity of the bed (as stated from Foscolo *et al.*) from these experimental results. It is interesting to note that Buyevich *et al.* (1994), in the discussion of their results, discarded the model that predicted a maximum at an intermediate solid fraction because it predicted a negative elasticity of the bed.

A better model for the granular pressure remains to be developed. Batchelor (1988) identified some of the questions that remain to be answered. Among them (and of relevance for understanding the mechanisms generating the particle pressure) is the prediction of the mean-square particle and fluid velocity fluctuations. Batchelor postulated that, in a homogeneous fluidized bed, the mean-square particle velocity fluctuation is a function of the solid fraction, the Reynolds number and the density ratio, but the exact functional form is unknown. The mechanisms that generate fluctuating velocities are a combination of the collisional and hydrodynamic interactions between particles. For mixtures with massive particles, like those discussed here, it

is not yet clear whether the particle collisions and hydrodynamic interactions would enhance or decrease the turbulence levels in the fluid phase, and whether or not the turbulence would promote or reduce the frequency and strength of the collisions among particles. The experimental results presented in this paper are intended to help refine understanding of these phenomena.

2.6 Probability density functions

A detailed statistical analysis of the measured collisions was also conducted. Sets of 1000 events (or more) were taken at a number of solid fractions to provide enough information to construct graphs of the probability density functions (PDF), or histograms of the occurrence of the individual collisional pressures, durations and impulses. Figures 2.19, 2.20 and 2.21 show the normalized probability density functions obtained for 3 mm glass particles in a 10.2 cm test section. The probability density functions are normalized such that

$$\int_0^\infty p\{x\}dx = 1.$$

Although these figures show the results of just one experiment, the repeatability was verified by taking consecutive sets of data points; once processed, the results obtained were practically identical.

Figure 2.19 presents the PDF of the collisional pressure. Clearly, low pressure collisions occur more frequently than high pressure collisions for all solid fractions. The value of the lowest pressure in the plot is the threshold level chosen for that experiment. The distribution becomes wider for lower solid fractions. In other words, more high-pressure impacts occur in a dilute bed.

Figure 2.20 shows the PDF of the collision duration. For all the solid fractions tested, the PDF shows a distribution with two distinct peaks. The first peak (short duration collisions) occurs at approximately 15 μs and its magnitude appears to be a function of the solid fraction. The second peak (long duration collisions) occurs at

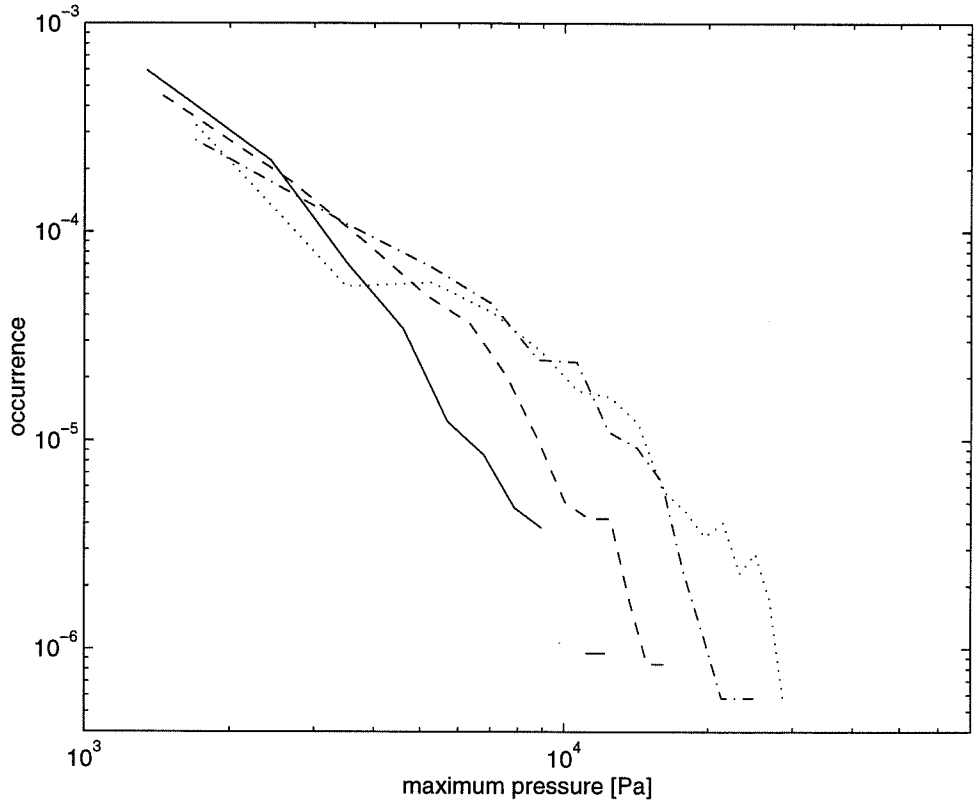

Figure 2.19: Probability density function of individual collision pressure. Fluidized glass 3 mm particles in a 10.2 cm test section. (—) $\nu = 0.503$, (– –) $\nu = 0.438$, (– · –) $\nu = 0.318$, (· · ·) $\nu = 0.194$.

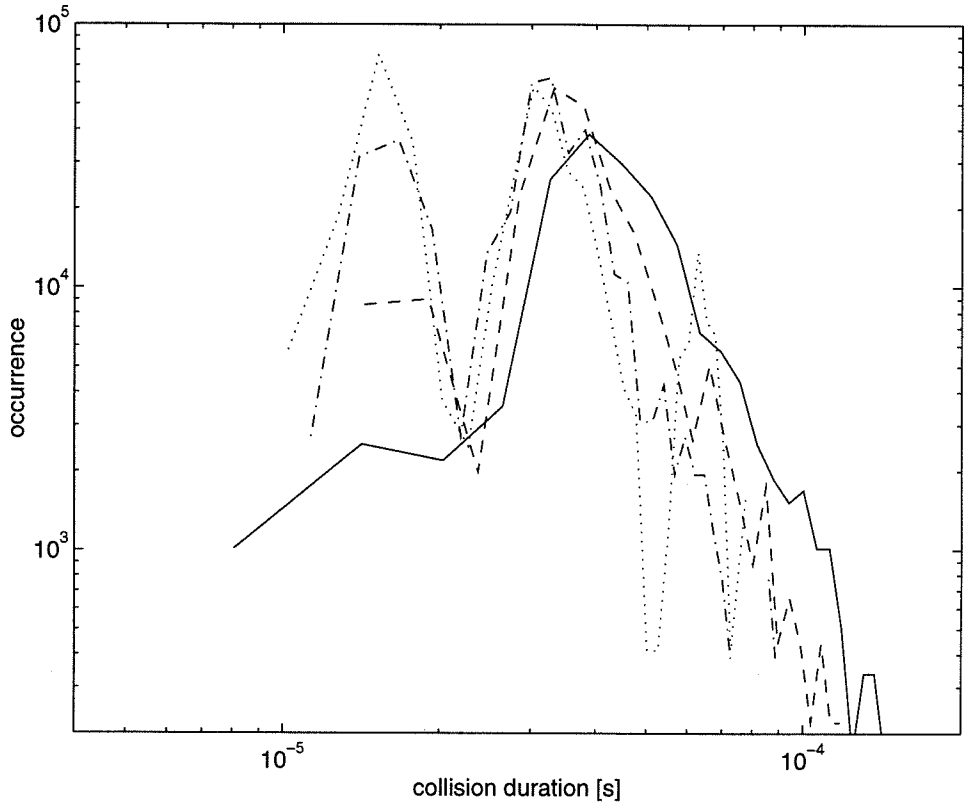

Figure 2.20: Probability density function of collision duration. Fluidized glass 3 mm particles in a 10.2 cm test section. (—) $\nu = 0.503$, (– –) $\nu = 0.438$, (– · –) $\nu = 0.318$, (· · ·) $\nu = 0.194$.

approximately 37 μs, and becomes narrower for lower solid fractions. During the calibration of the pressure transducer (which utilized normal impacts), *only* collisions of the long duration type were encountered. The duration of the long duration collisions is in accord with the Hertzian predictions. The short duration collision cannot be Hertzian: if the impact velocities were higher during the short duration collisions, the maximum pressure would also increase. However, the experimental results indicate that the short duration collisions are associated with low pressure collisions.

Figure 2.21 shows how the distribution of collision impulse changes with solid fraction. In a concentrated bed, collisions of low impulse are predominant. As the solid fraction decreases, the average impulse of the collision increases. The distribution becomes wider, indicating an increase in the occurrence of higher impulse collisions.

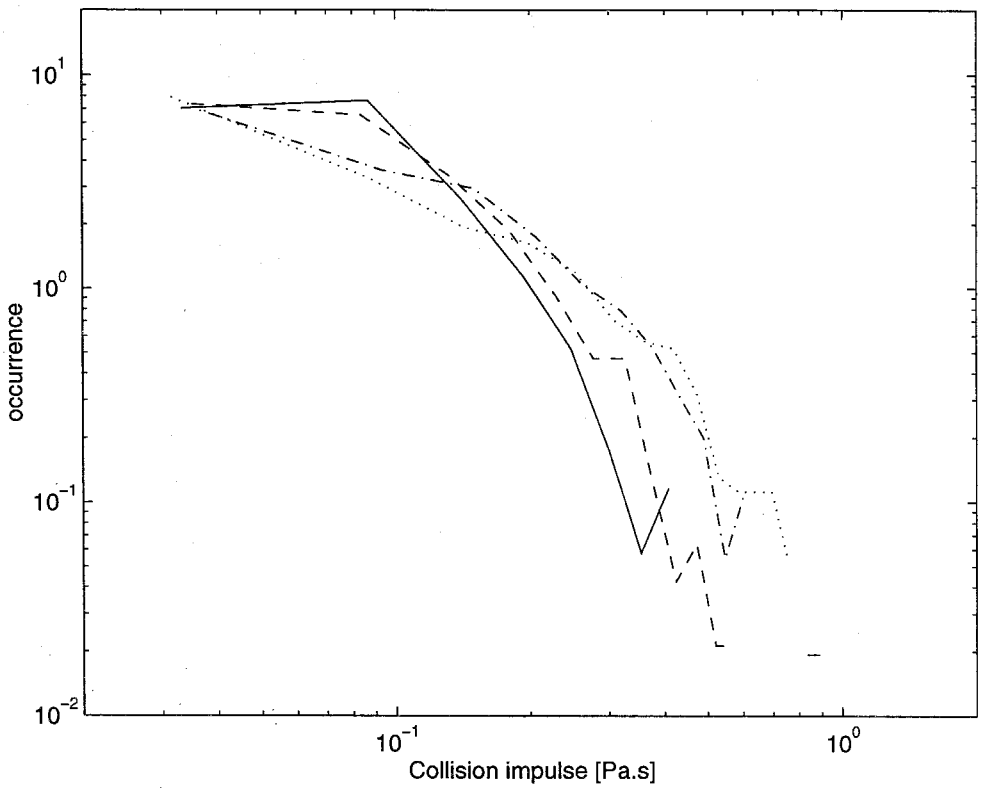

Figure 2.21: Probability density function of collision impulse. Fluidized glass 3 mm particles in a 10.2 cm test section. (—) $\nu = 0.503$, (– –) $\nu = 0.438$, (– · –) $\nu = 0.318$, (· · ·) $\nu = 0.194$.

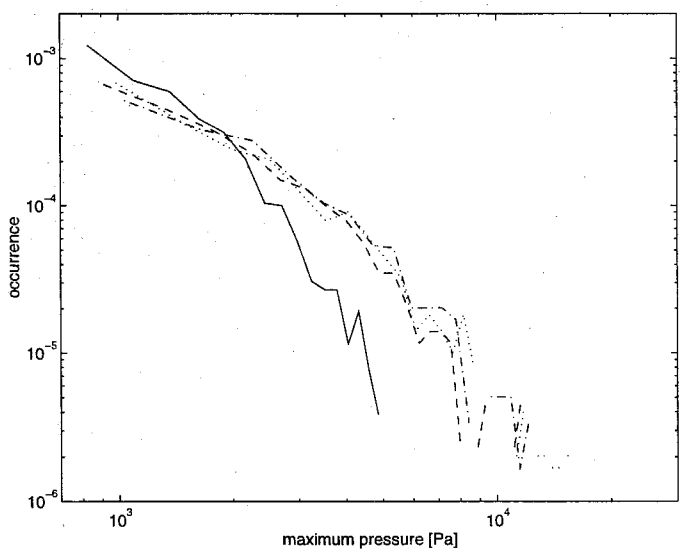

Figure 2.22: Probability density function of individual collision pressure. Fluidized glass 2 mm particles in a 10.2 cm test section. (—) $\nu = 0.4435$, (– –) $\nu = 0.327$, (– · –) $\nu = 0.243$, (· · ·) $\nu = 0.181$.

2.6.1 PDF for other particles

The same phenomena and trends are found for different particle diameters and densities. The magnitudes of individual collision pressures and collision impulses appear to be scaled with the particle mass. The two distinct peaks in the PDF of the collision duration occurred for all of the particles tested. The peaks occurred at different locations depending on the mass of the particles tested.

Different diameter glass particles

Figures 2.22, 2.23 and 2.24 show the normalized probability density functions obtained for 2 mm glass particles in a 10.2 cm test section. It can be observed that in the PDF of the duration of collision, the position of the two distinct peaks moved to durations shorter than those found for the 3 mm glass particles.

Figures 2.25, 2.26 and 2.27 show the normalized probability density functions obtained for 4 mm glass particles in a 10.2 cm test section. The results show the same trends found in the case of 3 mm and 2 mm particles, although changes for

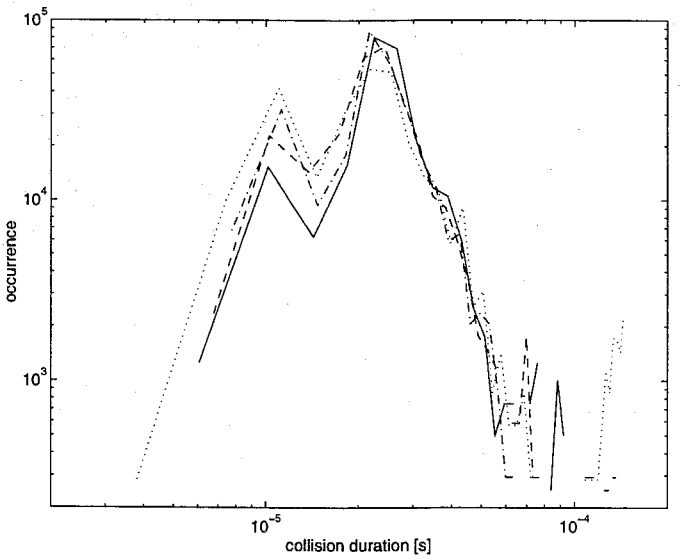

Figure 2.23: Probability density function of collision duration. Fluidized glass 2 mm particles in a 10.2 cm test section. (—) $\nu = 0.4435$, (– –) $\nu = 0.327$, (– · –) $\nu = 0.243$, (· · ·) $\nu = 0.181$.

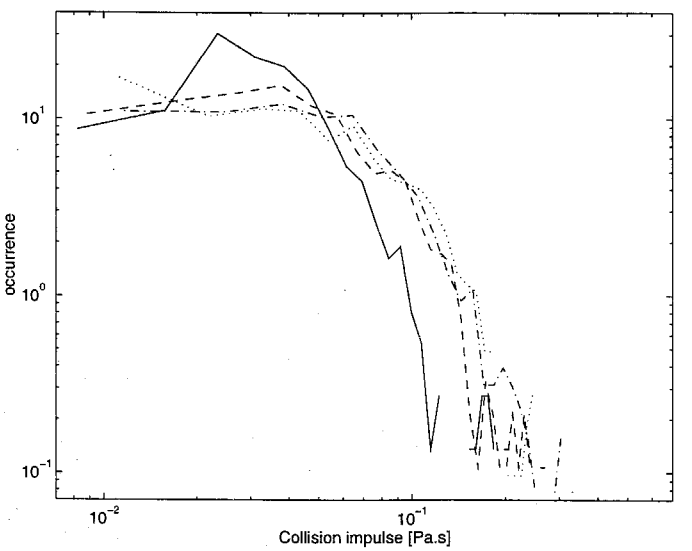

Figure 2.24: Probability density function of collision impulse. Fluidized glass 2 mm particles in a 10.2 cm test section. (—) $\nu = 0.4435$, (– –) $\nu = 0.327$, (– · –) $\nu = 0.243$, (· · ·) $\nu = 0.181$.

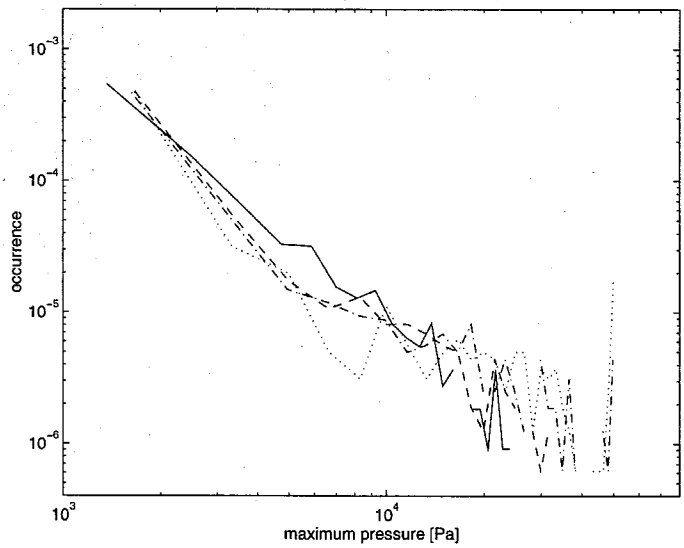

Figure 2.25: Probability density function of individual collision pressure. Fluidized glass 4 mm particles in a 10.2 cm test section. (—) $\nu = 0.481$, (−−) $\nu = 0.361$, (− · −) $\nu = 0.251$, (· · ·) $\nu = 0.115$.

different solid fractions are not as well observed as in the two previous cases. Again, the individual pressure and collision impulse measurements scale with the particle mass. Two distinct peaks were also found in the collision time distribution, occurring at 20 μs and 45 μs. In this case the long duration collisions agreed with the durations observed during the calibration tests.

The collision duration for the two types of pressure pulses (for the glass particles) varies with particle diameter according to

$$\frac{\tau_{2mm}^{sh}}{\tau_{3mm}^{sh}} \approx \frac{\tau_{2mm}^{lg}}{\tau_{3mm}^{lg}} \approx \frac{d_{2mm}}{d_{3mm}} \approx 0.666$$

$$\frac{\tau_{2mm}^{sh}}{\tau_{4mm}^{sh}} \approx \frac{\tau_{2mm}^{lg}}{\tau_{4mm}^{lg}} \approx \frac{d_{2mm}}{d_{4mm}} \approx 0.5$$

where the subscripts denote the particle diameter and the superscripts denote the type of collision. See appendix B for more details.

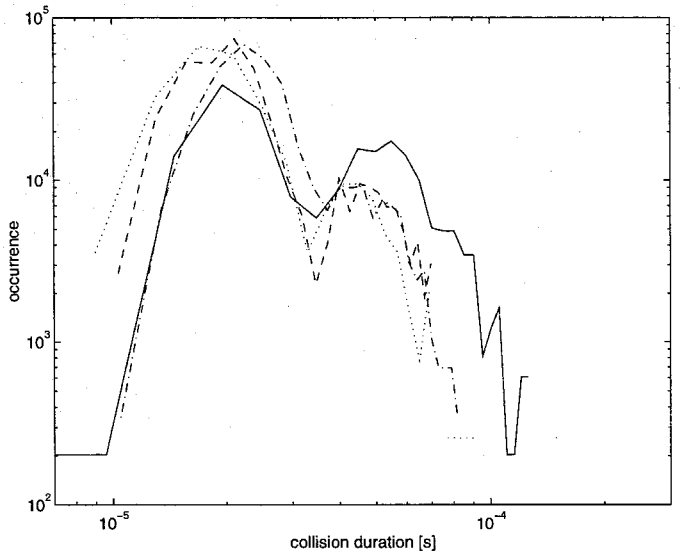

Figure 2.26: Probability density function of collision duration. Fluidized glass 4 mm particles in a 10.2 cm test section. (—) $\nu = 0.481$, (– –) $\nu = 0.361$, (– · –) $\nu = 0.251$, (· · ·) $\nu = 0.115$.

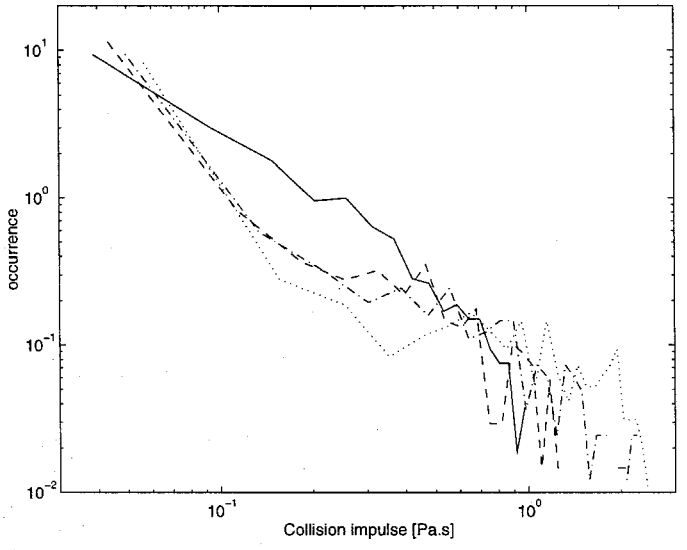

Figure 2.27: Probability density function of collision impulse. Fluidized glass 4 mm particles in a 10.2 cm test section. (—) $\nu = 0.481$, (– –) $\nu = 0.361$, (– · –) $\nu = 0.251$, (· · ·) $\nu = 0.115$.

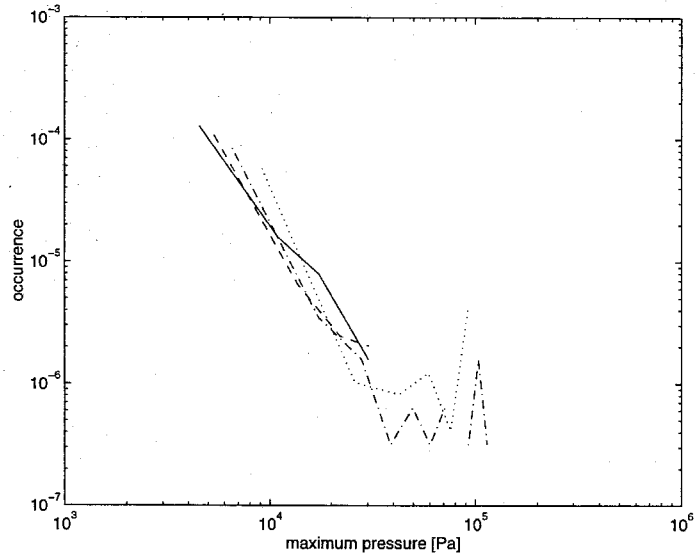

Figure 2.28: Probability density function of individual collision pressure. Fluidized steel 4.5 mm particles in a 5.1 cm test section. (—) $\nu = 0.568$, (– –) $\nu = 0.455$, (– · –) $\nu = 0.350$, (· · ·) $\nu = 0.172$.

Other particle densities

Figures 2.28, 2.29 and 2.30 show the normalized probability density functions obtained for 4.5 mm steel particles in the 5.1 cm test section.

Similar trends were observed in all of the PDF for steel particles. As expected, the magnitudes of the collision pressures and impulse pressure were, in general, larger than the values observed for any of the glass particles. In the case of the maximum pressure PDF the lines corresponding to different solid fractions were not significantly distinct from one another, as in the case of glass particles. However, it can be observed that large pressure impacts occur more frequently for low concentrations. The duration of the collisions were also larger than in the case of glass spheres. Two peaks were observed, although the short duration pulses appeared more readily than in the case of glass spheres for all solid fractions. The total number of short duration pulses was generally larger than in the case of glass spheres. However, the threshold level chosen determined the number of short duration pulses captured in a single run. If the threshold level had been left at the same level as in the case of glass spheres, the

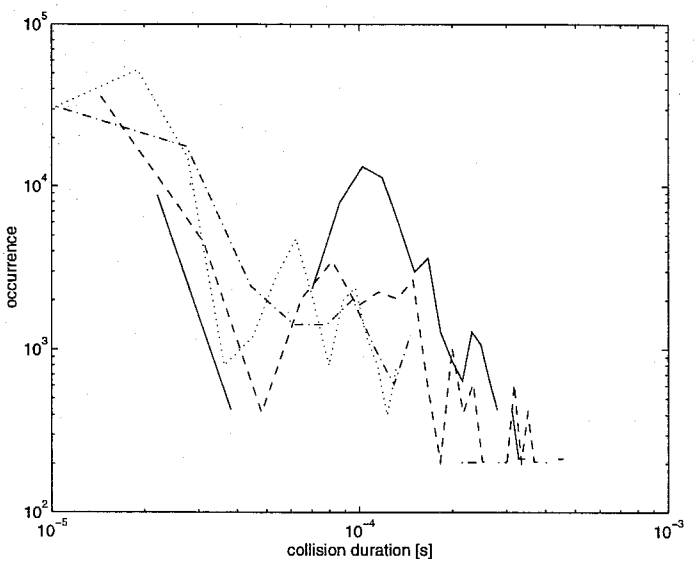

Figure 2.29: Probability density function of collision duration. Fluidized steel 4.5 mm particles in a 5.1 cm test section. (—) $\nu = 0.568$, (– –) $\nu = 0.455$, (– · –) $\nu = 0.350$, (· · ·) $\nu = 0.172$.

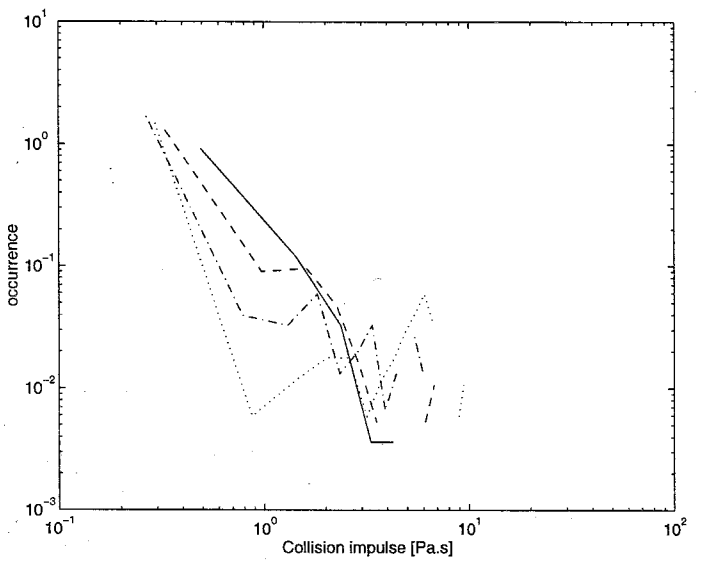

Figure 2.30: Probability density function of collision impulse. Fluidized steel 4.5 mm particles in a 5.1 cm test section. (—) $\nu = 0.568$, (– –) $\nu = 0.455$, (– · –) $\nu = 0.350$, (· · ·) $\nu = 0.172$.

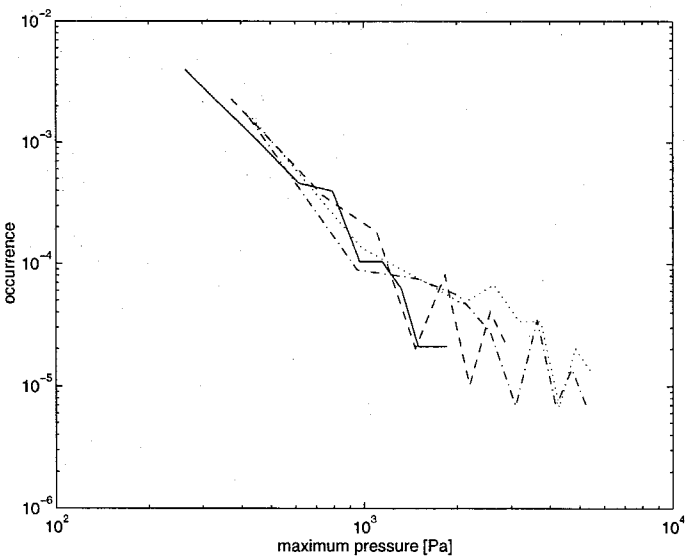

Figure 2.31: Probability density function of individual collision pressure. Fluidized nylon 6.35 mm particles in a 10.2 cm test section. (—) $\nu = 0.589$, (– –) $\nu = 0.434$, (– · –) $\nu = 0.2237$, (· · ·) $\nu = 0.134$.

number of short duration pulses would have dominated the set. This result shows the limitations of the data acquisition system.

Figures 2.31, 2.32 and 2.33 show the normalized probability density functions obtained for 6.35 mm nylon particles in the 10.2 cm test section.

The impulses for this case were smaller, and the duration of collisions larger, than in the case of glass particles. This was expected from Hertzian theory considerations. Although some of the shapes of the curves found are different than in the case of glass spheres, most characteristic features are preserved: a greater frequency of high impulse collisions at low solid fractions and two distinct peaks in the PDF of the collision duration. For this case the transducer is probably stiffer than the particles; therefore, the mechanisms producing the two distinct peaks in the collision duration PDF can be different than the ones for the glass or steel particles.

Figures 2.34, 2.35 and 2.36 show the normalized probability density functions obtained for 3.4 mm PVC rods in the 10.2 cm test section.

The same characteristics were observed for the rod-like PVC particles, with the exception of the PDF of the collision duration. In this particular case, the short

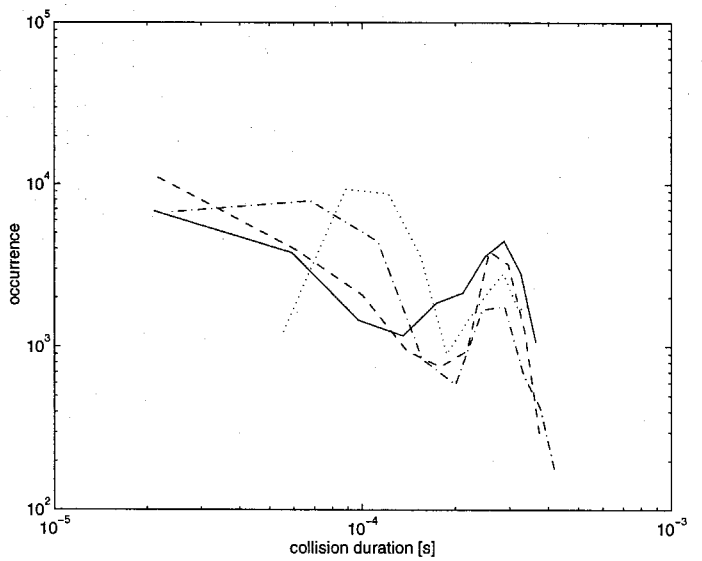

Figure 2.32: Probability density function of collision duration. Fluidized nylon 6.35 mm particles in a 10.2 cm test section. (—) $\nu = 0.589$, (– –) $\nu = 0.434$, (– · –) $\nu = 0.2237$, (· · ·) $\nu = 0.134$.

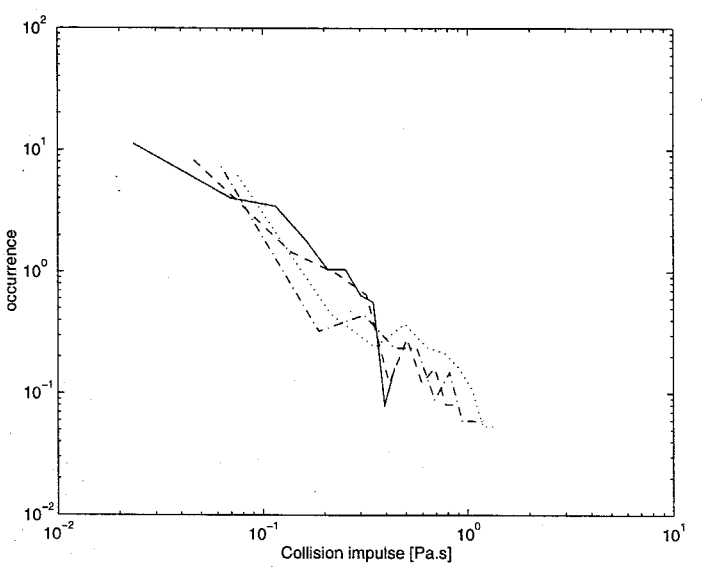

Figure 2.33: Probability density function of collision impulse. Fluidized nylon 6.35 mm particles in a 10.2 cm test section. (—) $\nu = 0.589$, (– –) $\nu = 0.434$, (– · –) $\nu = 0.2237$, (· · ·) $\nu = 0.134$.

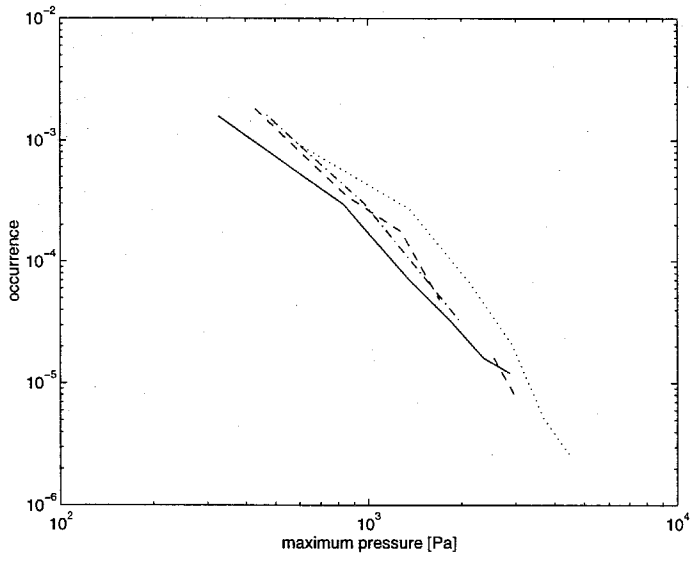

Figure 2.34: Probability density function of individual collision pressure. Fluidized PVC 3.4 mm rods in a 10.2 cm test section. (—) $\nu = 0.444$, (– –) $\nu = 0.341$, (– · –) $\nu = 0.2945$, (· · ·) $\nu = 0.771$.

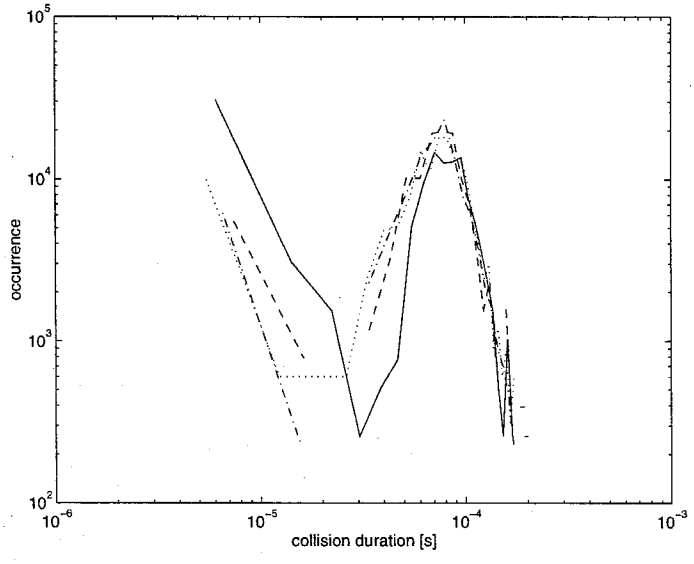

Figure 2.35: Probability density function of collision duration. Fluidized PVC 3.4 mm rods in a 10.2 cm test section. (—) $\nu = 0.444$, (– –) $\nu = 0.341$, (– · –) $\nu = 0.2945$, (· · ·) $\nu = 0.771$.

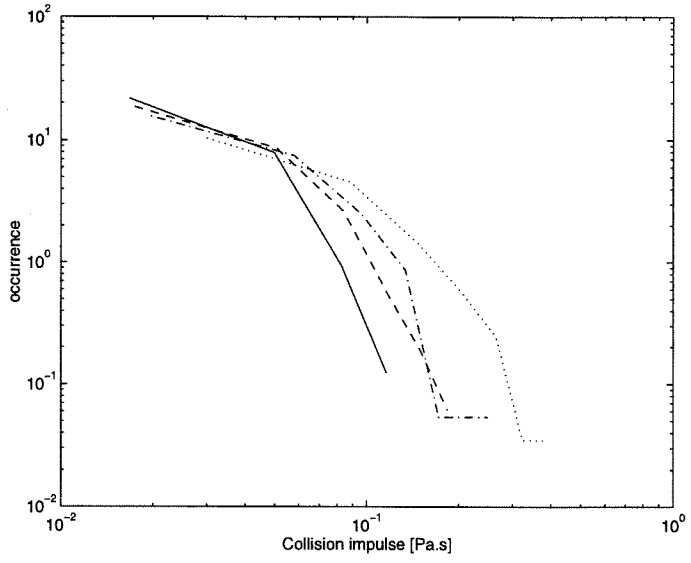

Figure 2.36: Probability density function of collision impulse. Fluidized PVC 3.4 mm rods in a 10.2 cm test section. (—) $\nu = 0.444$, (– –) $\nu = 0.341$, (– · –) $\nu = 0.2945$, (· · ·) $\nu = 0.771$.

duration events appear to decrease as solid fraction decreases (the opposite for all the other particles tested). It is important to note that these were the only non-spherical particles used in this investigation (the PVC rods were also the particles with the smallest mass per particle). The reason of different behavior could not be explained. It is probably a result of both the non-sphericity of the particle an the soft nature of these particles. A detailed visualization[3] can be performed to resolve these issues.

Contribution of the different pressure pulses to the total particle pressure

Figure 2.37 shows a comparison between the total particle pressure (solid line) and the contribution to the particle pressure from the long duration collisions (dashed line). This plot shows typical results obtained for 3 mm glass particles in the 10.2 cm test section. Though the short duration collisions may have occurred as frequently as the long duration collisions, their contribution to the average particle pressure was less than 5%, for all solid fractions.

[3]similar to the one presented in section 2.7

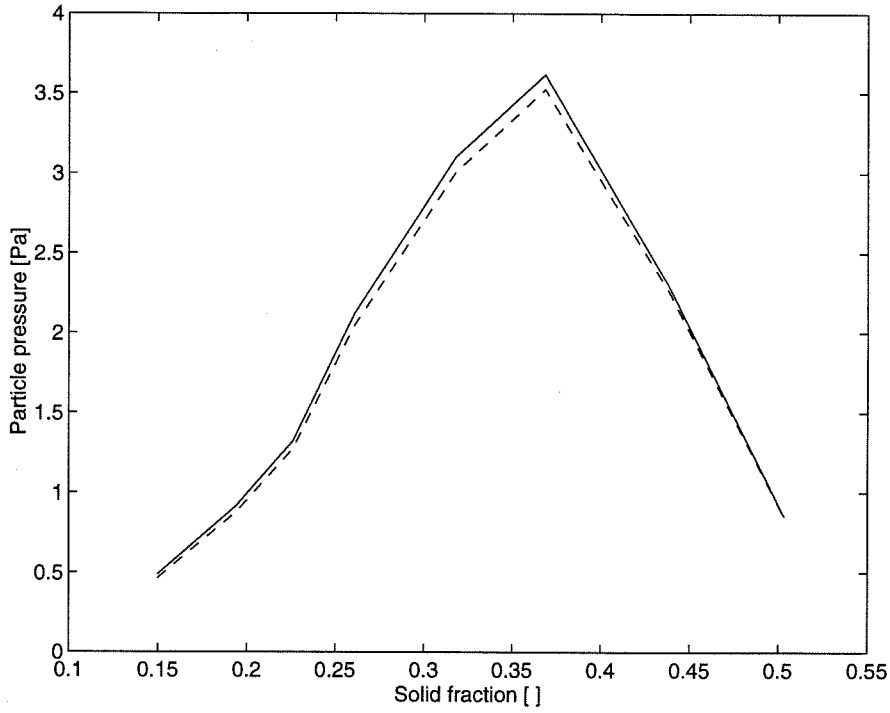

Figure 2.37: Particle pressure as a function of solid fraction, a comparison between the total particle pressure (—) and the particle pressure generated solely by the long duration collisions (– –). Fluidized glass 3 mm particles in the 10.2 cm test section.

2.7 Components of the collisional particle pressure

In the analysis of the probability density functions of collision duration two different characteristic pressure pulses were encountered: a long duration pulse whose duration and strength corresponded to those predicted by the Hertzian theory of contact, and a short duration pulse whose duration and strength were not in accord with Hertzian predictions. Several features of the short duration pulses were evident from the particle pressure measurements: their strength and duration are both smaller than those predicted by Hertzian theory; their occurrence increases as the solid fraction decreases (for the case of a fluidized bed); they occur at least as often as the long duration collisions (for the case of vertical flows); they were not observed when calibrating the transducers.

In the gravity-flow experiments, the short-duration pressure pulses were, in general, more frequent than in the fluidized bed experiments. The short-duration events

constituted up to 75% of the total number of events in the gravity flow experiments as compared to a maximum of 50% in the fluidized beds.

A number of different explanations of the origin of these short duration pulses were explored. One early hypothesis was that the short pulses were the result of a sliding contact of the particle against the face of the transducer. Such contact at a very acute incidence angle would have generated lubrication forces that would act as a reaction mechanism reducing the contact time with the transducer. Another thought was that a particle contacting the surface with a significant amount of spin could generate a similar lubrication reaction force at the moment of contact. Another possibility was a multi-particle interaction mechanism. A particle in the process of contacting the transducer could have been knocked off by another particle passing nearby, or could have been interrupted in the process of contact by some fluctuating motion of the fluid phase. However, for all these explanations a fairly broad distribution of such events in the probability density functions would be expected. The discrete peaks observed seem to contradict these thoughts.

The origin of the short duration pulses was not resolved until a detailed visualization of the particles was performed. The experimental setup employed to visualize the moving particles is shown in figure 2.38. An observation window was installed near the pressure transducer. A high speed digital camera, able to record images as fast as 500 frames per second, was positioned to observe the face of the transducer. The camera was synchronized with the data acquisition system so that images of the events occurring on the face of the transducer were filmed at the moment at which a pressure pulse was sensed. With this setup the pressure pulse obtained could be correlated with the motion of the particles interacting with the transducer. Clear images of the motion of the particles interacting with the transducer could, however, only be obtained for dilute fluidized beds. Many long and short pressure pulses were recorded and analyzed.

The long duration pulses were confirmed to be the result of direct contacts with particles against the transducer. Particles were observed to collide against the face of the transducer at many different speeds and incident angles. The strength and dura-

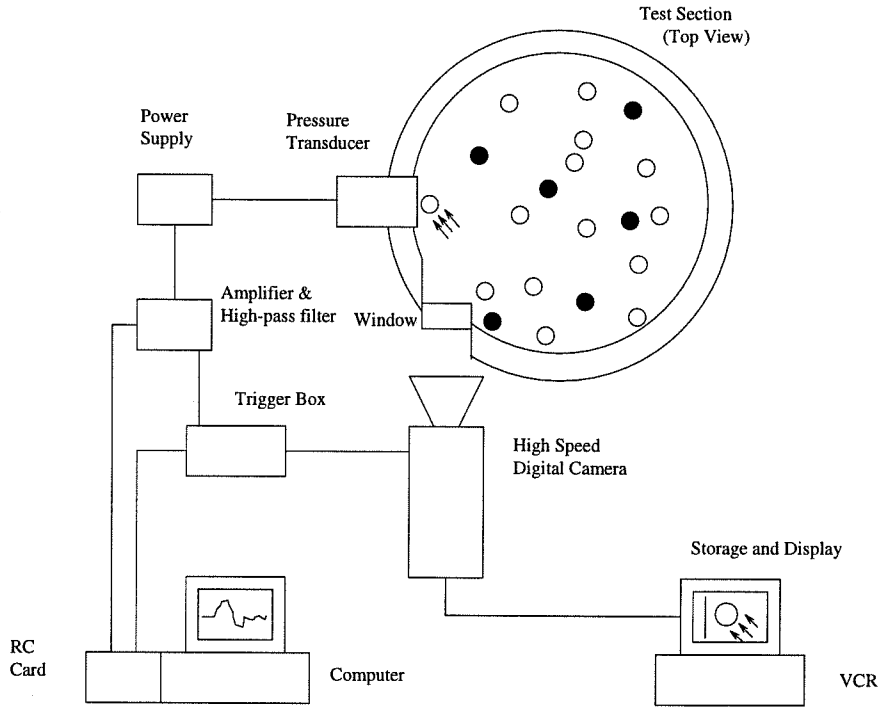

Figure 2.38: Schematic of experimental setup used to obtain the images of the moving particles and pressure pulses simultaneously.

tion of these collisions were confirmed to be in accordance with Hertzian predictions. A sequence of images of a typical direct collision of a particle in a liquid fluidized bed obtained using the high speed video camera is shown in figure 2.39. It can be observed clearly that the particle hit the transducer on the active surface, which produced a pressure pulse of the first kind, of long duration and high impulse. Note that the particle is in direct contact with the transducer at $t = 0$. A more complete study of immersed particle collisions is presented in Chapter 3.

The short duration events were found to be produced not by actual contacts between particles and the transducer, but rather by collisions between particles in the bulk that occur in the vicinity of the pressure transducer without having physical contact with it. The pressure pulse produced by the collision traveled from the point of occurrence to the transducer through the interstitial fluid. The intensity of these pulses appeared to be related to the impact velocity of the collision, the orientation of the colliding particles with respect to the transducer and the distance from the collision to the transducer. The duration of these events differ from the direct impacts

(a) t=-4 ms

(b) t=-2 ms

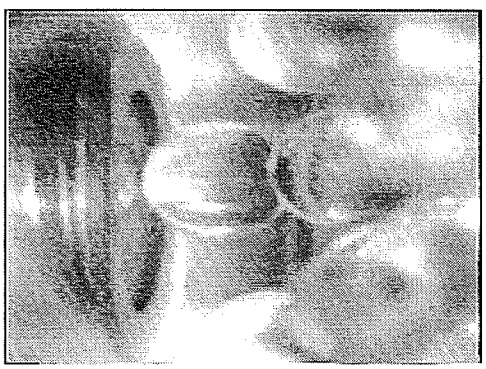

(c) t=0

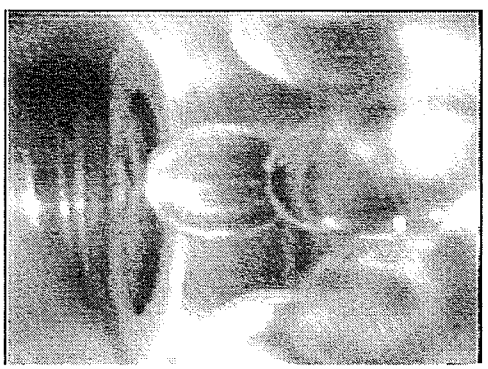

(d) t=2 ms

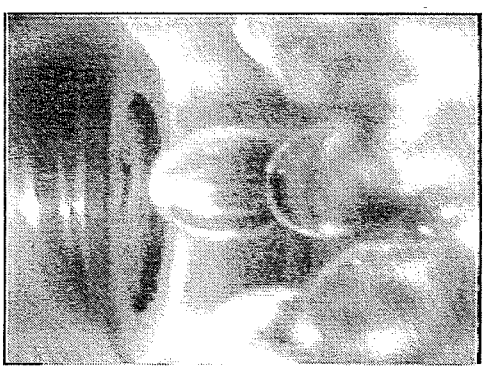

(e) t=4 ms

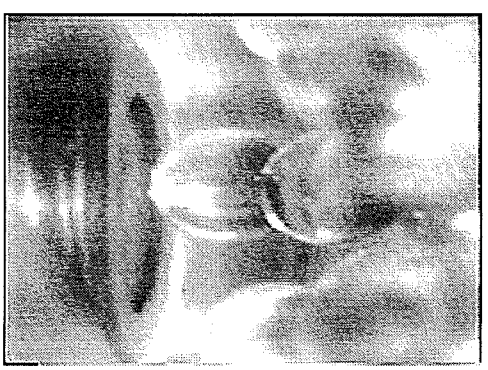

(f) t=6 ms

Figure 2.39: Sequence of images of pressure transducer obtained through view window. A typical long duration pressure pulse: a direct collision of a particle on the surface of the transducer. 3 mm glass fluidized particles in 5.1 cm test section. $\nu \approx 0.05$.

because two particles are colliding rather than a single particle with a flat surface. Figure 2.40 shows a series of images obtained when a short duration and low impulse pressure pulse was captured. The pressure front is generated due to the impulsive acceleration imposed to a particle during the collision event. A detailed analysis of the nature of these pressure pulses can be found in 4.

It can be concluded from these observations that the particle pressure is generated by two distinct mechanisms: one the result of direct impacts of particles, and a second one by pressure pulses transmitted through the fluid generated by particle interactions. Figure 2.41 illustrates these processes diagrammatically.

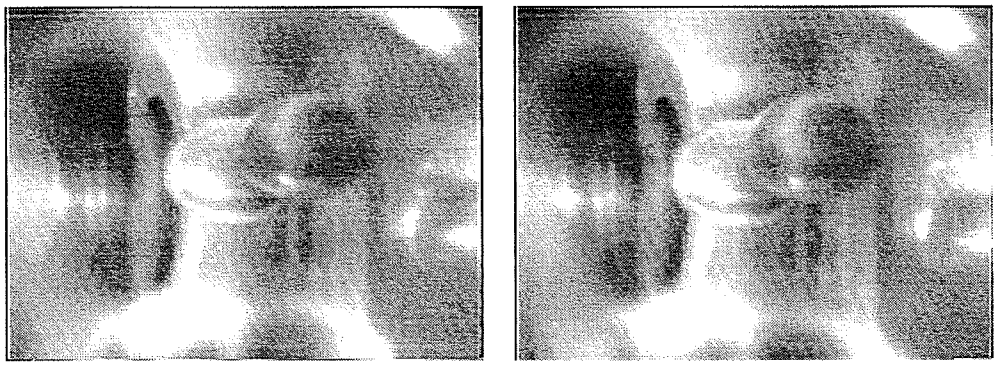

(a) t=-4 ms (b) t=-2 ms

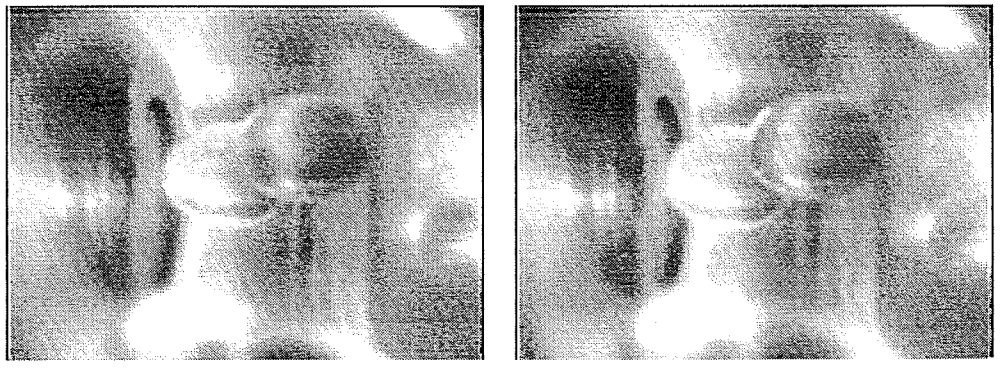

(c) t=0 (d) t=2 ms

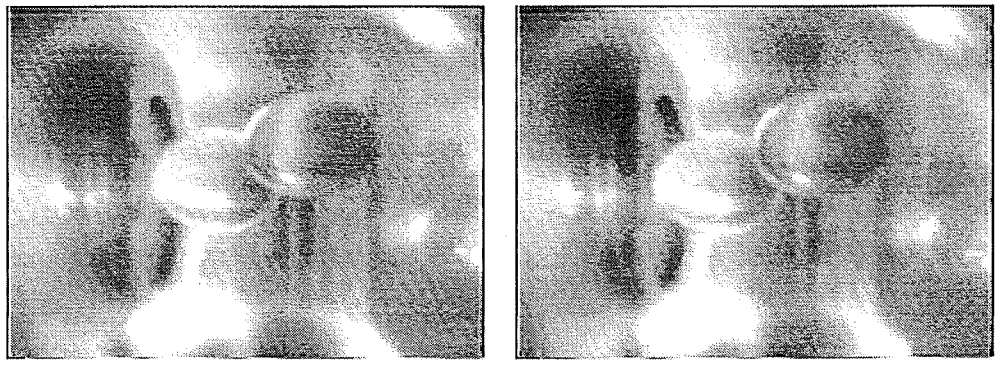

(e) t=4 ms (f) t=6 ms

Figure 2.40: Sequence of images of pressure transducer obtained through view window. A typical short duration pressure pulse: impulsive acceleration of a particle near the transducer. 3 mm glass fluidized particles in 5.1 cm test section. $\nu \approx 0.05$. Note that at zero time the particle is not in contact with the transducer.

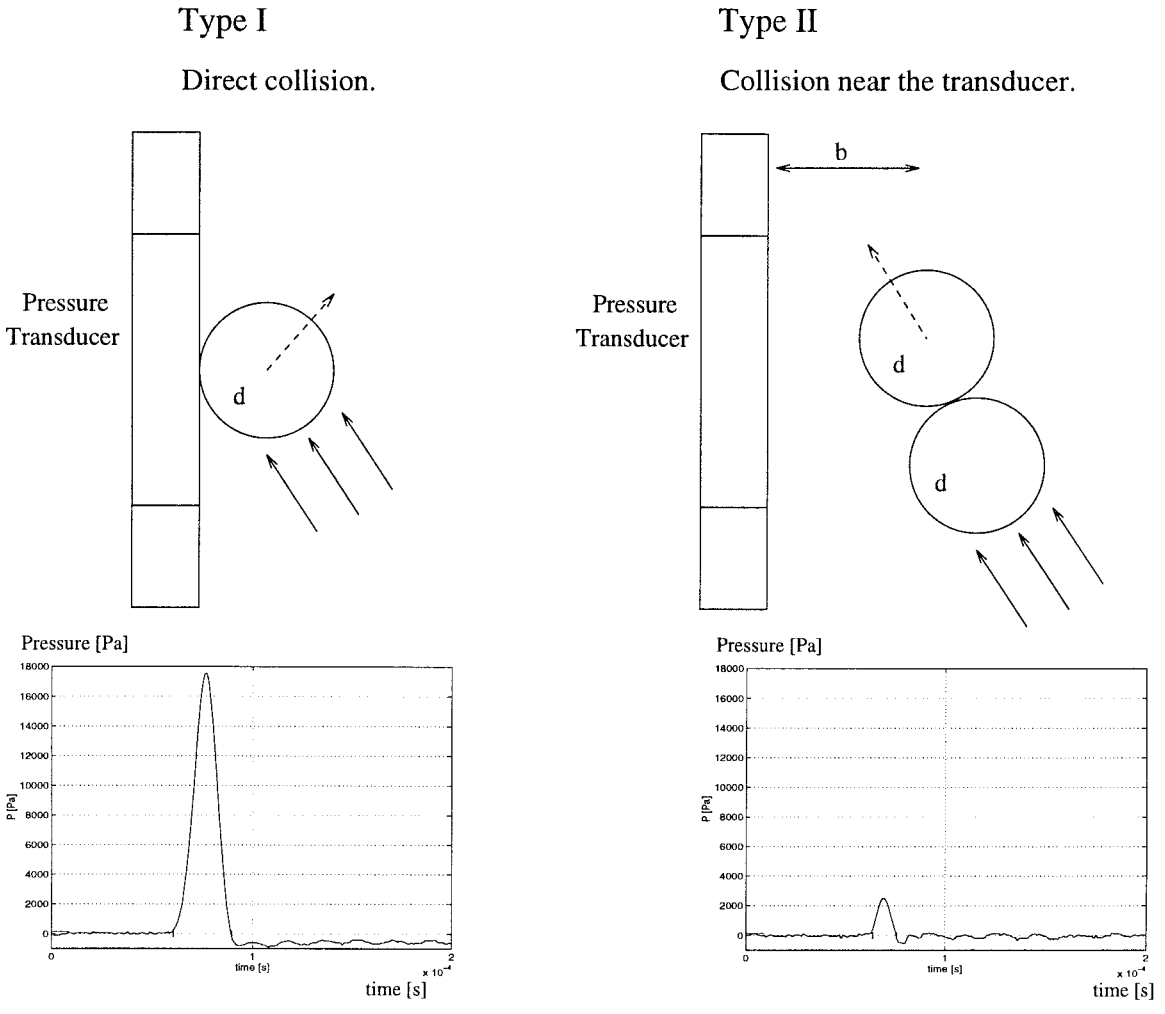

Figure 2.41: Types of pressure pulses that contribute to the particle pressure. Sketch of the collisions and type of pressure pulse recorded. The solid arrows represent the motion before contact, and the dashed arrows, the motion after contact.

Chapter 3 Mechanics of immersed particle collisions

3.1 Introduction

The collisional component of the particle pressure in liquid-solid flows was found to be the result of particle collisions with themselves and the boundaries.

The direct impact of particles against the containing walls is the most significant contribution to the particle pressure. During a collision the approaching particle exerts a certain force on the wall. This force is in general a function of the impact velocity, the mass of the particle and, in the case of an immersed collision, on the properties of the fluid.

Dry collisions have been studied since the beginning of the century (Johnson, 1985; Goldsmith, 1960). The mechanics of contact are well established, and rebound and energy losses can be modeled for most simple cases with few exceptions (see Tüzün and Walton, 1992). The mechanics of liquid immersed collisions are still a matter of current research. When a particle approaches a rigid planar surface, or another particle, there is a fluid film that has to be drained out for contact to take place. A pressure build up is generated due to the squeezing of the fluid in the gap between the surfaces. In this process a certain amount of the initial kinetic energy is dissipated or transferred to the fluid, resulting in the slowing of the particle. Depending on how much of the kinetic energy of the particle is lost during the approach and contact processes, the contact may or may not result in a rebound.

The purpose of this chapter is to analyze particle collisions occurring in a liquid environment. By means of a set of relatively simple experiments, spheres of various diameters and materials submerged in water are made to impact a wall. Measurements of the particle position and velocity are obtained for various impact velocities.

The impulse pressure produced by the particle collision is measured using a dynamic high-frequency response pressure transducer. Additionally, a simple collision model to account for the effect of the fluid is presented. Comparisons between the results of the model and the experimental measurements show good agreement.

3.1.1 The impact paradox

Many researchers have studied the problem of immersed collisions. Moments before contact the gap between the particle and the wall is very small. Presumably, in such a situation the Reynolds number of the flow[1] is small. If the Reynolds is small enough that the creeping flow approximation can be assumed, the flow can be resolved (Happel and Brenner, 1965). By calculating the pressure profile in the gap between the particle and the wall, the net force exerted by the fluid on the particle can be predicted. When the gap tends to zero, the predicted force grows infinitely, therefore predicting that direct contact never occurs. Consequently, it is not possible to predict a rebound velocity under this assumption.

Modifications to the creeping flow approximation can be performed. If the approaching surfaces allow elastic deformation resulting from the hydrodynamic pressure built up, an elastohydrodynamic model can be formulated (Lian *et al.* , 1996; Davies *et al.* , 1985). In this case some of the kinetic energy is stored as elastic deformation and, therefore, rebound is possible. However, physical contact between the two surfaces does not occur.

On the other extreme, if the flow around the particle approaching a wall could be assumed to be inviscid and irrotational, the hydrodynamic force on the sphere can be calculated in the form of added masses and the flow can be resolved in a non-explicit form in terms of an infinite series of doublets (Milne-Thomson, 1950). Landweber & Shahshashan (1992) obtained a simplification that allows the accurate calculation of the hydrodynamic forces when the two surfaces are very close to each other. In this case, also, the hydrodynamic force is found to grow unbounded when the distance

[1] based on the gap thickness

between the two surfaces tends to zero. This effect is mainly due to the discontinuity of the velocities between the moving particle and the stationary plane.

The question remains. What really happens when the distance between the two surfaces tends to zero? It is expected that if the velocity of approach is small, the viscous effects would dominate, and therefore most of the kinetic energy would be dissipated in viscous friction. But in the case when the velocity of approach is large, it has been experimentally observed that particles come into 'apparent contact' and rebound freely (McLaughlin, 1968; Zenit & Hunt, 1997). In the case of particles colliding immersed in a gas, the phenomena have been explored assuming that the continuum mechanics assumptions are no longer valid when the gap distance is comparable with the mean free path of the gas molecules (Sundararajakumar and Koch, 1996; Hocking, 1973). In the case of a liquid, the mean free path is practically zero and the continuum assumptions are expected to hold up to distances of tens of molecular diameters. Some researchers have argued that contact takes place through the surface roughnesses that stick out beyond the lubrication layer critical distance. However, from the continuum mechanics point of view, in a liquid the characteristic length of the roughnesses are still much larger than the mean free path of the molecules. The contact between surface roughnesses is, therefore, also impossible.

Some studies have suggested that under the compression levels generated during a collision, the liquid in the gap 'locks up' for a brief time period behaving like a solid (Ballamudi *et al.* , 1994), and therefore transmitting the collision pressure between surfaces without physical contact.

3.2 Experimental measurement of immersed collision properties

Although there have been attempts to model immersed collisions, the results obtained have been diverse. Studies with detailed experimental measurements have been rare (Lundberg *et al.* , 1992; Barnocky and Davis, 1988; McLaughlin, 1968).

The following section describes the experiments performed to measure velocities and collision impulses for particle-wall and particle-particle collisions immersed in a liquid. The results obtained can be utilized to further understand the generating mechanisms of the particle pressure, and to gain fundamental understanding of the factors that determine particle approach and rebound in immersed situations. The results obtained from this study could potentially be used in computer simulations of multi-phase flows.

3.2.1 Experimental setup

To obtain measurements of the velocity and impulse of a particle approaching and colliding with a wall, a simple pendulum experiment was built. A schematic of the experimental setup is shown in figure 3.1. A fine string was attached to a particle starting from rest at some initial angle, θ_i. On the wall, at $\theta = 0$, a high-frequency response pressure transducer was flush mounted. A suction system was used to position the particle and release it from rest with no rotation. Once released, the particle accelerated towards the pressure transducer. The motion of the particle was recorded using a high speed digital camera, able to record images as fast as 500 frames per second. A typical multi-exposure picture is shown in figure 3.2. When the collision was sensed by the pressure transducer, the trigger system activated the digital camera. The images were digitally processed to calculate the centroid of the particle for different times. The velocity was calculated from the displacement of the particle centroid between consecutive images. A typical collision pressure signal is presented in figure 3.3.

The calibration provided by the manufacturer of the high-frequency response pressure transducer was used. This was corroborated by comparing the results of dry impacts with Hertzian theory predictions (see Chapter 2). The properties of the particles used in the experiments are presented in table 3.1.

To verify the velocity measurements obtained by this technique, calibration measurements were taken for a swinging immersed pendulum with no colliding wall. A

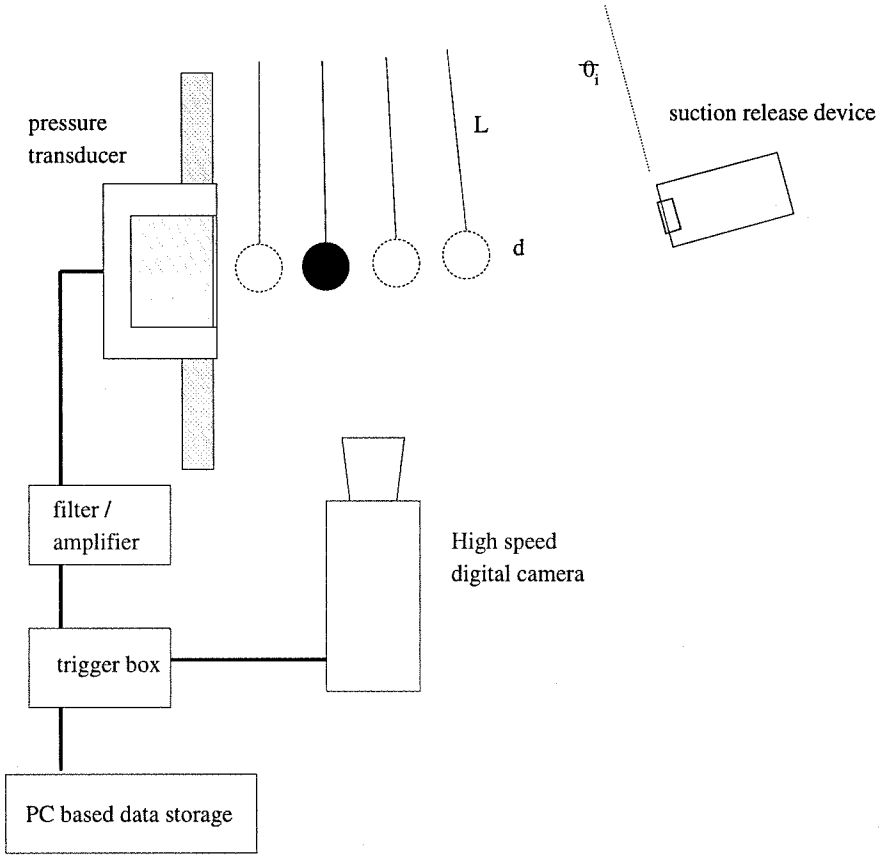

Figure 3.1: Experimental setup.

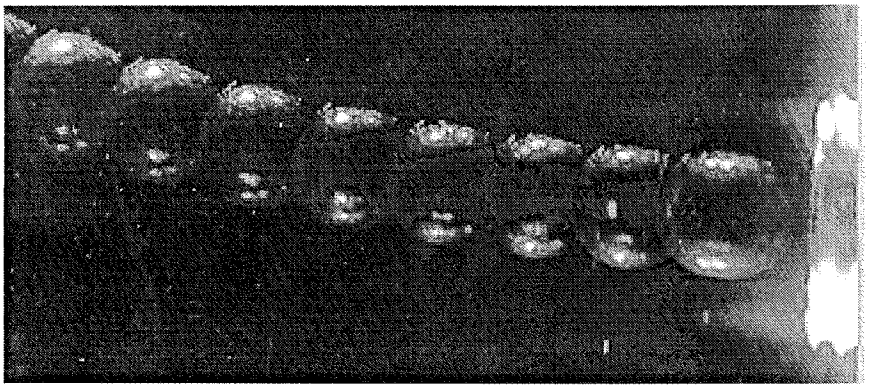

Figure 3.2: Typical collision (picture). 4.5 mm steel particle in water. Only approach shown.

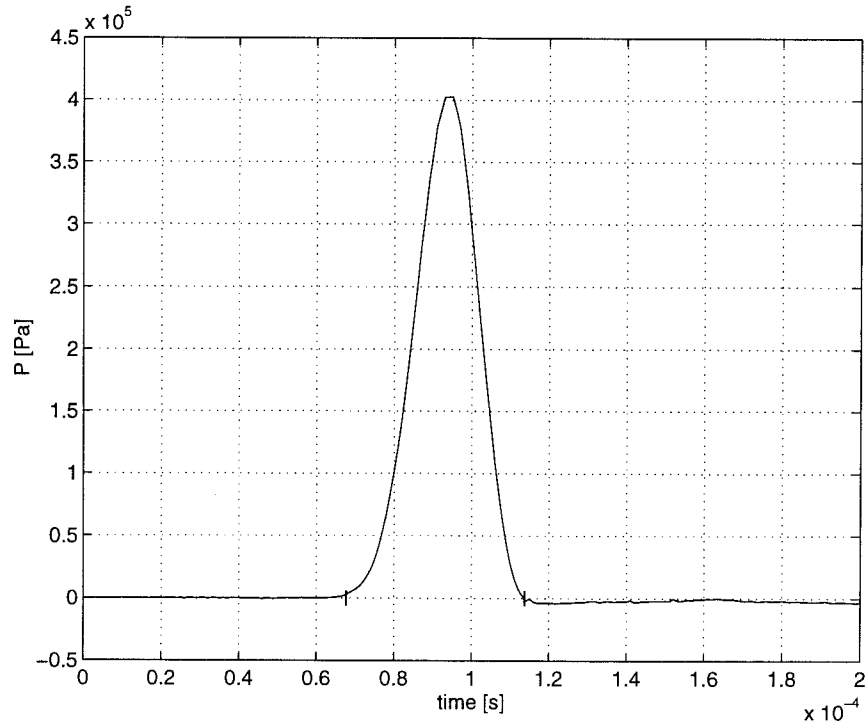

Figure 3.3: Typical collision (pressure pulse). 4.5 mm steel particle in water.

Table 3.1: Properties of particles used in direct collisions experiments.

Material	$d_p[mm]$	ρ_p/ρ_w	$u_t[cm/s]$	Re_t
Glass $\times$	3.00	2.54	31.8	954
Glass $*$	3.96	2.54	36.8	1338
Glass $\circ$	6.00	2.54	47.4	2583
Steel $\oplus$	4.50	7.78	89.6	3665
Nylon $\otimes$	6.35	1.14	13.6	785

particle was released from an initial angle and photographed for part of one oscillation cycle. The measurements were then compared with a prediction of a model by Mei (1994). Mei proposed expressions for the unsteady drag on a sphere at *finite* Reynolds number. The proposed form of the total unsteady drag on a moving particle immersed in a stagnant fluid is

$$\begin{aligned} f(t) &= \frac{4}{3}\pi a^3(\rho_p - \rho_f)g - 6\pi\mu a v\phi(t) \\ &\quad -6\pi\mu a^2 \int_{-\infty}^{t} K(t-\tau)\frac{dv}{d\tau}d\tau \\ &\quad -\frac{2}{3}\rho_f \pi a^3 \frac{dv}{dt} \end{aligned} \tag{3.1}$$

where ρ_p and ρ_f are the densities of the solid particle and the fluid respectively, v is the velocity of the particle, $\phi(t)$ is a drag force function, $K(t)$ is the history force kernel and a is the radius of the particle. This expression was incorporated in the equation of motion of an immersed pendulum

$$\begin{aligned} \frac{4}{3}\pi a^3 \frac{\partial^2 s}{\partial t^2} &= \frac{4}{3}\pi a^3(\rho_p - \rho_f)g\sin s/L + 6\pi\mu a\phi(t)\frac{\partial s}{\partial t} \\ &\quad -6\pi\mu a^2 \int_{-\infty}^{t} K(t-\tau)\frac{\partial}{\partial \tau}\left(\frac{\partial s}{\partial t}\right)d\tau \\ &\quad -\frac{2}{3}\rho_f \pi a^3 \frac{\partial^2 s}{\partial t^2} \end{aligned} \tag{3.2}$$

where s is the arc-length position, and L is the length of the pendulum string. This equation is then solved numerically. Figure 3.4 presents a comparison of the predicted phase plot with the experimental results obtained for a steel particle of 4.5 mm of diameter with a pendulum length of 10.5 cm. Several experimental runs were taken under the same nominal conditions. The experimental results are within 5% error. Errors arise from the difficulty of determining the centroid of a particle with a discrete number of pixels. No attempt was made to account for the drag force exerted on the string since its effect was negligible for most of the particles.

With this prediction the maximum impact velocity, the velocity at $\theta = 0$, can be obtained. Since the model does not account for the effects of the wall, the predicted

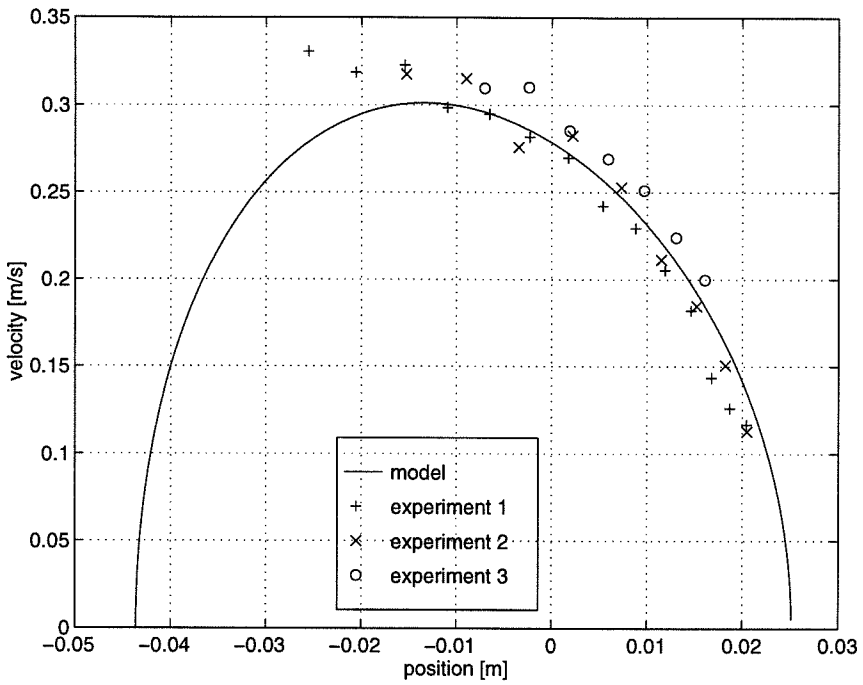

Figure 3.4: Comparison of the phase plot predicted by Mei (1994) and experimental measurements.

impact velocity is overestimated. This velocity represents a maximum value of the impact velocity, and is a function of the initial angle of release of the particle.

The strength of the collision was measured with a high-frequency response pressure transducer. In general, the magnitude and duration of a collision depend on the elastic properties of the colliding surfaces, impact velocity and the mass of the particle and, in this case, also on the fluid properties. Before actual contact between the solid surfaces occurs, a pressure build up is generated due to the squeezing of the fluid in the gap between the surfaces.

Figure 3.5 shows a comparison of a typical collision for a 4.5 mm steel particle against the prediction from Hertzian theory, which is used as a reference. The prediction is matched by choosing an impact velocity that would predict the same maximum pressure. Tabulated elastic properties of the particle are used ($E_{st} = 200GPa, \alpha_{st} = 0.26$). The maximum pressure and the impulse predicted from Hertzian theory represent the maximum limiting values for an ideal collision in which the fluid has no effect and the surfaces are smooth and perfectly elastic.

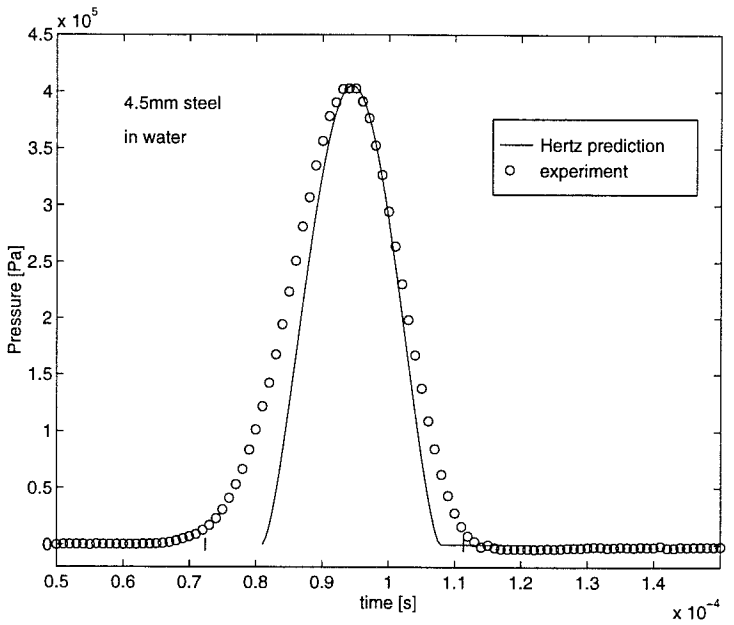

Figure 3.5: Comparison of the pressure pulse generated by a steel particle with the prediction from Hertzian theory. Data for a 4.5 mm steel particle, immersed in water.

While the Hertzian prediction is symmetric with respect to the point of maximum pressure, the experimental pressure pulse is wider and slightly asymmetric. This could be interpreted as the pressure build up due to the presence of the fluid. Before the solid surfaces come into contact, a considerable hydrodynamic pressure is exerted on the surface of the transducer. Additionally, the experimental measurement might deviate from the prediction due to the many assumptions made in the theory of Hertz (e.g., smooth surfaces, perfectly elastic properties, etc.).

3.3 Particle-wall collisions

3.3.1 Approach velocities

The velocity of approach was measured and compared with the predictions from the immersed pendulum for several cases. Phase plots of three different particles are shown in figures 3.6, 3.7 and 3.8.

Figure 3.6 presents the phase plots obtained for a 6 mm glass particle immersed in water. The horizontal axis represents the nondimensional distance from the wall

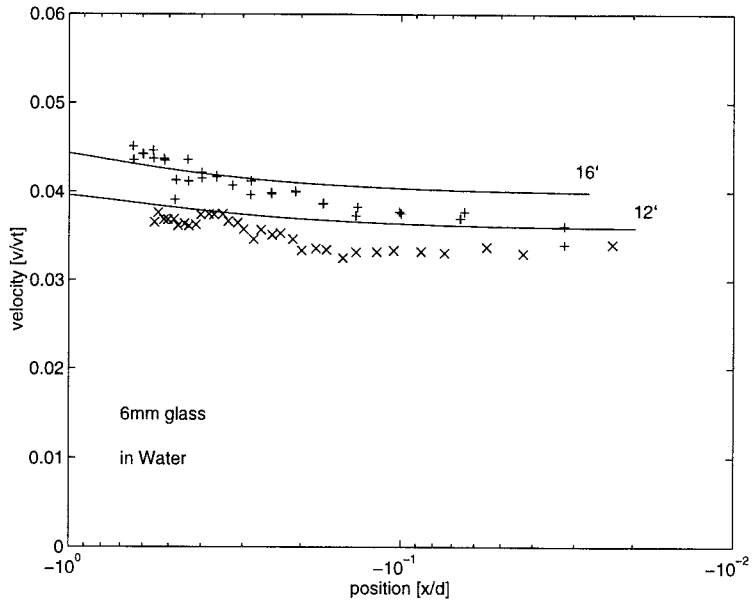

Figure 3.6: Phase plot for a 6 mm glass particle immersed in water. (+) $\theta_i = 16^o$; (×) $\theta_i = 12^o$.

($x/d = 0$ represents the position of the wall). The vertical axis represents the particle nondimensional velocity (u/u_t) along the pendulum trajectory. Two different starting angles are shown (12° and 16°). The solid lines represent the prediction from the pendulum model using equation 3.1. The measured velocity appears to agree well with the prediction up to half a diameter away from the wall. The effects of the wall can be observed at about half a diameter away from the wall, where the velocity prediction from the pendulum equation appears to overestimate the experimental measurements.

Figure 3.7 shows the measurements obtained for a 4.5 mm steel particle. The deviation between the prediction and the experimental measurements becomes important approximately one quarter of a diameter away from the wall.

Figure 3.8 presents results obtained for a 6.35 mm nylon particle. The experimental results differ substantially from the prediction in the vicinity of the wall. In general, the prediction from the pendulum equation is closer to the experimental results when the particle Reynolds number, Re_t (based on the terminal velocity in water u_t), is larger than 2000. The effect of the string may also become important as

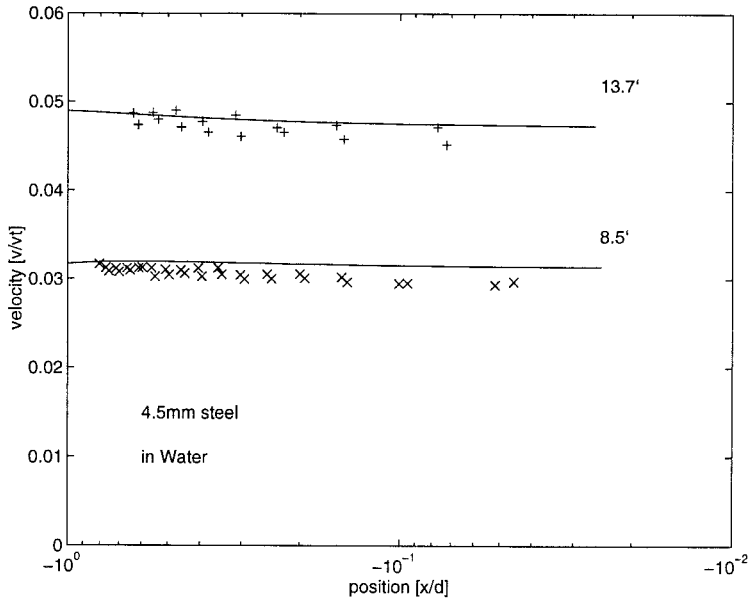

Figure 3.7: Phase plot for a 4.5 mm steel particle immersed in water. (+) $\theta_i = 13.7°$; (×) $\theta_i = 8.5°$.

the mass of the particle decreases.

3.3.2 Rebound and coefficient of restitution

Measurements of the rebound velocity were obtained. Since both the approach velocity and the rebound velocity were calculated, the coefficient of restitution can be determined. The coefficient of restitution in the normal direction is defined as

$$\epsilon = -\frac{u_\tau}{u_a} \tag{3.3}$$

where u_τ is the rebound velocity and u_a is the approach velocity.

It is important to note that the velocity of the particle changes significantly in the moments before and after contact. One must be careful to decide when and where the u_τ and u_a velocities are measured. Figure 3.9 presents a typical result of the particle position as a function of time. For this case the particle was a 6 mm glass particle released from an initial angle of 15°. The slope of this curve is the velocity of

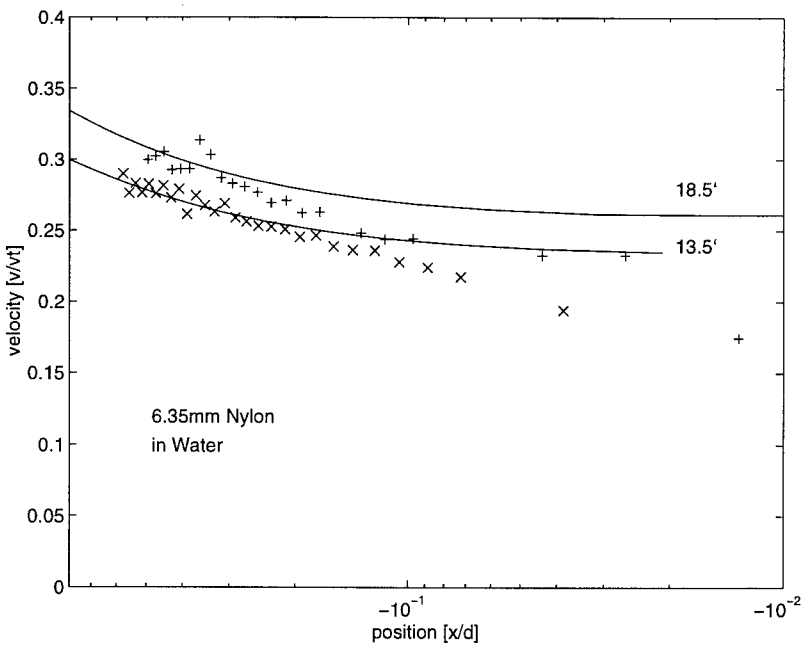

Figure 3.8: Phase plot for a 6.4 mm nylon particle immersed in water. (+) $\theta_i = 18.5^o$. (×) $\theta_i = 13.5^o$.

the particle. The curve's maximum represents the point of collision. The slope of the curve is nearly constant before the collision, decreasing only moments before contact. The rebound after contact appears in the plot as a change in the sign of the slope. Figure 3.10 shows the velocity-time history of the same experiment. The velocity was calculated simply by measuring the displacement of the geometric center of the particle image between consecutive frames. For this particular case the framing rate of the imaging system is 500 frames per second; therefore, the time resolution is 2 ms. The duration of a particle collision lasts only in the order of tens of microseconds. Hence, the exact moment of contact cannot be captured. A very interesting feature should be noted: after the particle has rebounded from the wall, its velocity continues to increase. In a dry collision the maximum velocity of rebound occurs at the moment when the particle loses contact with the wall. In the case of an immersed collision, the fluid appears to accelerate the particle moments after it has lost contact with the wall. It is important to mention that this particle post-rebound acceleration is not always observed. It appears to be more noticeable in the case of higher impact

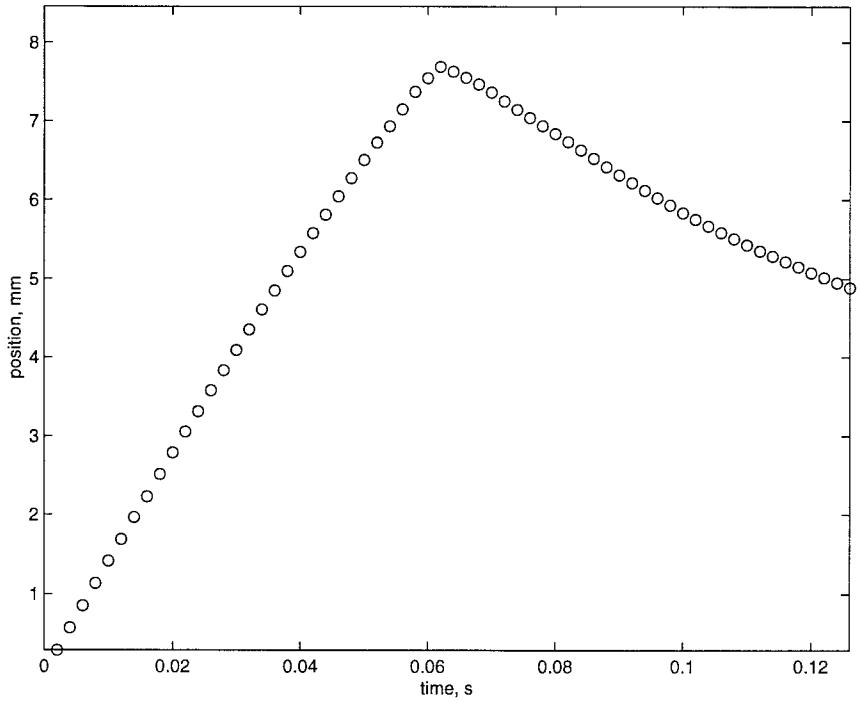

Figure 3.9: Typical time history of a 6 mm glass particle position colliding and rebounding against a flat surface, immersed in water.

velocities; however, if the particle velocity is too large, the time resolution of the imaging system may not be high enough to capture the rapidly changing velocities.

Figures 3.11 to 3.14 show typical cases of particle positions and velocities as function of time. On the left, the positions are shown as a function of time, and on the right the calculated velocities for the same data are shown. The different symbols represent experiments starting from different initial angles.

Figure 3.11 shows the results obtained for a 4.5 mm steel particle. It can be observed that the velocity of the particle is affected by the presence of the wall only a couple of data points (from 2 to 4 ms) before collision occurs. The effect of the wall appears to affect the trajectory of the particle only very few moments before and after contact. As expected higher approach velocities produce higher rebound velocities.

Figure 3.12 shows the positions and velocities measured for the case of a 6 mm glass particle. In this case the velocity is observed to decrease at greater distances from the wall. The particle acceleration after losing contact with the wall is clearly

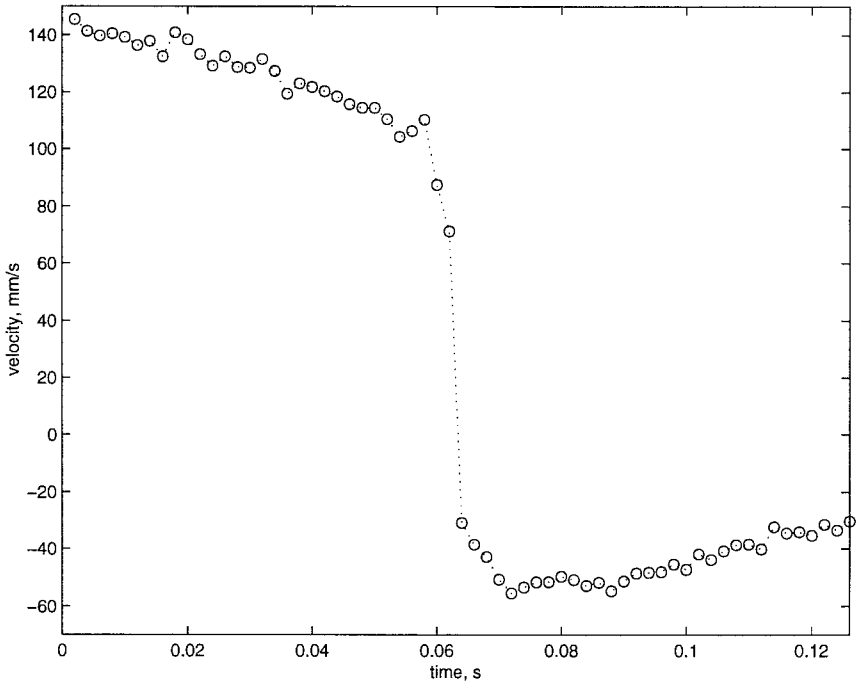

Figure 3.10: Typical time history of a 6 mm glass particle velocity colliding and rebounding against a flat surface, immersed in water.

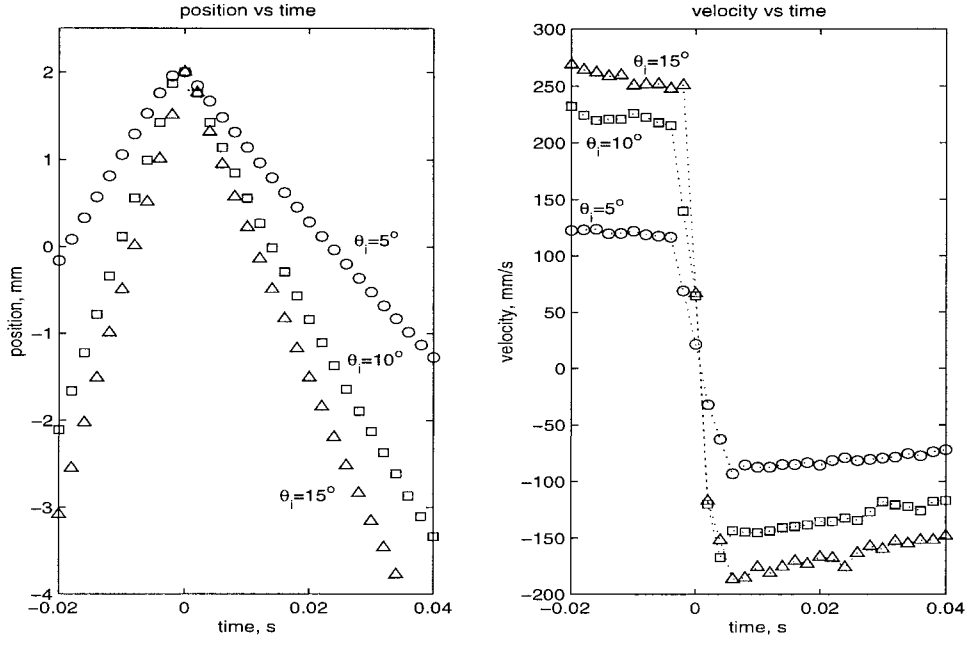

Figure 3.11: Particle position and velocity as a function of time for a 4.5 mm steel particle in water, for various initial release angles.

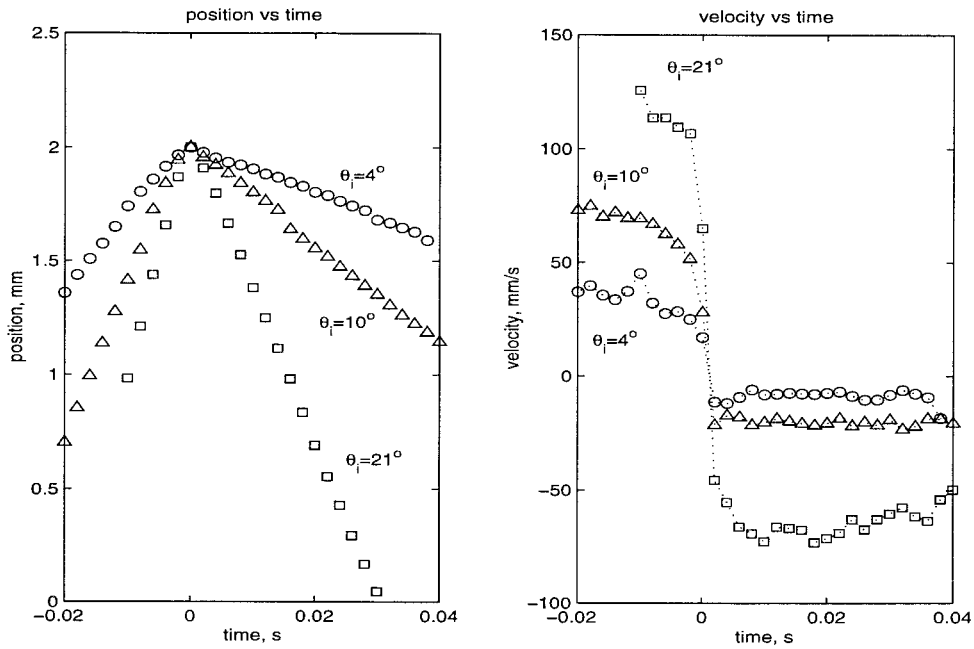

Figure 3.12: Particle position and velocity as a function of time for a 6 mm glass particle in water, for various initial release angles.

observed in most of the release angles tested. It should also be noted that in some cases the measured rebound shows a fair amount of variance. Under the same nominal experimental conditions, particles approaching at approximately equal velocities would result in rebound velocities of up to 30% difference. This behavior was observed for all of the particles tested. The reason for this variance is unclear. Care was taken to ensure that the surfaces were clean and that the water used was as pure as possible. The rebound may be influenced by the configuration of the surface roughnesses at the exact point of contact. Impurities in the liquid, perhaps introduced during the handling of the experiment, may have an effect on the nature of the contact and rebound as well. The fluid motion all around the sphere, in the moment of collision, may also affect the rebound.

Figure 3.13 presents the results for a 4 mm glass particle. For slowly moving particles the finite size pixel resolution causes the error involved in the measurement of the particle centroid displacement to increase. Noise in the velocity plots can be clearly observed, and the differences in the rebound velocities for the different cases

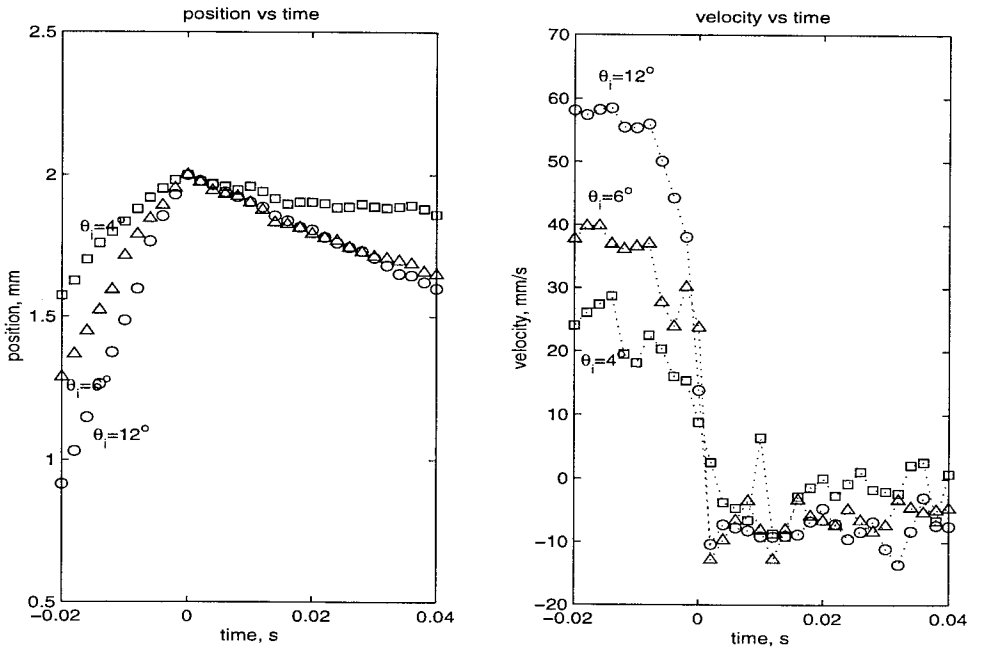

Figure 3.13: Particle position and velocity as a function of time for a 4 mm glass particle in water, for various initial release angles.

are hard to distinguish. The position-time plot allows a clearer view of the results. The lines with the smaller slope denote the slower approach velocities. Clearly, it can be observed that if the approach velocity is small, the rebound velocity will be small. In the case of the line representing the collision starting from a 4^o angle, the slope of the rebound trajectory is nearly zero. A zero slope in the rebound trajectory represents no rebound after contact.

Figure 3.14 shows the results obtained for a 3 mm glass particle. To reduce the error due to finite pixel resolution, the recording framing rate was reduced to allow longer displacements between consecutive frames. For this case and the case of the 6.35 mm nylon particles the video framing rate was 250 frames per second. The noise introduced in the particle velocity by the finite pixel size can be observed in the velocity-time plot.

Figure 3.15 show the measurements obtained for a 6.35 mm nylon sphere. For this case only the positions as a function of time are shown. For the case of slowly moving particles the error in the measurement of particle displacement increases due to the

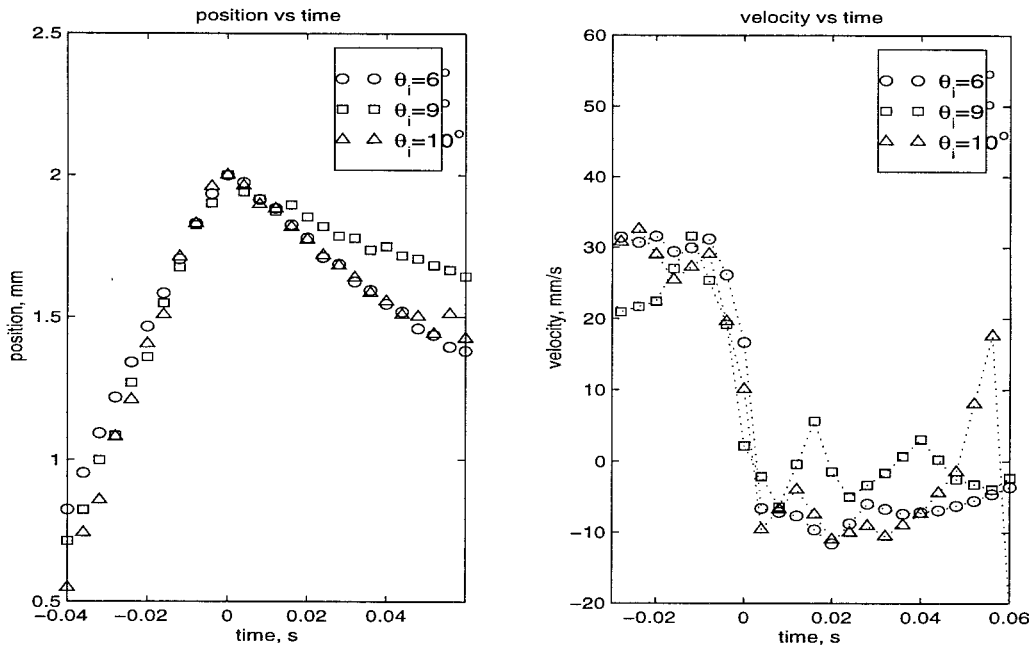

Figure 3.14: Particle position and velocity as a function of time for a 3 mm glass particle in water for various initial angles of release.

limitations in the pixel resolution. Since the velocity is calculated point-wise, small variations in the measured displacement can result in large variations in the velocity. The approaching velocities are in accordance with the initial angle of release; however, a wider range of velocities could not be obtained. The rebound velocities for the 10^o and 5^o are practically zero, in which no rebound was noticed.

Based on these observations different coefficients of restitution can be defined. A total coefficient of restitution, ϵ_{tot}, was calculated by measuring the approach and rebound velocities at distances 'far' from the wall, where the rapid changes of velocity due to the collision are not observed. To obtain a consistent measurement, the approach and rebound velocities were measured 10 ms before and after the point of collision (5 data points before and after collision for a 500 frames per second data set). The results obtained for the total coefficient of restitution are presented in figure 3.16, as a function of the impact velocity, for all the particles tested. A certain amount of variance in the measured coefficients can be observed; however, the general trend is clear. The coefficient of restitution appears to increase with impact velocity and

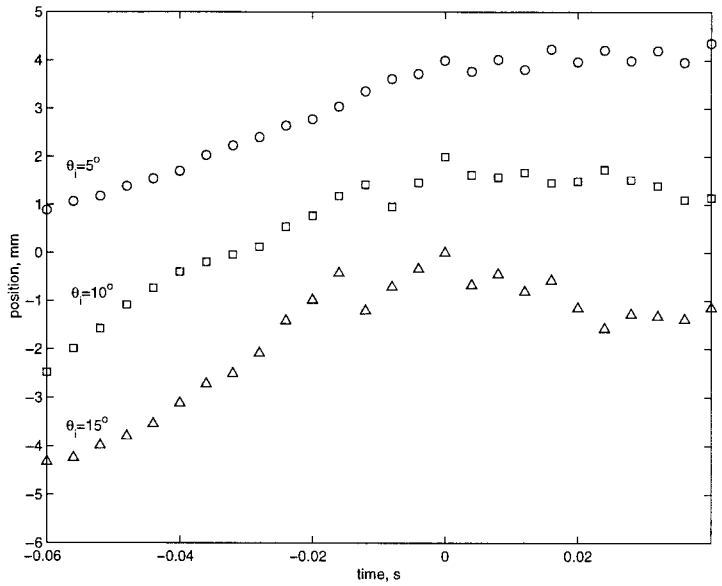

Figure 3.15: Particle position as a function of time for a 6.35 mm nylon particle in water for various initial angles of release.

particle Stokes number.

A contact coefficient of restitution could be calculated if the velocities just before and after the contact are measured. Due the limited time resolution of the experimental setup, these velocities can only be estimated. By fitting curves (second order polynomials) to the velocities 10 ms (5 data points) before and after contact, the impact and rebound velocities can be extrapolated. Figure 3.17 shows the calculated restitution coefficient as a function of impact velocity for all the particles tested. The resulting coefficient of restitution appears to be closer to 1, as it would be expected for a dry collision. However, the error caused by the finite pixel size introduces large errors to the calculation of the extrapolated velocities.

3.3.3 Collision impulses

Since the collision impulse, according with Hertzian predictions, is independent of the elastic properties of the colliding surfaces (see Chapter 2), it appears to be the most appropriate parameter to present the collision measurements.

Figure 3.18 shows the measured collision impulse as a function of the predicted

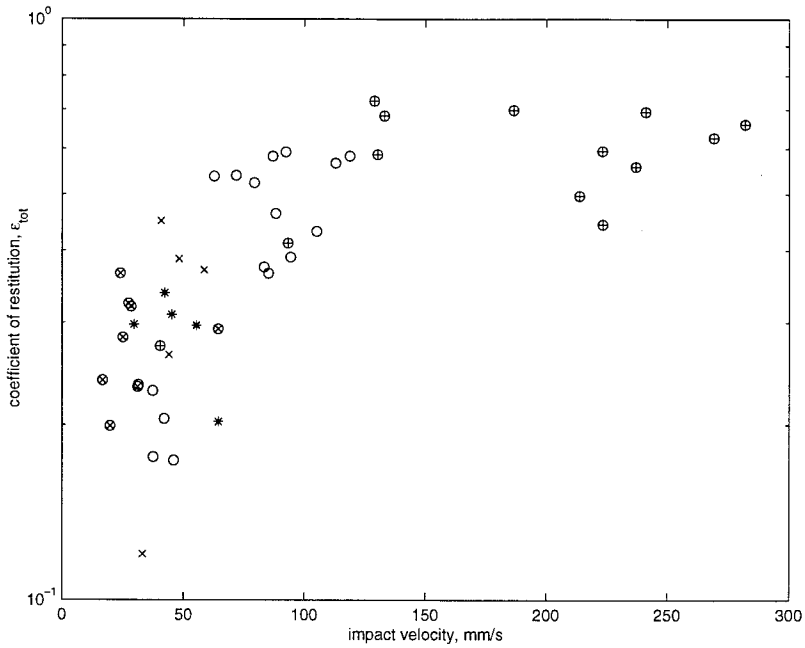

Figure 3.16: Plot of the total coefficient of restitution, ϵ_{tot} as a function of impact velocity, for all particles. See Table 3.1 for symbol identification.

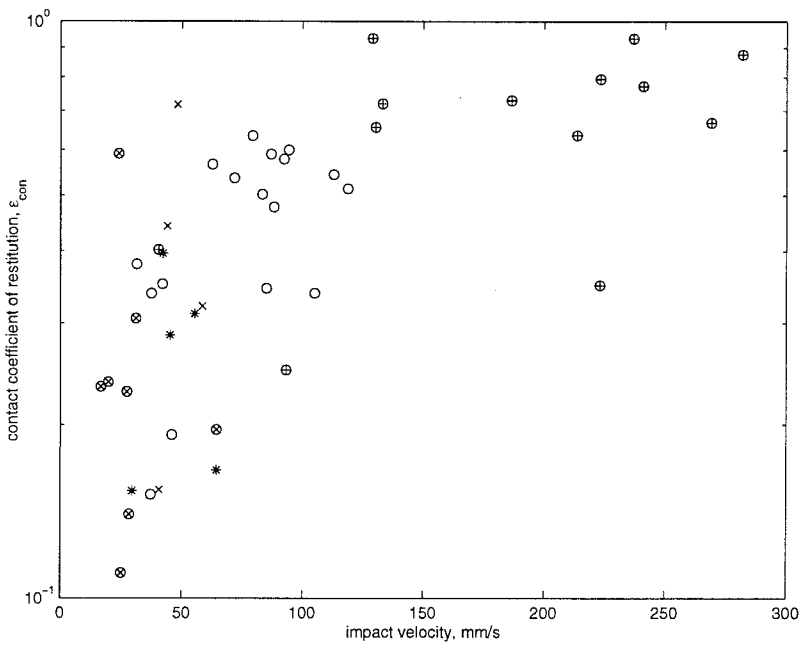

Figure 3.17: Plot of the contact coefficient of restitution, ϵ_{con} as a function of impact velocity, for all particles. See Table 3.1 for symbol identification.

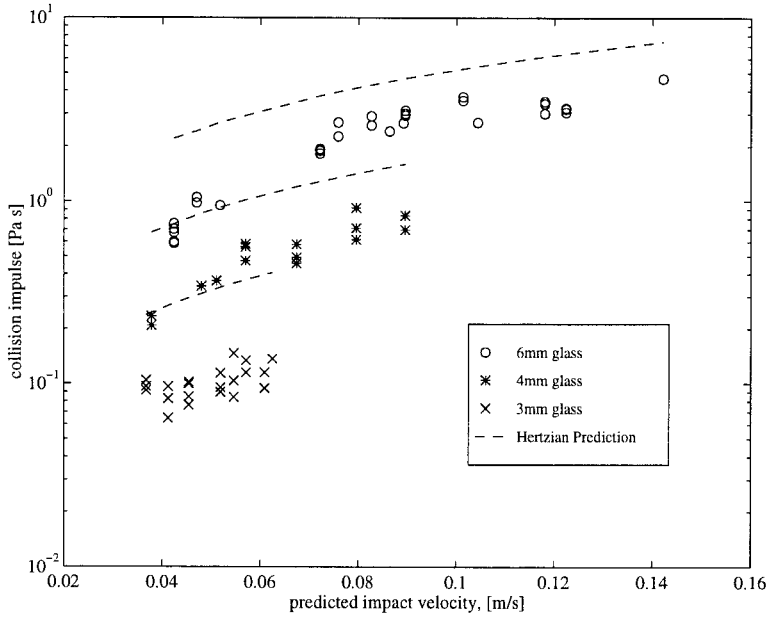

Figure 3.18: Measured collision impulse as a function of impact velocity. Glass particles in water. The dashed lines represent the Hertzian theory prediction.

impact velocity for three different glass particle diameters in water. The velocity of impact is calculated from the pendulum equation, and it does not account for the effect of the wall. To compare, the predictions from Hertzian theory are also shown. The experimental measurements appear to follow a trend similar to that predicted by the Hertzian theory, that is an increase in collision impulse with particle mass and velocity of impact. It can be argued that the difference between the ideal prediction and the measurements is the total effect of the interstitial fluid.

Similarly, figure 3.19 shows the measured collision impulse as a function of the predicted impulse velocity for 4.5 mm steel particles, 6.35 mm nylon particles and 4 mm glass particles. The corresponding dashed lines show the predictions of Hertzian theory. For all these cases the measured collision impulse appears to increase with particle mass and impact velocity. It can also be noted that the deviation from the Hertzian prediction increases for smaller impact velocities.

Following the scaling proposed by the Hertzian theory, the collision impulse results

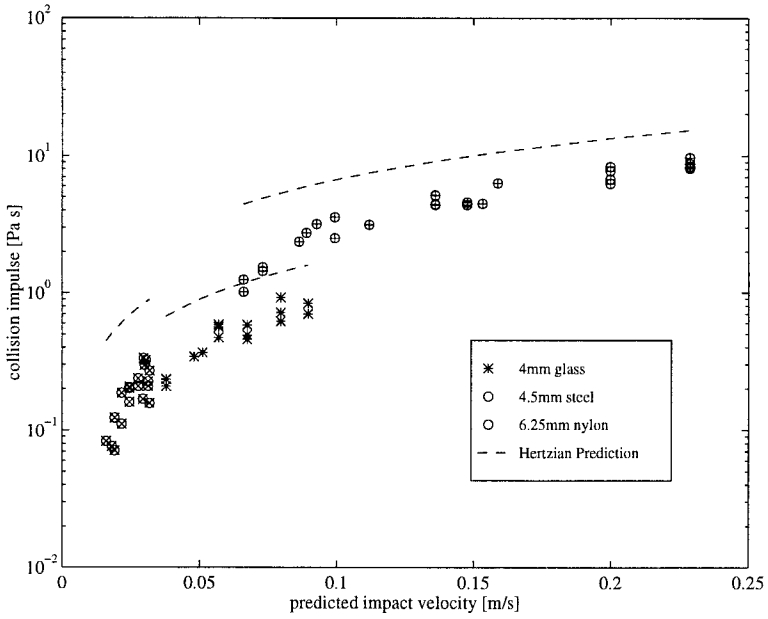

Figure 3.19: Measured collision impulse as a function of impact velocity. Steel, nylon and glass particles in water. The dashed lines represent the Hertzian theory prediction.

are non-dimensionalized using

$$\hat{I} = \frac{I}{u_i m_p} \tag{3.4}$$

where I is the measured collision impulse, u_i is the predicted impact velocity and m_p is the mass of the particle. Note that, when non-dimensionalized, the collision impulse predicted by the Hertzian theory is constant. The normalized results are shown in figure 3.20. The data appears to come closer together, forming a single band of values. For small impact velocities the scatter is larger, although a clear increase of the deviation from Hertzian theory can be observed.

3.4 Modeling

In order to predict the effect of the fluid as a spherical particle approaches a flat solid wall, a simple model based on a control volume is proposed. By calculating the mass and momentum fluxes of the fluid in the gap between the solid wall and the particle

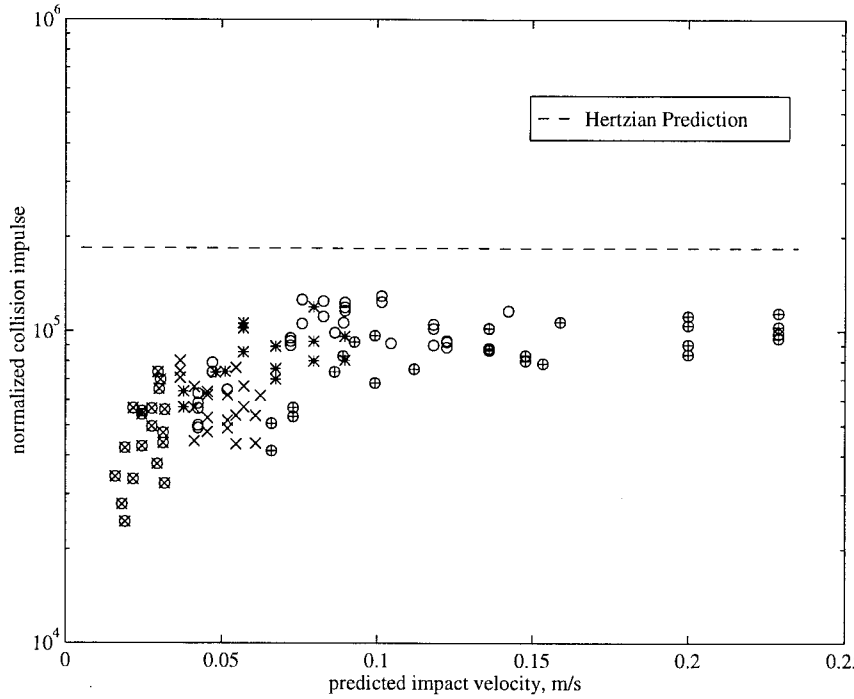

Figure 3.20: Normalized collision impulses as a function of predicted impact velocity.

an estimate of the pressure is calculated. By integrating the pressure over the surface of the particle the net force can be calculated. This net force is then incorporated into the equation of motion of the particle such that the velocity and deceleration of the particle can be calculated prior to collision.

Consider a spherical particle of radius a of mass m moving towards a flat wall, whose center is positioned at $h(t)$ at some instant t in time, immersed in a viscous and incompressible fluid of density ρ_f and viscosity μ. The velocity and acceleration of the sphere moving towards a solid boundary are therefore $\dot{h}$ and $\ddot{h}$ respectively, (see figure 3.21).

The motion of the particle in the z-direction will impose a radial velocity u_r to the fluid in the gap. For contact to take place, the fluid in between the particle and the wall has to be displaced. Therefore, some of the kinetic energy of the particle will be transferred to the fluid, and some will be dissipated in viscous friction. A control volume analysis can be performed in the gap. The control volume (figure 3.22) is a

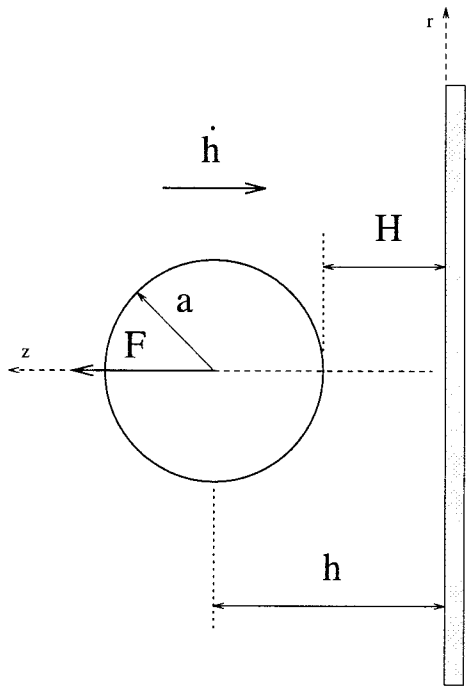

Figure 3.21: Schematic of the problem and coordinate system.

cylindrical shell of infinitesimal thickness dr (shaded area). Assuming that the flow in the gap is axisymmetric ($\frac{\partial}{\partial\theta}$=0) and purely radial ($\vec{u} = (u_r, 0, 0)$), and that the pressure field is uniform with respect to the z direction, the mass and momentum balances for the control volume can be obtained.

The mass conservation analysis leads to

$$u_r h = -\frac{r}{2}\dot{h} \tag{3.5}$$

where u_r is the mean radial velocity of the fluid in the gap, $h(r)$ is particle profile and $\dot{h}$ is the velocity at which the particle is moving. The equation obtained from the momentum balance is

$$r\frac{\partial}{\partial t}(u_r h) + \frac{\partial}{\partial r}(u_r^2 hr) = -\frac{1}{\rho_f}\frac{\partial}{\partial r}(Phr) - \frac{2r}{\rho_f}\tau_w \tag{3.6}$$

where $P(r)$ is the pressure in the fluid in the gap and τ_w is the wall shear stress.

Combining equations 3.5 and 3.6 and integrating over r, an explicit expression for

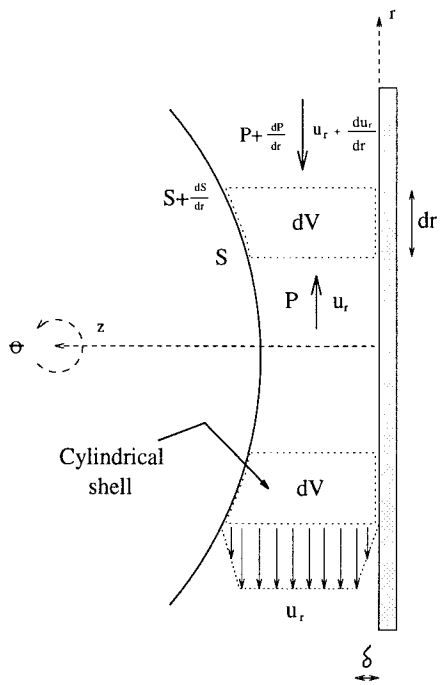

Figure 3.22: Control volume : Momentum and mass fluxes.

the pressure $P(r)$ in the gap is obtained

$$P(r) = \frac{\rho_f}{6}\frac{r^2\ddot{h}}{h} - \frac{\rho_f}{4}\left(\frac{r\dot{h}}{h}\right)^2 - \frac{2}{hr}\int_0^r r'\tau_w dr' \tag{3.7}$$

To account for the effects of the wall viscous shear stress, a simple model is used. Assuming that the effects of viscosity remain in a thin layer of fluid near the surfaces, it can be considered

$$\tau_w = \mu\frac{du}{dz}|_w \approx \mu\frac{u_r}{\delta} \tag{3.8}$$

where δ represents the thickness of the viscous fluid layer.

To obtain the total force exerted by the fluid on the particle, equation 3.7 is integrated over the projected area of the particle, assuming that the pressure outside the gap is a constant P_o (zero for convenience). Therefore,

$$\begin{aligned} F(t) &= \int_A P(r)dA = 2\pi\int_0^a P(r)rdr \\ &= 2\pi\frac{\rho_f\ddot{h}}{6}\int_0^a \frac{r'^3}{h}dr' - 2\pi\frac{\rho_f\dot{h}^2}{4}\int_0^a \frac{r'^3}{h^2}dr' \end{aligned}$$

$$-2\pi\frac{\mu\dot{h}}{\delta}\int_0^a\frac{1}{h}\left[\int_0^{r'}\frac{r''^2}{h}dr''\right]dr' \tag{3.9}$$

To obtain an explicit expression for the force, it remains only to obtain an expression for the particle profile, $h(r)$. For a spherical particle the exact profile is

$$h(r) = H + a - \sqrt{a^2 - r^2} \tag{3.10}$$

To make the integrals simpler, an approximation for the profile is used instead

$$h(r) = H + \frac{r^2}{a} + ... \tag{3.11}$$

This makes the handling of the obtained expressions tractable, yet preserves the geometric characteristics of the curved surface.

For convenience the expressions are made non-dimensional using $\hat{r} = \frac{r}{a}, \hat{h} = \frac{h}{a}, \hat{t} = \frac{t}{t_c}$. Here t_c is a characteristic time, not yet specified. Using these and integrating using the simplified profile (equation 3.11), the expression obtained for the non-dimensional force is

$$\hat{F}(\hat{t}) = A(\hat{H})\ddot{\hat{h}} - B(\hat{H})\dot{\hat{h}}^2 - C(\hat{H})\frac{\mu_f t_c}{\rho_f a^2}\frac{a}{\delta}\dot{\hat{h}} \tag{3.12}$$

where $\hat{F}(\hat{t})$ is normalized by $\rho_f\left(\frac{a}{t_c}\right)^2 a^2$ and $A(\hat{H})$, $B(\hat{H})$ and $C(\hat{H})$ are functions of $\hat{H}$ defined as

$$\begin{aligned}
A(\hat{H}) &= \frac{\pi}{6}\left(1 - \hat{H}Log\left(\frac{1+\hat{H}}{\hat{H}}\right)\right) \\
B(\hat{H}) &= \frac{\pi}{4}\left(\frac{\hat{H}}{1+\hat{H}} - 1 + Log\left(\frac{1+\hat{H}}{\hat{H}}\right)\right) \\
C(\hat{H}) &= \pi\left(Log\left(\frac{1+\hat{H}}{\hat{H}}\right) - Tan^{-1}\left(\frac{1}{\sqrt{\hat{H}}}\right)^2\right)
\end{aligned}$$

Particle equation of motion

Once an expression for the force on the particle has been obtained, it can be incorporated in the equation of motion of the particle and solved to obtain the deceleration

of the particle prior to collision,

$$-\hat{F} = \Gamma \ddot{\hat{h}} \tag{3.13}$$

where Γ is the normalized mass of the particle defined as

$$\Gamma = m/(\frac{4\pi}{3}a^3\rho_f) = \frac{\rho_p}{\rho_f} \tag{3.14}$$

Grouping terms

$$\ddot{\hat{h}}\left(\Gamma + A(\hat{H})\right) = B(\hat{H})\dot{\hat{h}}^2 + C(\hat{H})K\dot{\hat{h}} \tag{3.15}$$

where

$$K = \frac{\mu t_c}{\rho_f a^2}\frac{a}{\delta}.$$

Equation 3.15 is a second order non-linear ODE, which can be solved numerically. The characteristic time t_c can be now specified as $t_c = a/\dot{h}_0$. The set of initial conditions is

$$\begin{aligned} \dot{\hat{h}}(0) &= 1 \\ \hat{H}(0) &= 2. \end{aligned}$$

In this case the particle has a velocity $\dot{h}_0$ at a distance $2a$ (a diameter) away from the wall. The coefficient K in equation 3.15 becomes

$$K = \frac{2\mu_f}{\rho_f 2a h_0}\frac{a}{\delta} = \frac{2}{Re_0}\frac{a}{\delta} \tag{3.16}$$

where Re_o is the initial Reynolds number.

3.4.1 Results of the model

Figures 3.23 and 3.24 show some of the results obtained from this model. The vertical axis shows the nondimensional approach velocity ($\dot{h}/\dot{h}_0$) and the horizontal axis shows the dimensionless distance from the wall, $\hat{H}$. Figure 3.23 shows the phase plots

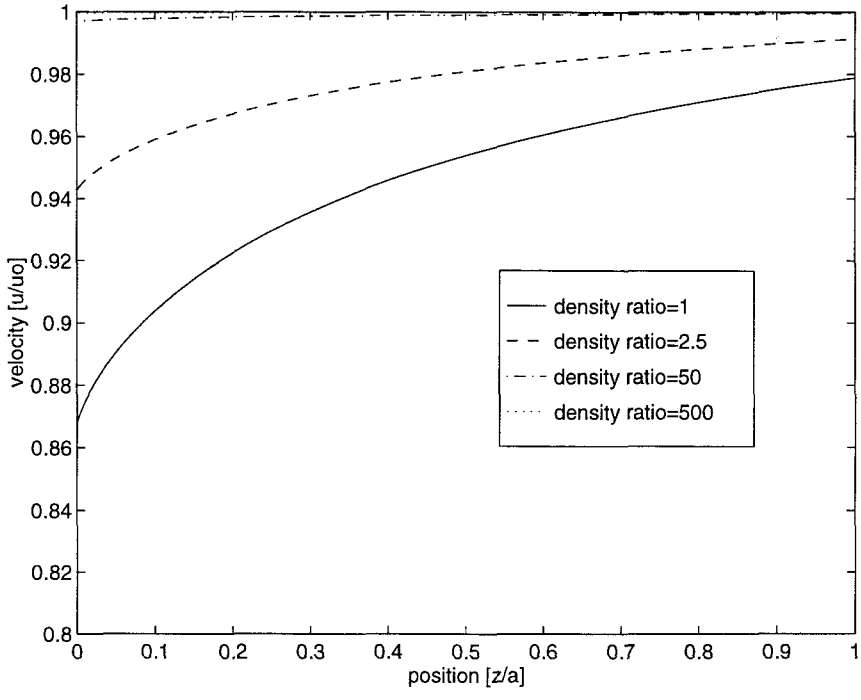

Figure 3.23: Phase plot of non-dimensional velocity vs. non-dimensional distance, inviscid case.

obtained for an inviscid case. Each line represents a different density ratio. The particle impact velocity, e.g., the velocity at $\hat{H} = 0$, is larger for a larger density ratio.

Figure 3.24 shows the phase plots obtained for different Reynolds number for a fixed density ratio ($\Gamma = 2.5$). The value of the parameter K was calculated assuming that

$$\frac{\delta}{a} \propto \frac{1}{\sqrt{Re_o}} \tag{3.17}$$

therefore,

$$K = \frac{C_o}{\sqrt{Re_o}} \tag{3.18}$$

where C_o is a constant ($C_o = 0.04$ was chosen for these calculations, which corresponds to a thickness, δ/a, of approximately 1/80). The figure shows that for decreasing Reynolds number the deceleration of the particle is higher. Moreover, a critical Reynolds number can be found for each density ratio at which the particle reaches the wall with zero velocity. Below that critical number the particle stops

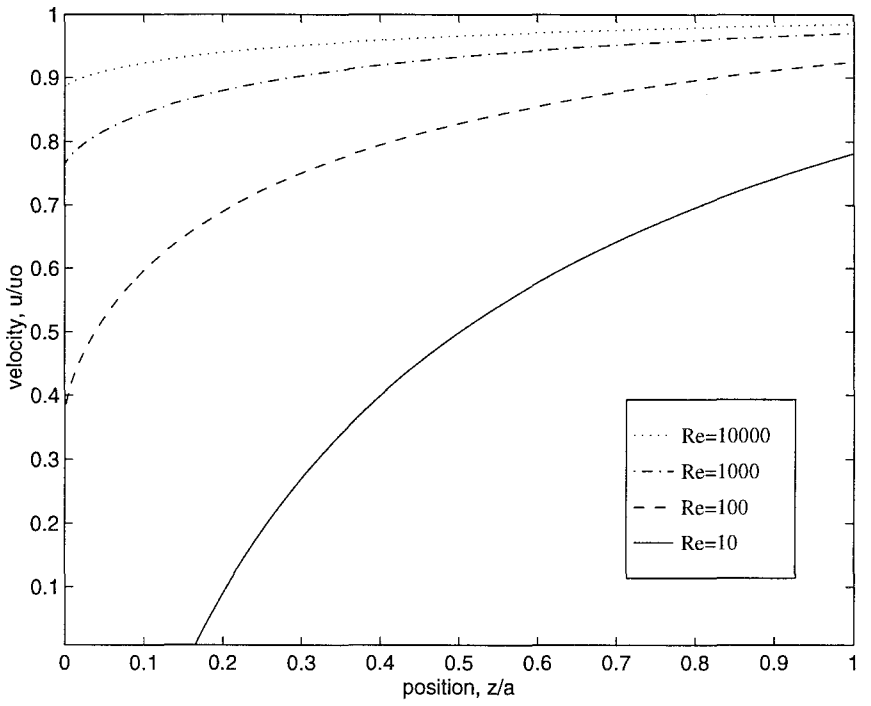

Figure 3.24: Phase plot of non-dimensional velocity vs. non-dimensional distance, viscous case for a density ratio of 2.5 ($C_o = 0.04$).

completely before reaching the wall. The existence of this critical value of Reynolds is in agreement with experiments performed by McLaughlin (1968).

Figures 3.25 and 3.26 show plots of the calculated critical Reynolds number, Re_c. The critical Reynolds number is defined as the Reynolds number at which the particle reaches the wall with zero velocity, and for $Re_o < Re_c$ the particle stops completely before reaching the wall. Figure 3.25 shows the critical Reynolds number as a function of the density ratio, Γ. It can be observed that as the density ratio decreases, the critical Reynolds number decreases. This means that as the particles become lighter the viscous forces become more dominant and therefore the stoppage Reynolds number can occur at a larger value. Figure 3.26 shows the calculated critical Reynolds number as a function of the particle Stokes number. The Stokes number is defined as

$$St_p = \frac{m_p u_p}{6\pi\mu a^2} = \frac{1}{9}\frac{d_p \rho_p u_p}{\mu} = \frac{1}{9}\Gamma Re_p$$

A solution for equation (3.15) can also be obtained analytically. Using the trans-

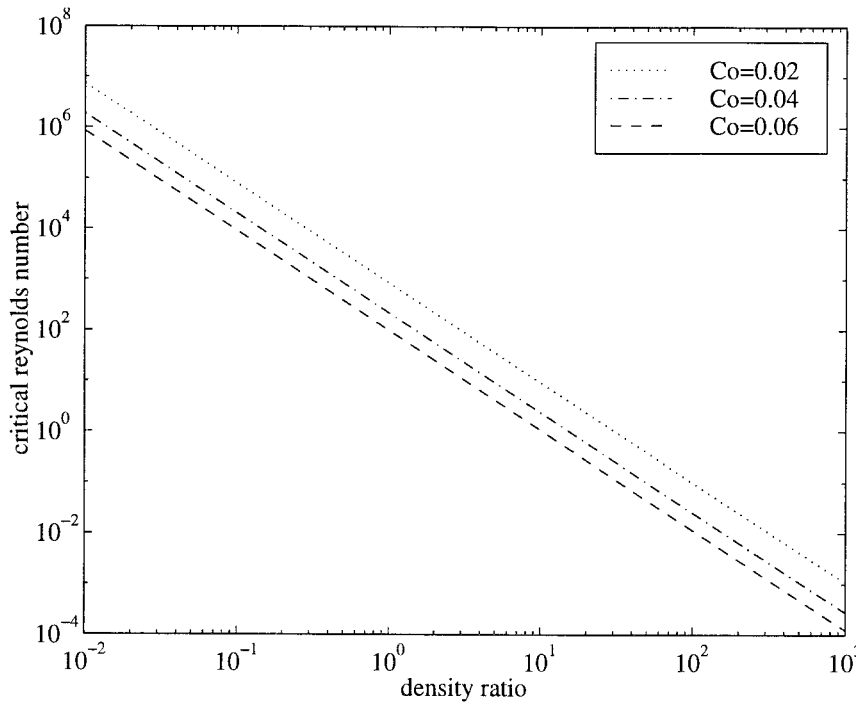

Figure 3.25: Critical Reynolds number Re_c as a function of the density ratio, ρ_p/ρ_f, for different values of the proportionality constant C_o.

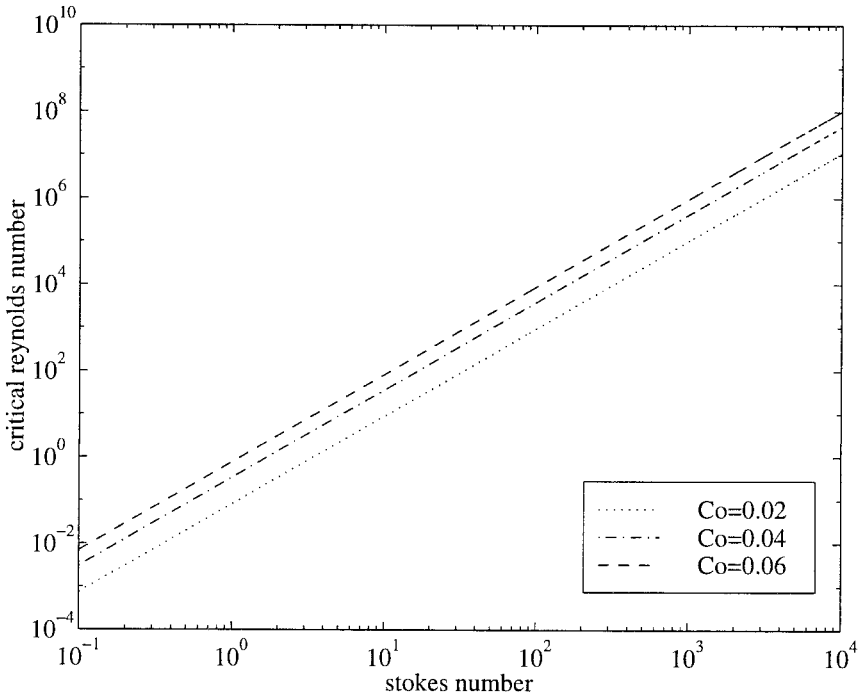

Figure 3.26: Critical Reynolds number Re_c as a function of the Stokes number, St_p, for different values of the proportionality constant C_o.

formation $\hat{\dot{h}} = V$ equation (3.15) can be re-written as,

$$\frac{\partial V}{\partial \hat{H}} = B'(\hat{H})V + C'(\hat{H}) \tag{3.19}$$

where $B'(\hat{H}) = B(\hat{H})/(\Gamma + A(\hat{H}))$ and $C'(\hat{H}) = C(\hat{H})/(\Gamma + A(\hat{H}))$. The solution for this first order linear equation is

$$V = \frac{C_1}{I(\hat{H})} + \frac{1}{I(\hat{H})}\int^{\hat{H}} C'(\hat{H}')I(\hat{H}')d\hat{H}' \tag{3.20}$$

where C_1 is a constant that depends on the initial condition and $I(\hat{H})$ is the integrating factor,

$$I(\hat{H}) = \left(-6\,\Gamma - \pi + \pi\,\hat{H}\,\log(1 + \frac{1}{\hat{H}})\right)^{-\frac{3}{2}}. \tag{3.21}$$

Equation 3.20 can be shown to be finite as $\hat{H} \to 0$. Therefore, the model can predict a non-zero finite impact velocity. The models found in the literature assumed that the flow in the gap was in the creeping regime for $\hat{H} \ll 1$, which resulted in the complete stoppage of the particle before actual contact occurred.

3.4.2 Comparisons with experiments

In an attempt to validate the predictions from the model, a comparison with the experimental measurements is presented. The experimental measurements presented in figures 3.18 and 3.19 are plotted using the predicted velocity from the pendulum equation, which does not account for the presence of the wall. This predicted velocity can be corrected using the model presented above. The velocity a diameter away predicted from the pendulum equation can be input as the initial condition, and therefore an approximation for the actual impact velocity can be obtained. Once the corrected value of the impact velocity is known, a new estimate of the collision pressure can be calculated using the Hertzian theory.

Figures 3.27 and 3.28 show the measured collision impulse as a function of the predicted impact velocity. Figure 3.27 shows the results for 6 mm glass, and figure

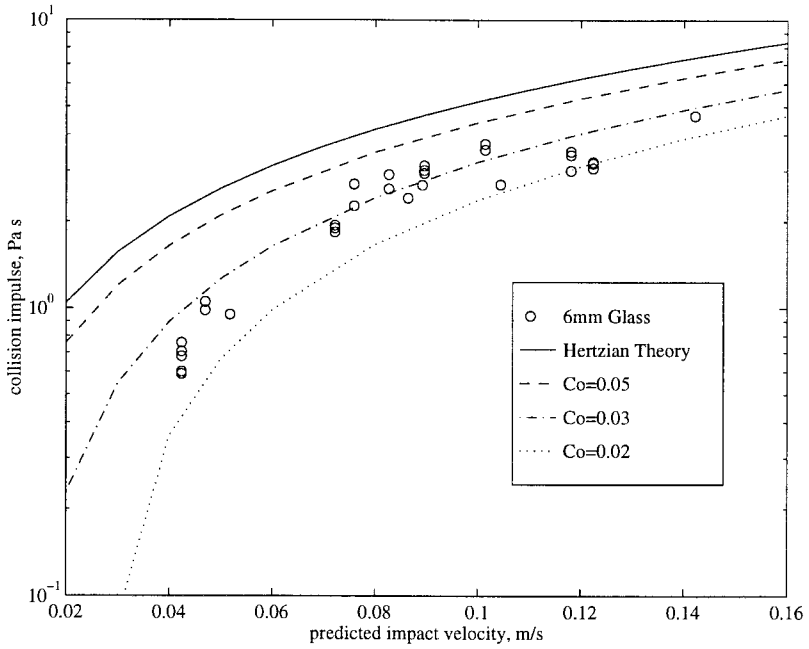

Figure 3.27: Collisional Impulse as a function of predicted impact velocity. Comparison between the 6 mm glass particle experimental measurements and the predictions from the model for different values of the proportionality constant C_o.

3.28, the results for 4.5 mm steel particles. The solid line shows the prediction from Hertzian theory with the uncorrected impact velocity. The different dashed lines show the predicted impulse when the impact velocity is corrected using the model, for different values of the proportionality constant C_o. It can be observed that when the impact velocity is corrected with the model, the predicted collision impulse appears closer to the experimental measurements. It appears also that the proportionality constant C_o may be itself function of the density ratio.

3.5 Binary collisions

With a slight modification, the experimental setup allowed the measurements of binary collisions of particles. An additional particle (the target particle) was suspended in a pendulum-like fashion at rest. The two pendulum strings were aligned to ensure a normal head-on collision between the two particles. By releasing the original

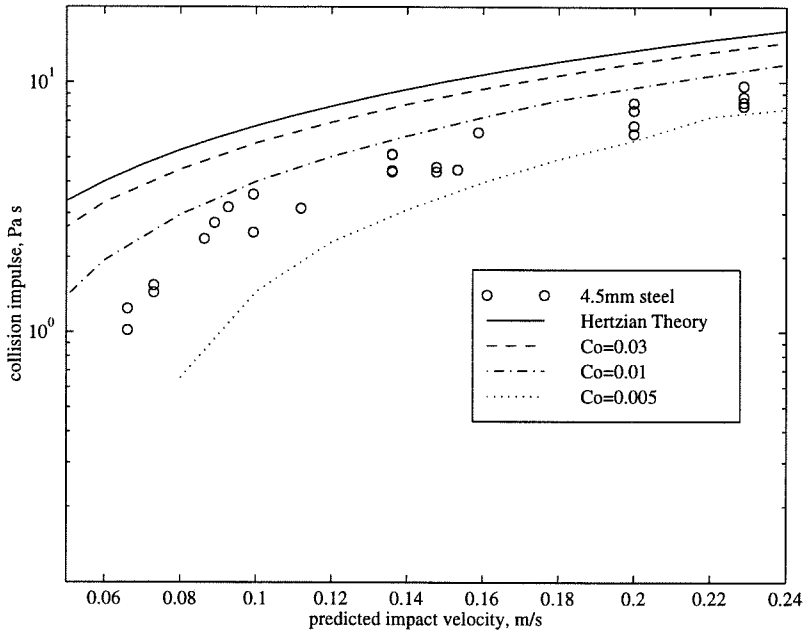

Figure 3.28: Collisional Impulse as a function of predicted impact velocity. Comparison between the 4.5 steel particle experimental measurements and the predictions from the model for different values of the proportionality constant C_o.

particle (impact particle) from rest, the two particles come into contact. A more detailed description can be found in chapter 4. A very similar setup is used to study the fluid pressure produced and radiated during a binary collision of particles. The collision results in the acceleration of the target particle and the deceleration of the impact particle. By tracking the positions of the two particles a measurement of their velocity could be obtained, as well as the coefficient of restitution.

Figures 3.29 and 3.30 show a typical binary collision of two 6 mm glass particles. The incoming impact velocity was approximately 90 mm/s. It can be noted that the target particle begins to move slowly moments before contact occurs, presumably due to the pressure disturbance created by the motion of the impact particle. When contact occurs the velocities of both particles change abruptly. The target particle increases its velocity significantly, while the impact particle velocity decreases. As time progresses, the velocity of the target particle decreases slightly, while the velocity of the target particle appears to increase. This effect can be interpreted as an attraction between the target and impact particles. The low pressure wake behind

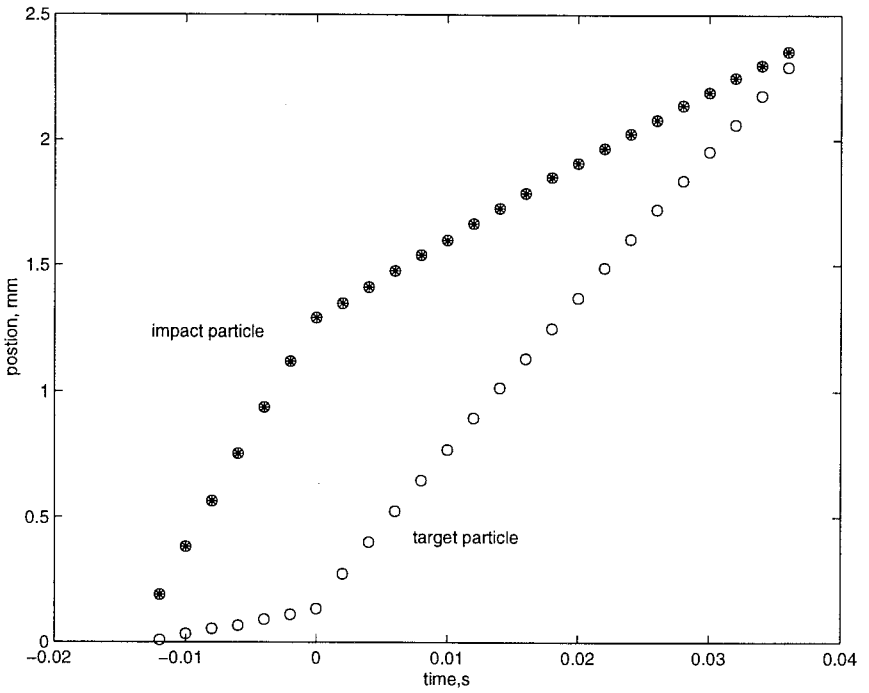

Figure 3.29: Typical time history of the position of two 6 mm glass particles undergoing a binary collision immersed in water.

the moving target particle appears to exert a positive force on the impact particle, making it increase its velocity.

The coefficient of restitution can be calculated using

$$\epsilon_{bin} = \frac{(u_{tar} - u_{imp})_\tau}{(u_{tar} - u_{imp})_a} \tag{3.22}$$

where u_{tar} is the velocity of the target particle, u_{imp} is the velocity of the impact particle, the subscript τ denotes the velocities after collision and the subscript a the velocities before collision. It is important to establish the point at which the velocities will be measured. The coefficients reported in this section are calculated from the velocities immediately before and after the large velocity jump produced by the collision.

Figures 3.31 to 3.34 show typical cases of binary collisions for different particle densities and collision velocities. It can be observed that, in general, the coefficient of restitution decreases with the impact velocity and the particle Reynolds number.

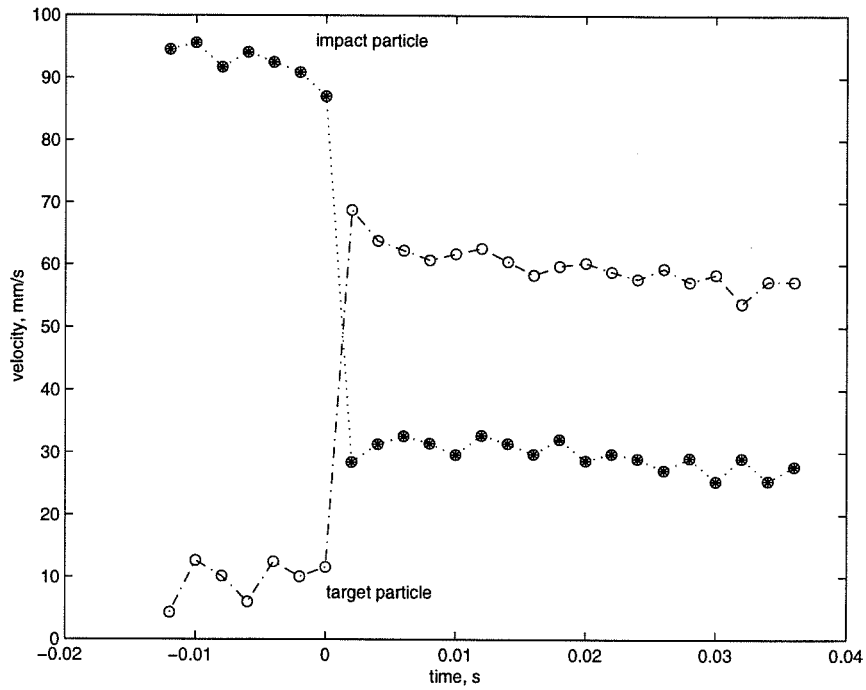

Figure 3.30: Typical time history of the velocity of two 6 mm glass particles undergoing a binary collision immersed in water. $\epsilon_{bin} = 0.52$, $(u_i)_o = 88mm/s$.

Since only a few typical cases were studied, the calculated coefficients of restitution are shown in the captions of the respective figures.

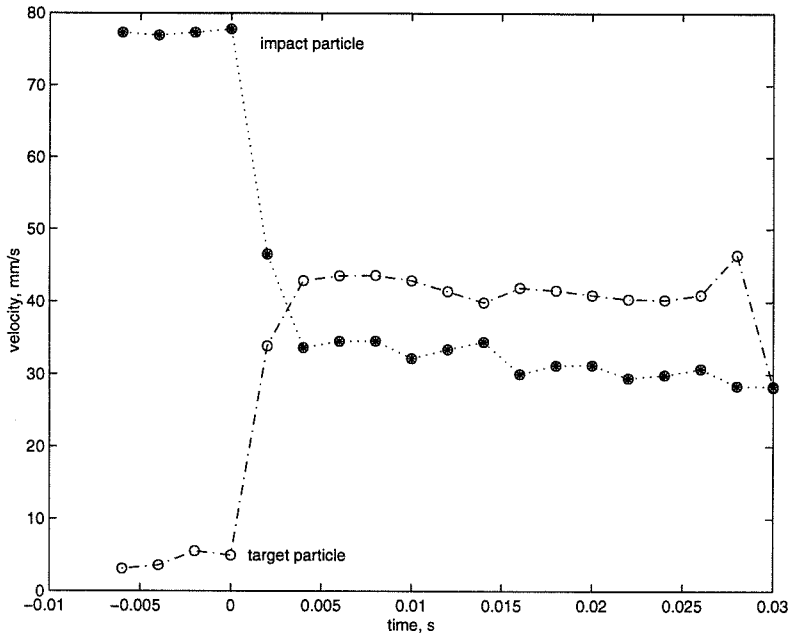

Figure 3.31: Typical time history of the velocity of two 4 mm glass particles undergoing a binary collision immersed in water. $\epsilon_{bin} = 0.10$, $(u_{imp})_a = 78mm/s$.

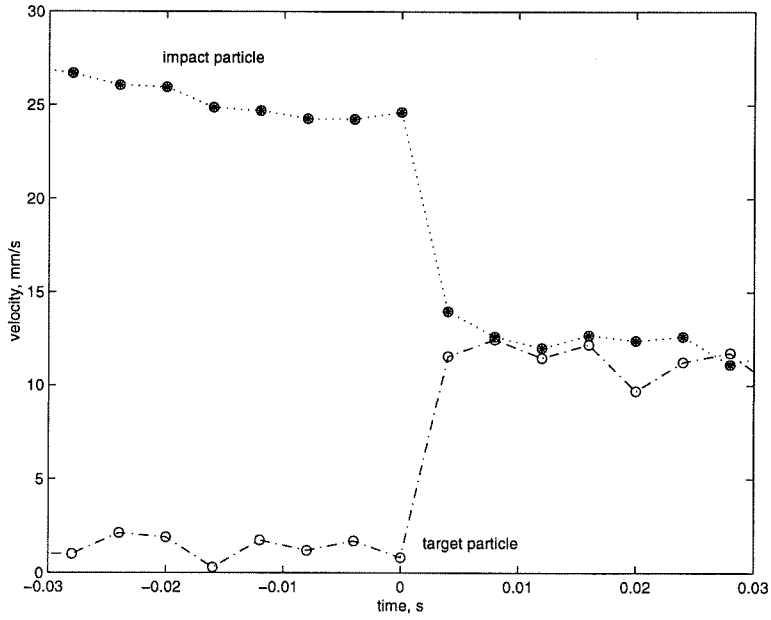

Figure 3.32: Typical time history of the velocity of two 3 mm glass particles undergoing a binary collision immersed in water. $\epsilon_{bin} = 0.01$, $(u_{imp})_a = 25mm/s$.

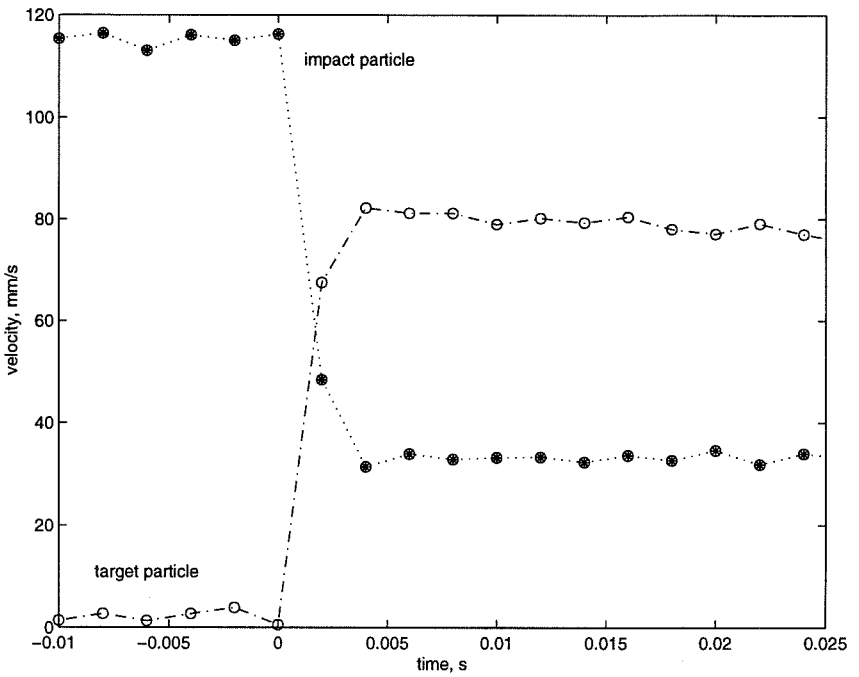

Figure 3.33: Typical time history of the velocity of two 4.5 mm steel particles undergoing a binary collision immersed in water. $\epsilon_{bin} = 0.43$, $(u_{imp})_a = 116mm/s$.

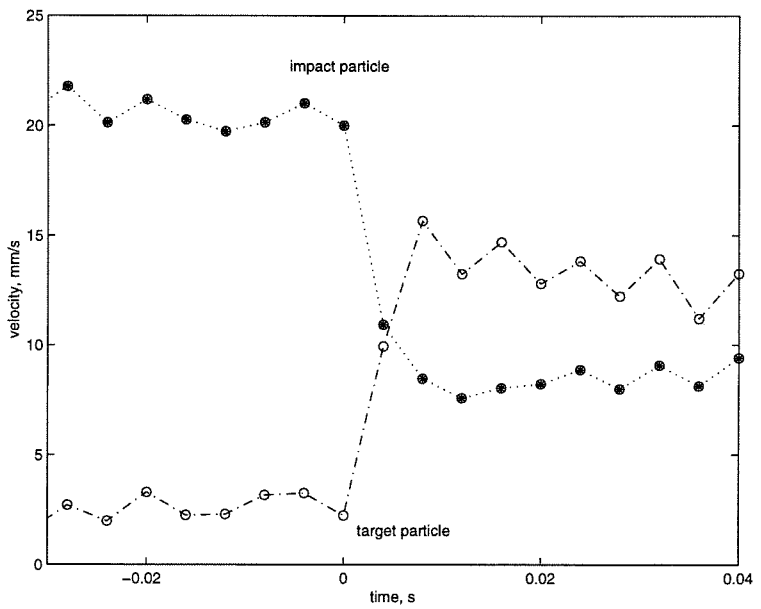

Figure 3.34: Typical time history of the velocity of two 6.35 mm nylon particles undergoing a binary collision immersed in water. $\epsilon_{bin} = 0.37$, , $(u_{imp})_a = 20mm/s$.

Chapter 4 Liquid pressure front generated by particle-particle collisions

4.1 Introduction

In Chapter 2 the results of the collisional particle pressure measurements for solid-liquid flows were presented. The particle pressure was defined as the additional pressure exerted on the containing walls of a particulate system due to the presence of the particles. The collisional particle pressure measured on a surface was found to be composed of two contributions: direct collisions of particles against the surface, and a pressure contribution from particle-to-particle collision that was transmitted through the fluid.

Originally the particle pressure was thought of being solely the result of direct collisions between particles and containing walls. However, during the analysis of the probability density functions (see section 2.6), two different kinds of pressure pulses were identified. One corresponded with the estimated values of a collision of an individual particle from Hertzian theory of contact. The origin of the short duration pulses was not resolved until a detailed visualization of the particles was performed.

The first contribution, the direct collision of particles, was studied in detail in Chapter 3. The mechanics of the approach, contact and rebound were presented.

In this chapter a study of the second contribution of the collisional particle pressure is presented. It was discovered that when a collision of two particles occurs in the vicinity of the transducer, a pressure front is generated due to the impact and is transmitted through the fluid. In this case the particles are not in direct contact with the transducer at the moment when the pressure pulse is registered. The intensity of these pulses is related to the impact velocity of the collision, the orientation of the colliding particles with respect to the transducer and the distance from the collision

to the transducer. The duration of these events is determined by the fact that two particles are colliding rather than a single particle with a flat surface. The pressure front is generated due the impulsive acceleration imposed on a particle due to a collision event. As described in Chapter 3, the velocity of a particle changes significantly in a short time period when a collision has occurred.

The nature of these radiated pressure pulses is described in the next section, and is characterized and corroborated experimentally in the subsequent sections.

4.1.1 Pressure-impulse theory

To determine the nature of the pressure front, a pressure-impulse analysis was explored. This approach is similar to that used by coastal engineers to determine the strength of wave impacts (Cooker & Peregrine, 1995), and involves the initiation of fluid motion in incompressible fluids.

The concept of impulse pressure, or impulsive pressure, is well known (Lamb, 1945; Batchelor, 1967), although it rarely appears in the multi-phase flow literature. Its development has been primely motivated by the study of water wave impacts against coastal structures. Coastal engineers refer to 'shock pressure' when describing the large brief pressures of a wave impact.

When a solid boundary suddenly accelerates, a change in the pressure field in the surrounding fluid is expected. If the change of velocity is the result of an impact, the pressure rises and falls back down in a very short period of time generating large pressure gradients causing the velocity of the fluid to change.

Since the change of velocity during this impulsive event takes place during a short period of time, the non-linear convective terms in the equation of motion are negligible small compared with the time derivative. Thus, the equations of motion reduce to

$$\frac{\partial \vec{u}}{\partial t} = -\frac{1}{\rho_f}\nabla P \tag{4.1}$$

assuming that the viscous effects are negligible. Compressibility effects may be important during the brief moment of impact, but are neglected for simplicity. Equation

4.1 can be time-integrated through the impact time interval, $[0, \tau]$, to obtain

$$\vec{u}_\tau - \vec{u}_0 = -\frac{1}{\rho_f}\nabla I \tag{4.2}$$

where I is the impulse pressure defined as[1]

$$I = \int_0^\tau P(t)dt \tag{4.3}$$

By taking the divergence of 4.2 it is obtained that the impulse pressure satisfies Laplace's equation

$$\nabla^2 I = 0 \tag{4.4}$$

The boundary conditions to be applied to equation 4.4 can be formulated readily

1. At a free surface the pressure remains constant, zero for convenience, : $I = 0$.
2. At a stationary solid boundary, in contact with the fluid, the normal velocity is unchanged: $\partial I/\partial n = 0$.
3. During impact the change in normal velocity at a moving fluid-solid interface gives:

$$\frac{1}{\rho_f}\frac{\partial I}{\partial n} = u_{nb}$$

.

Consider the domain shown in figure 4.1. A spherical particle, of diameter d, is positioned at a certain distance, b, away from a solid wall. The fluid is incompressible and is at rest for $t \leq 0$. If at $t = 0$ the particle is accelerated instantaneously from rest to a velocity u_τ, the impulse pressure problem, e.g., $\nabla^2 I = 0$, can be solved and the impulse pressure field calculated. Consider the following boundary conditions:

- at the wall, $\partial I/\partial x = 0$,
- far away from the wall, $I = 0$ ($\partial I/\partial x = 0$, could also be considered),

[1]similarly defined in equation 2.10

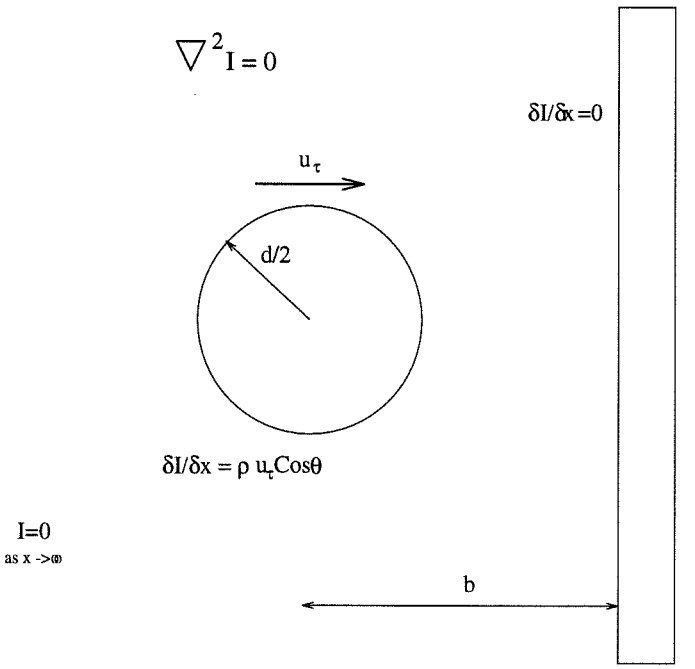

Figure 4.1: Schematic of the impulsive motion of a sphere near a wall in an inviscid irrotational flow.

- on the surface of the particle, $\partial I/\partial x = \rho_f u_\tau \cos\theta$.

Thus the impulse generated by the impulsive motion of a body is very similar to the velocity potential for the steady potential flow around that same body (Milne-Thompson, 1950). For example the impulse, I, produced by a sphere of diameter d, given a sudden change u_τ in its velocity in the x -direction (in an unbounded fluid), will be given by a doublet so that

$$I = \frac{1}{2}\rho_f u_\tau (d/2)^3 \frac{x+b}{((x+b)^2+y^2)^{3/2}} \tag{4.5}$$

where the center of the sphere is at $x = -b, y = 0$.

To obtain an approximate solution when there is a solid wall at $x = 0$ (as sketched in figure 4.1), an image doublet is placed at $x = +b, y = 0$ in order to satisfy the condition of zero velocity normal to the wall. Then

$$I = \frac{1}{2}\rho_f u_\tau (d/2)^3 \left(\frac{x+b}{((x+b)^2+y^2)^{3/2}} - \frac{x-b}{((x-b)^2+y^2)^{3/2}} \right) \tag{4.6}$$

The impulse pressure distribution is shown in figure 4.2 for different b/d ratios. In this figure the solid lines represent lines of constant impulse. The point $x/d = 0$ represents the position of the wall. It is important to note that the solution by mirror images is not an exact solution for the flow of a particle approaching a wall. The image doublet method does not precisely satisfy the boundary condition on the surface of the sphere, specially when the two spheres are close to one another.

The magnitude of the impulse pressure depends also on the angle of the impulsive motion with respect to the wall. Using ϕ as the angle between the impulsive motion direction and the vector normal to the wall ($\phi = 0$ when the motion is perpendicular to the wall, and $\phi = \pi/2$ when the motion is upwards parallel to the wall) equation 4.6 becomes

$$I = \frac{1}{2}\rho_f u_\tau (d/2)^3 \left(\frac{(x+b)\cos\phi - y\sin\phi}{((x+b)^2+y^2)^{3/2}} - \frac{(x-b)\cos\phi - y\sin\phi}{((x-b)^2+y^2)^{3/2}} \right) \tag{4.7}$$

The impulse pressure distribution for different incidence angles, ϕ, is shown in figure 4.3 for $b/d = 1.5$.

The exact solution of this problem can be obtained using a technique similar to one used by Landweber and Shahshahan (1992), when two spheres approach each other in an inviscid flow. By adding an infinite series of image doublets, the boundary condition on the surface of the spheres can be satisfied exactly for any b/d. However, this procedure requires large summations when the two particles are very close to each other. The construction above should represent the essence of the mechanics of the radiated pulse caused by a suddenly accelerated particle near a boundary.

4.2 Experimental setup

As described in the previous section, when the two particles come into contact, the impulsive acceleration imposed on the particles produces an impulsive pressure pulse. As observed in the experimental measurements, the pressure pulse is transmitted through the fluid from moving particles to the pressure transducer. To characterize

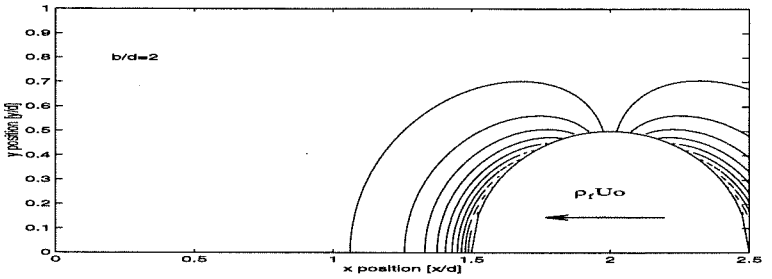

(a) $b/d = 2$

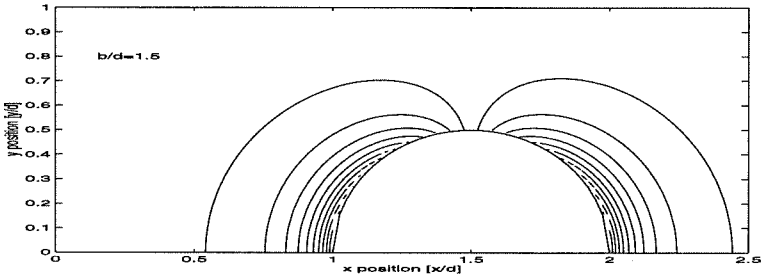

(b) $b/d = 1.5$

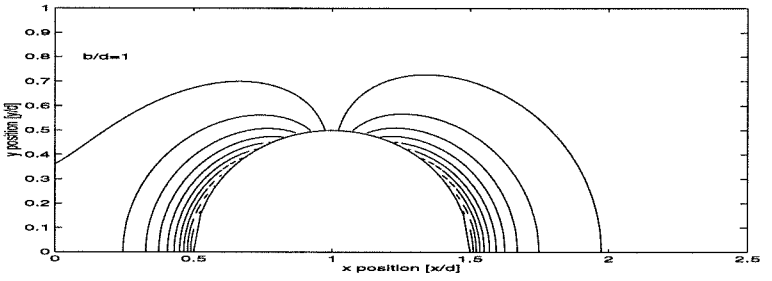

(c) $b/d = 1$

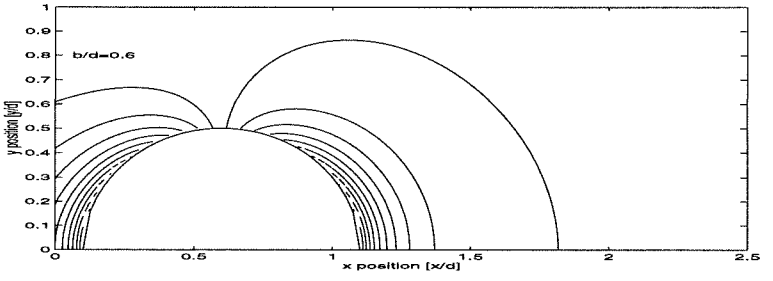

(d) $b/d = 0.6$

Figure 4.2: Impulse distribution for different b/d ratios. The impulse is normalized by $\rho_f u_\tau d$.

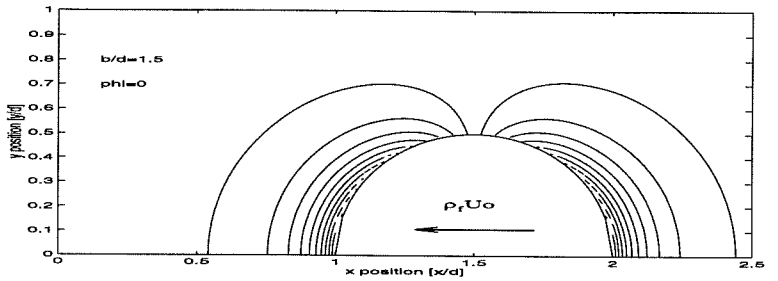

(a) $\phi = 0$

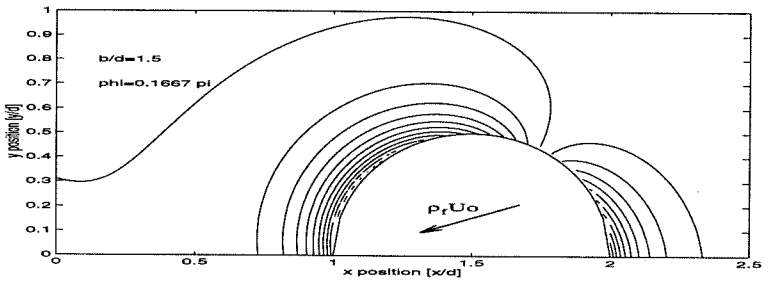

(b) $\phi = 0.166\pi$

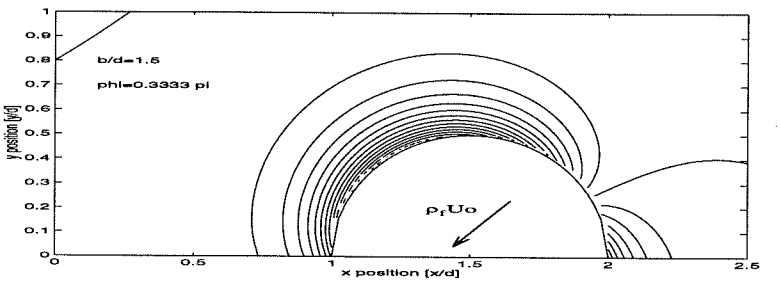

(c) $\phi = 0.333\pi$

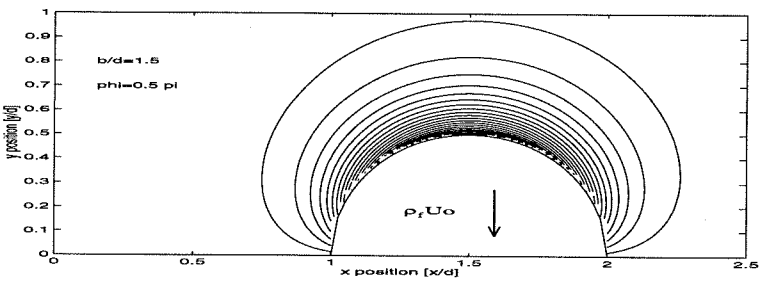

(d) $\phi = \pi/2$

Figure 4.3: Impulse distribution for different angles of incidence ϕ, for $b/d = 1.5$

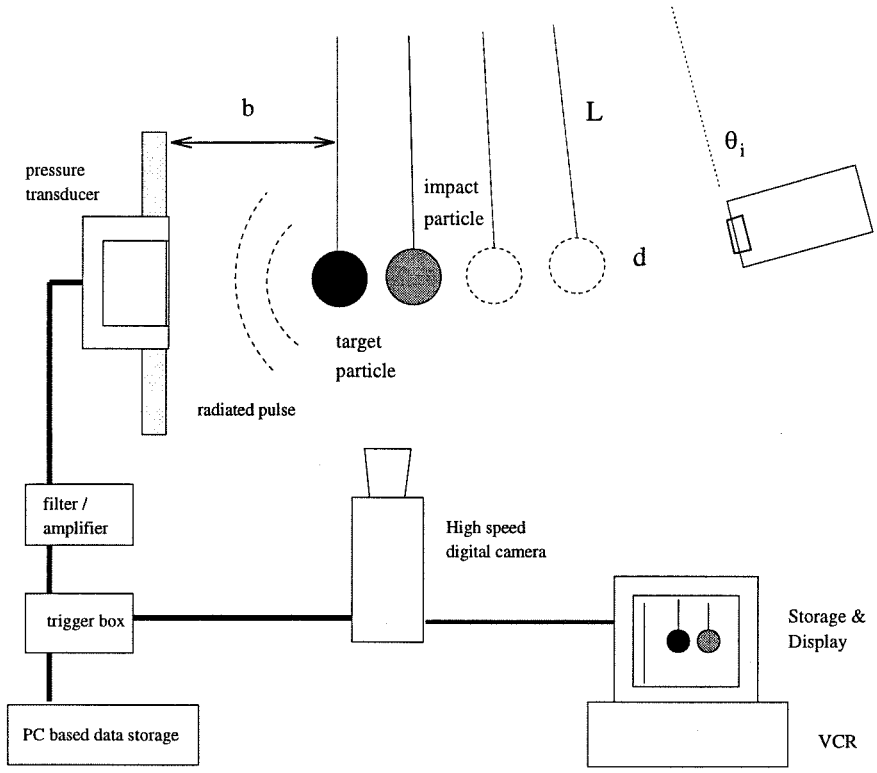

Figure 4.4: Experimental setup of the dual pendulum to measure the impulse pressure produced by a collision.

the nature of this pressure front, an experimental apparatus was set up to produce controlled binary collisions of particles.

The experimental setup is shown in figure 4.4. A simple dual pendulum was set up to generate controlled collisions. A particle was suspended (the target particle) at a certain distance, b, from a wall. On the wall a high-frequency-response pressure transducer was flush mounted. A second particle (the impact particle) was released starting from rest at some initial angle. The impact particle accelerated towards the target particle and produced a collision. The collision produced a sudden acceleration of the target particle and generated an impulsive pressure front. The impulsive pressure pulse was captured by the pressure transducer. The motion of both particles was recorded using a high-speed digital camera, which allowed the velocity and acceleration to be measured moments after the impact occurred. The fluid used for all of the experimental measurements was de-ionized water.

A typical pressure pulse of this kind is shown in figure 4.5. For this particular

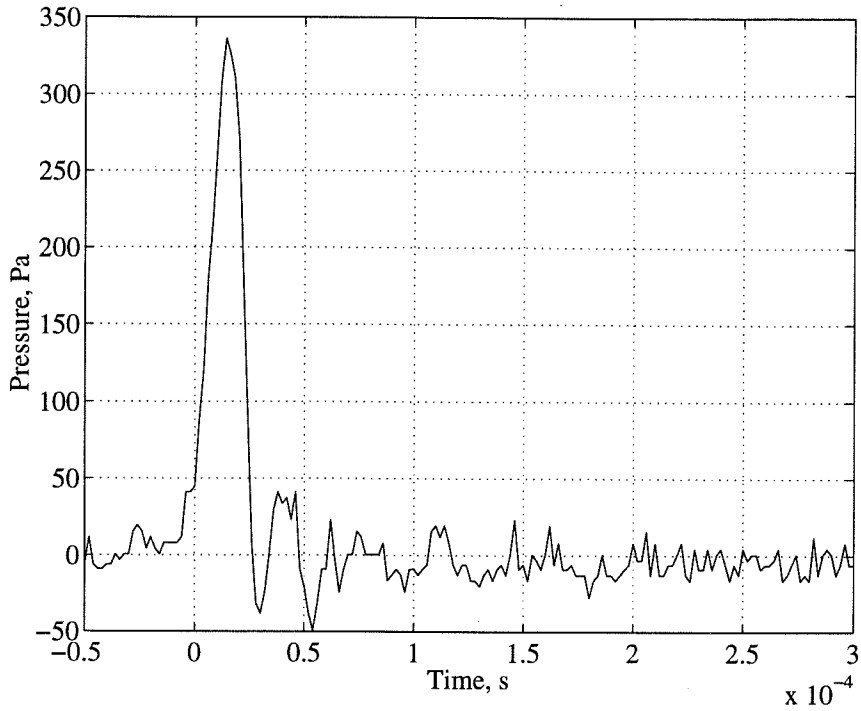

Figure 4.5: Typical pressure pulse impulse pressure produced by a collision of two 4.5 mm steel particles in water.

case the pressure pulse was generated by the collision of two 4.5 mm steel particles. The target particle collided at approximately 13 cm/s, and the distance of the target particle to the wall was 8 mm. Note that after the initial pressure increase a reverberation of the signal can be observed. This oscillating pressure resembles the kind of typical oscillation found in direct collision of particles against the pressure transducer. See appendix A for a brief discussion of these pressure oscillations.

A number of different pairs of particles were used, for a range of impact velocities, and for various incidence angles. The properties of the spheres tested are shown in table 4.1.

The impulse pressure was obtained by integrating the measured pressure pulses[2]. The secondary oscillations were neglected in the reduction of the data. The calibration provided by the pressure transducer manufacturer was used[3].

[2]following the formula in equation 2.10

[3]the calibration of the pressure transducer was verified in Chapter 2.

Material	d_p [mm]	ρ_p/ρ_f	u_t [cm/s]	Re_t
Glass $\times$	3.00	2.54	31.8	954
Glass $*$	4.10	2.54	36.8	1338
Glass o	6.00	2.54	47.4	2583
Steel $\oplus$	4.50	7.78	89.6	3665
Nylon $\otimes$	6.35	1.14	13.6	785

Table 4.1: Properties of particles used in pressure front measurements experiments.

4.3 Results

Figure 4.6 shows the impulse measured for a 6 mm glass sphere as a function of the initial distance from the wall b. The impact velocity for this experiment was constant, determined by the initial angle of release. The nominal impact velocity for the experimental set was 0.0704 m/s. The solid line is the power law fit of the data.

Similarly, figures 4.7 and 4.8 show the maximum pressure and pressure pulse duration respectively, for the same data set. Clearly, the impulse and the maximum pressure decrease as the distance from the wall increases. Not surprisingly, the duration of the pressure pulse appears to remain unchanged for any distance b/d. The power fit of the impulse data shows that the magnitude of the measured impulse decreased approximately as $(b/d)^{-2}$.

Figure 4.9 shows the measured impulse pressure as a function of the predicted impact velocity for 6 mm glass particles. For this case the distance between the target particle and the wall was kept fixed at $b/d = 0.62$. The impact velocity plotted in the horizontal axis is the predicted velocity of approach based on the initial position of the particle. As expected, the magnitude of the impulse increases with the impact velocity. In this case the impulse appears to increase linearly with impact velocity.

Experimental results were obtained also for different angles of motion of the target particle with respect with the wall. Both the distance b/d and the impact velocity were kept constant. The incidence angle represents the angle between the normal to the wall and the trajectory of target particle after the impact (an angle $\alpha = 0$ represents an incidence motion normal to the wall, and $\alpha = \pi/2$ represents an incidence motion

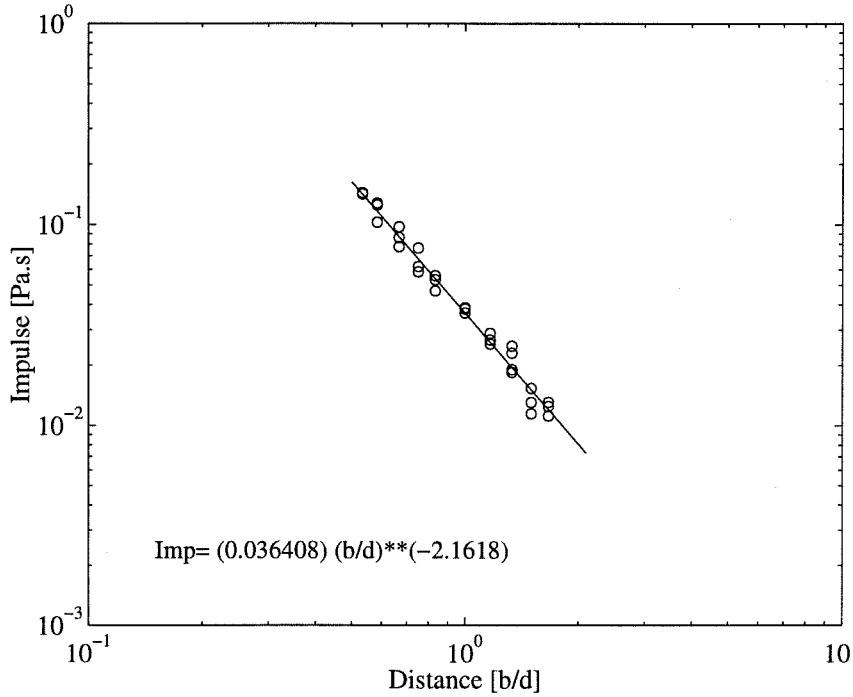

Figure 4.6: Measured impulse-pressure as a function of normalized distance from the wall, b/d. Acceleration of the particle produced by the collision of a particle of the same diameter and density. 6 mm glass particles immersed in water. Velocity of the target particle after impact $\approx 0.0704\ m/s$.

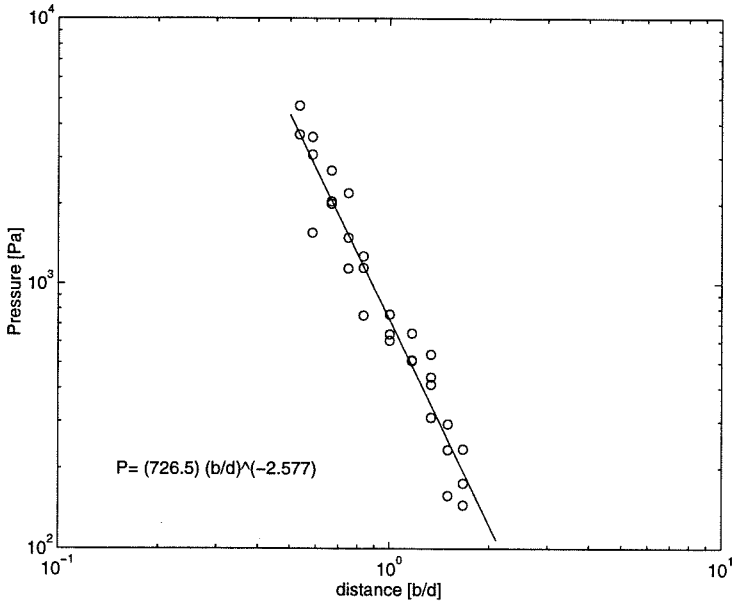

Figure 4.7: Measured maximum pressure as a function of normalized distance from the wall, b/d. Acceleration of the particle produced by the collision of a particle of the same diameter and density. 6 mm glass particles immersed in water. Velocity of the target particle after impact $\approx 0.0704\ m/s$.

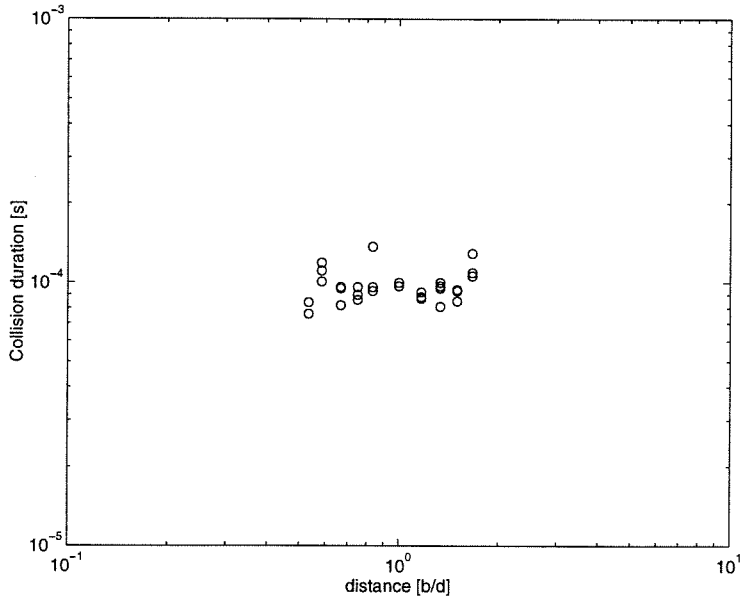

Figure 4.8: Measured pressure pulse duration as a function of normalized distance from the wall, b/d. Acceleration of the particle produced by the collision of a particle of the same diameter and density. 6 mm glass particles immersed in water. Velocity of the target particle after impact $\approx 0.0704\ m/s$.

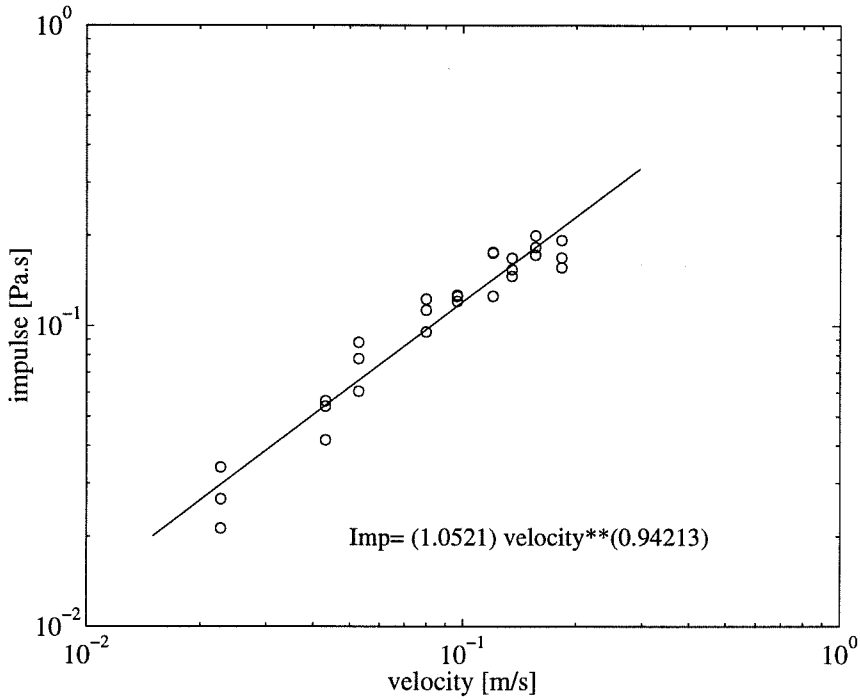

Figure 4.9: Measured impulse pressure as a function of impact velocity. Distance from the wall, $b/d = 0.625$. 6 mm glass particles immersed in water. The solid line shows the power law fit of the data.

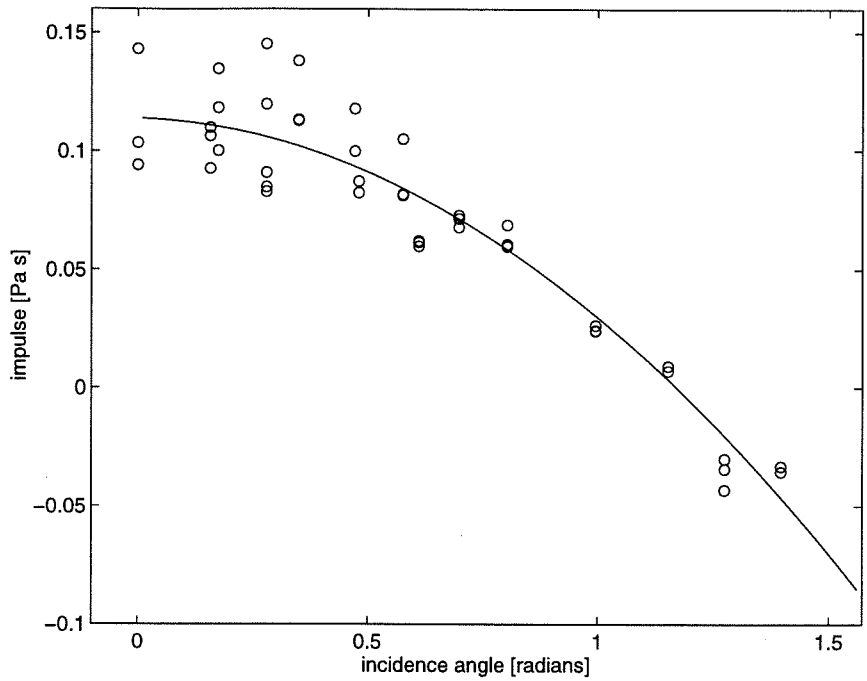

Figure 4.10: Measured impulse pressure as a function of incidence angle ϕ. Distance from the wall, $b/d = 0.65$, and impact velocity = 0.1093 m/s. 6 mm glass particles immersed in water. The solid line shows the best fit of the data.

parallel to the wall). Figure 4.10 shows the measured impulse for 6 mm glass particles as a function of the angle α. For this particular experimental case $b/d = 0.65$ and the calculated impact velocity is 0.1093 m/s.

Clearly, the magnitude of the measured impulse decreases as the motion deviates from normal incidence. Note that when the incidence angle is greater than $2/5\pi$ the impulse is negative, which means that the pressure pulse captured by the transducer decreased at the time of contact.

Results were obtained for particles of various diameters and densities. Impulses as a function of b/d for three different diameters of glass spheres are shown in figure 4.11. It can be observed that the larger the particle, the larger the magnitude of the measured impulse. However, it is important to note that the impact velocities for these three cases are different. For the pendulum experimental setup, the control over the impact velocities is limited to a certain range of velocities for each kind of particle. To match velocities for different particles was not a simple task.

Figure 4.12 shows the measurements obtained for pairs of particles with different

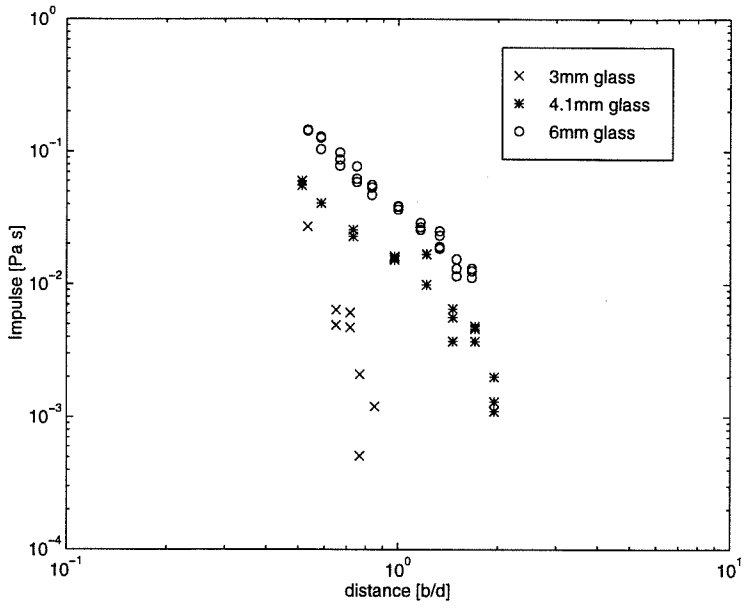

Figure 4.11: Comparison of the measured impulse-pressure as a function of normalized distance from the wall, b/d, for different diameter glass particles immersed in water: 6 mm glass ($\circ$), $u_\tau = 0.0704\ m/s$; 4.1 mm glass ($*$), $u_\tau = 0.0596\ m/s$; 3 mm glass ($\times$), $u_\tau = 0.0544\ m/s$.

densities. With the present experimental setup, it was not possible to match the impact velocities; therefore, the results are not readily comparable.

Thus, to further compare the measured pulses for different particles, a normalization of the impulse pressure was adopted. Following the scaling implied in 4.6,

$$\hat{I} = \frac{I}{\rho_f u_\tau d}. \tag{4.8}$$

From this normalization, the measured impulse as a function of impact velocity (shown in figure 4.9) appears to be nearly independent of the impact velocity, which allows direct comparison when the impact velocity is not the same.

Figure 4.13 shows the normalized impulse for all the particles tested as a function of distance, b/d. The data appears to collapse to a single line for the "heavy" particles. The 6 mm glass, 4 mm glass and the 4.5 mm steel particle impulses fall in the same band of values. The "light" particles appear to deviate from this trend. The dependence on distance for these particles appears to have a larger slope.

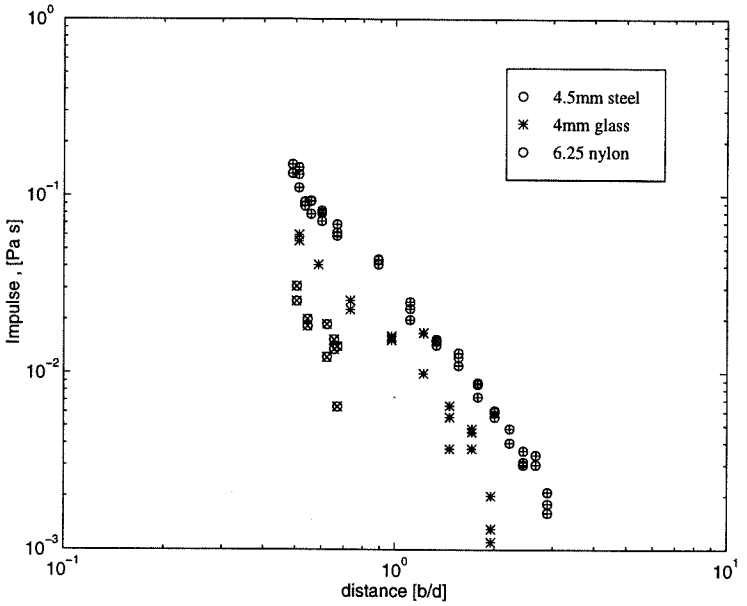

Figure 4.12: Comparison of the measured impulse-pressure as a function of normalized distance from the wall, b/d, for different density particles immersed in water: 4.1 mm glass $(*)$, $u_\tau = 0.0596\ m/s$; 4.5 mm steel $(\oplus)$, $u_\tau = 0.0934\ m/s$; 6.35 mm nylon $(\otimes)$, $u_\tau = 0.0249\ m/s$.

4.4 Comparisons with impulse-pressure theory

Comparisons can be made between the experimental results and the predictions from impulse-pressure theory. Equation 4.6 is re-written to express the impulse at the wall, at $(0,0)$, as a function of b/d, and by normalizing by $\rho_f u_\tau d$ leads simply to

$$\hat{I}_w = \frac{1}{8}\left(\frac{d}{b}\right)^2. \tag{4.9}$$

The dashed line in figure 4.14 shows the calculated impulse from this expression, for the same experimental parameters. The prediction slightly overestimates the experimental measurements but follows the trend well.

In the present experiment two real particles collide and. therefore, in an approximate solution, two doublets. One doublet has positive strength, $\rho_f u_\tau$, at $x = -b$ and the second one has negative strength, $-\rho_f u_\tau$, at $x = -(b+d)$, and thus image doublets at $x = b$ and $x = b + d$. This leads to the approximate impulse condition of

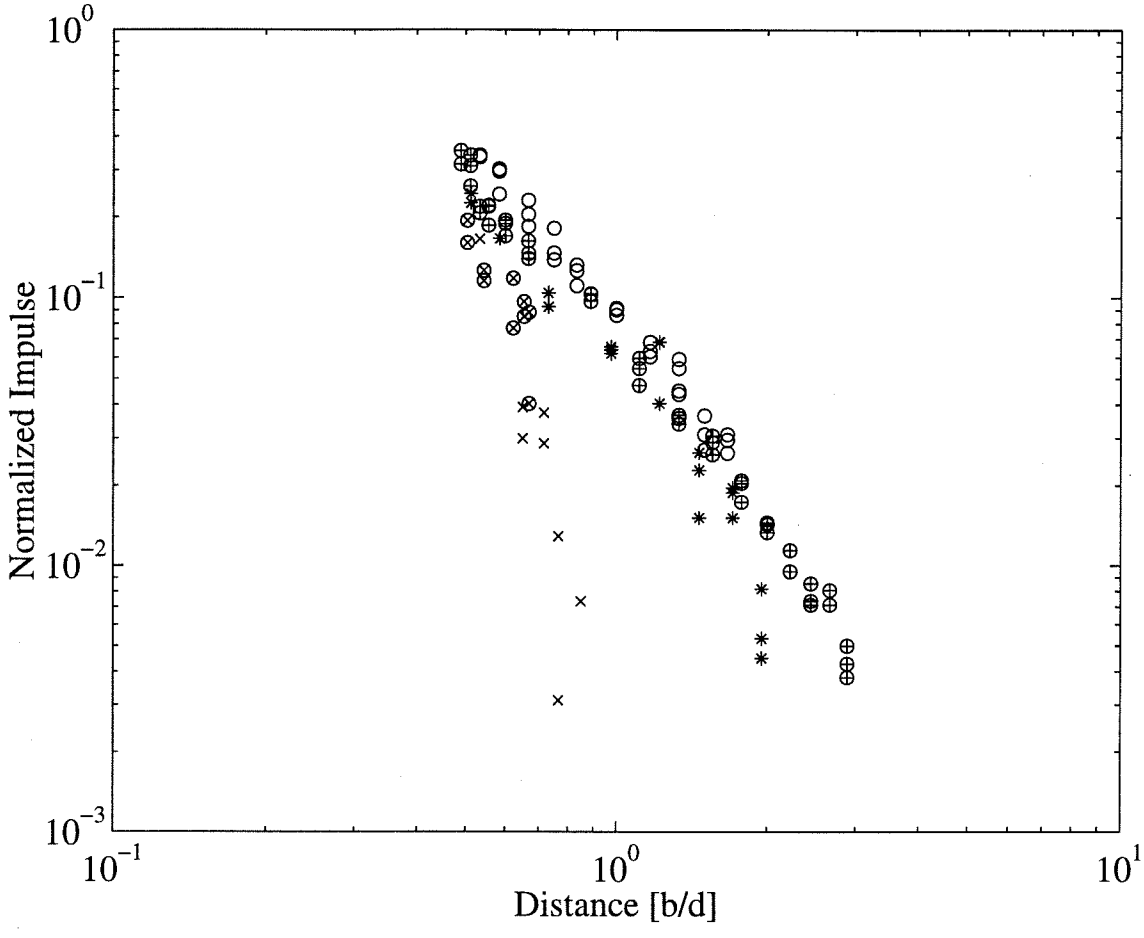

Figure 4.13: Comparison of the normalized impulse-pressure, $\hat{I}$, as a function of normalized distance from the wall, b/d, for all tested particles. 6 mm glass ($\circ$), $u_\tau = 0.070\ m/s$; 4.1 mm glass ($*$), $u_\tau = 0.059\ m/s$; 3 mm glass ($\times$), $u_\tau = 0.054\ m/s$; 4.5 mm steel ($\oplus$), $u_\tau = 0.093\ m/s$; 6.25 mm nylon ($\otimes$), $u_\tau = 0.025\ m/s$.

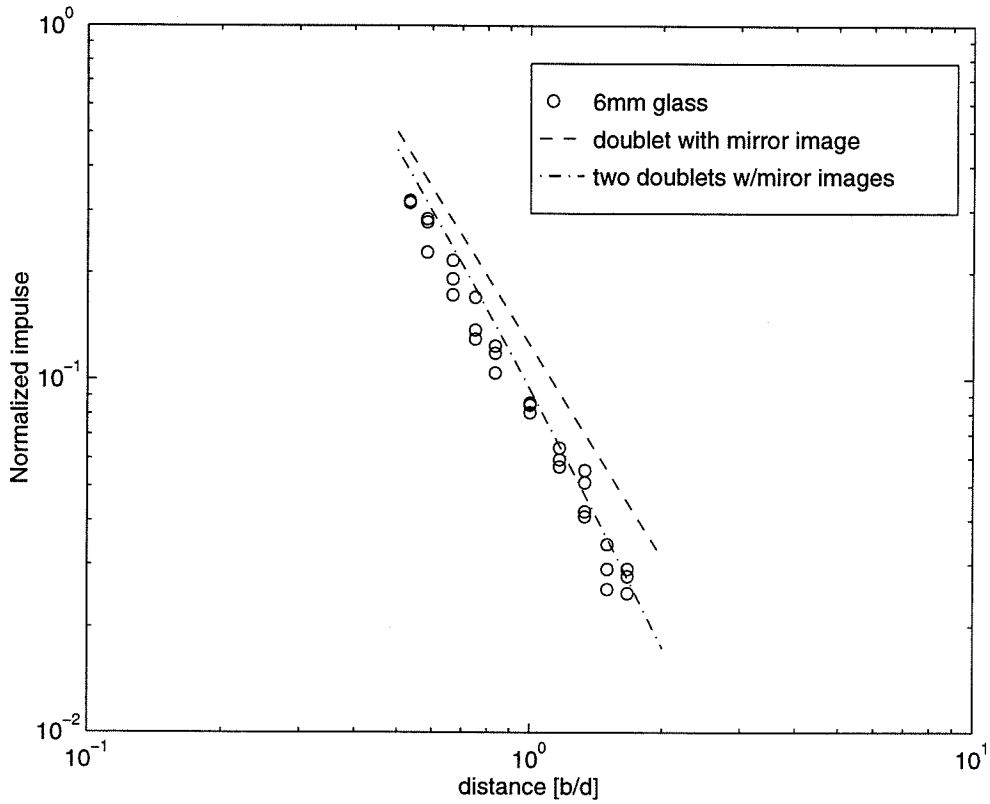

Figure 4.14: Comparison between theory and experiments of the normalized impulse-pressure, $\hat{I}$, as a function of normalized distance from the wall, b/d. 6 mm glass (o), $u_\tau = 0.0704\ m/s$. Equation 4.9 $(- - -)$; equation 4.11 $(- \cdot -)$.

zero velocity normal to the wall. Therefore,

$$I = \tfrac{1}{2}\rho_f u_\tau (d/2)^3 \left(\frac{x+b}{((x+b)^2+y^2)^{3/2}} - \frac{x+b+d}{((x+b+d)^2+y^2)^{3/2}} - \frac{x-b}{((x-b)^2+y^2)^{3/2}} + \frac{x-b-d}{((x-b-d)^2+y^2)^{3/2}} \right) \tag{4.10}$$

Thus, the normalized impulse at the wall reduces to

$$\hat{I}_w = \frac{1}{8}\left(\frac{d}{b}\right)^2 \left(\frac{\frac{2b}{d}+1}{\left(\frac{b}{d}+1\right)^2} \right) \tag{4.11}$$

The dashed-dotted line in figure 4.14 shows the calculated impulse for the case of two doublets with their respective images. The prediction appears to predict the experimental measurements very well.

Now, examining the dependence on the angle of incidence, equation 4.7 leads to a normalized impulse at the wall,

$$\hat{I}_w = \frac{1}{8}\left(\frac{d}{b}\right)^2 \cos\phi. \tag{4.12}$$

In figure 4.15, the dashed line shows the calculated normalized impulse as a function of the angle of incidence. The experimental data obtained for the same parameters is shown in the figure. The model appears to predict the magnitude of the impulse pressure well for angles below $\pi/6$.

The two-particle and four-doublet approach which led to equation 4.10, leads in the case of an oblique collision to

$$I = \tfrac{1}{2}\rho_f u_\tau (d/2)^3 \left(\frac{(x+b)\cos\phi - y\sin\phi}{((x+b)^2+y^2)^{3/2}} - \frac{(x-b)\cos\phi - y\sin\phi}{((x-b)^2+y^2)^{3/2}} - \frac{(x+b+d\cos\phi)\cos\phi - (y-d\sin\phi)\sin\phi}{((x+b+d\cos\phi)^2+(y-d\sin\phi)^2)^{3/2}} + \frac{(x-b-d\cos\phi)\cos\phi - (y-d\sin\phi)\sin\phi}{((x-b-d\cos\phi)^2+(y-d\sin\phi)^2)^{3/2}} \right) \tag{4.13}$$

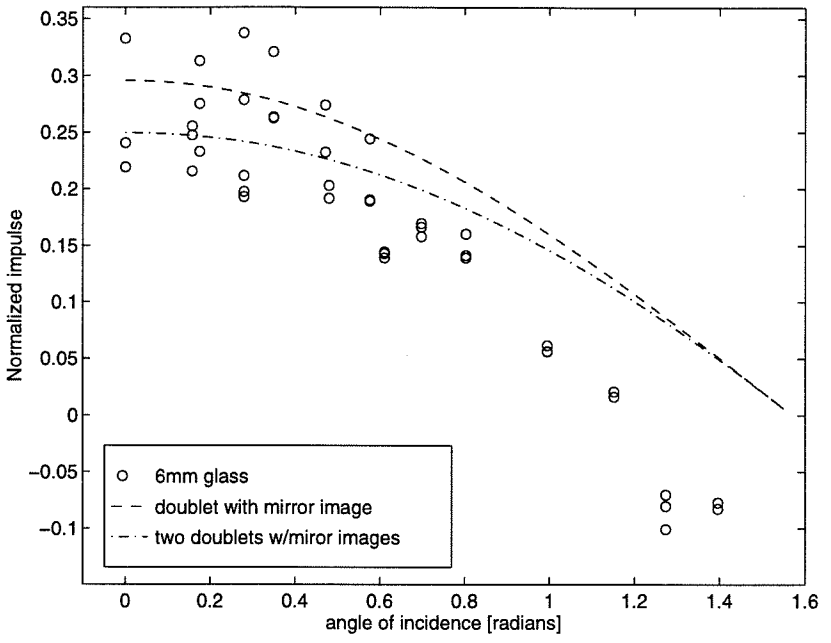

Figure 4.15: Comparison between theory and experiments of the normalized impulse-pressure, $\hat{I}$, as a function of angle of incidence ϕ. 6 mm glass ($\circ$), $u_\tau = 0.109\ m/s$. Equation 4.12 ($- - -$); equation 4.14 ($- \cdot -$).

which leads to an impulse at the wall given by

$$\hat{I}_w = \frac{1}{8}\left(\frac{d}{b}\right)^2 \cos\phi \left(1 - \frac{(1+\frac{d}{b}\cos\phi)\cos\phi}{((1+\frac{d}{b}\cos\phi)^2 + (\frac{d}{b}\sin\phi)^2)^{3/2}}\right). \tag{4.14}$$

The dashed-dotted line in figure 4.15 shows the prediction from the expression above. The model appears to predict the magnitude of the impulse better than equation 4.12, but also over-estimates the magnitude for angles above $\pi/5$, and fails to predict the 'negative impulse' found in the experimental measurements.

4.5 Discussion

An extra contribution to the collisional component of the particle pressure was recognized. The radiated component of the collisional particle pressure was identified from the analysis of the probability density functions and from a detailed visualization system. The collision of two particles in the bulk of the flow produces sudden changes

in their velocities and, as a result, a pressure front is generated which is radiated through the interstitial fluid.

The existence of this component of the particle pressure has not been recognized in the past. In the present chapter, a series of experimental measurements were performed to further investigate the nature of the pressure pulse generated by a particle collision.

By means of a series of simple experiments, the radiated pulses were reproduced in a controlled fashion. Binary collisions were generated using a dual pendulum. One of the particles was suspended at rest at a particular distance from the transducer, while the other was swung from some initial angle. The collision produced an impulse acceleration of the target particle, which produced a pressure front which was transmitted from the point of contact to the surface of the transducer through the interstitial fluid. Measurements of pressure pulses produced by binary collisions were obtained for a variety of particles for a range of impact velocities and incident angles. The magnitude of the radiated impulse was found to be related to the impact velocity, the diameter of the particles and the distance from the wall. When the measured impulses are normalized using

$$\hat{I} = \frac{I}{\rho_f u_\tau d} \tag{4.15}$$

the data appears to collapse into a single curve. Particles with small mass appear to deviate from this trend, which may be because the range of impact velocities for these particles is much smaller than those for any of the other particles. In this case, for smaller velocities, the viscous effect may be more important thereby introducing other scaling parameters to the problem. Also, since the magnitude of the pressure pulses generated was small for the attainable velocities, measurements were only possible at close distances from the transducer. Greater impulsive velocities for the light particles could be achieved by using a more dense particle as the impact particle.

To further investigate the nature of these pressure pulses, an analysis was carried out using the pressure-impulse theory (Batchelor, 1967). By neglecting both convective and viscous effects in the equation of motion and integrating through the impact

time, if the flow is incompressible, it can be obtained that

$$\nabla^2 I = 0$$

where I is the pressure impulse. Approximate expressions for the solution of the impulse field of a solid sphere near a wall were obtained using superposition of doublets.

The prediction from the pressure-impulse theory appears to agree very well with the experimental measurements. Even the simple doublet appears to follow the same decay. When the effects of the second particle are included, the slope and magnitude of the measurements are matched closely by the prediction. It is important to note that even for small distances, the prediction and the experiments match well, although the solid boundary condition on the spheres is only satisfied approximately.

Although the prediction from pressure-impulse theory shows very good agreement with the experimental measurements for normal and small angles of motion, it fails to predict the measured impulses for acute angles of incidence. When the angle of incidence is taken into account in the calculation, the model predicts a reduction of the impulse which resembles that found in the experimental measurements but only for angles smaller than $\pi/6$. For greater angles the model fails to predict the large reduction of the impulse and also fails to predict the negative values found in the experiments. The model is based on an inviscid approximation, therefore the boundary condition on the surface of the sphere differs greatly from that in the experiment, specially in non-normal angles. This may lead to the discrepancy found between the experiment and the prediction for acute angles of incidence.

Chapter 5 Solid fraction fluctuations in liquid-solid flows

5.1 Introduction

In Chapter 2 measurements of the particle pressure were presented and analyzed. Particle-wall and particle-particle collisions were studied since the particle pressure is composed of pressure pulses generated from these events. In this chapter, by contrast, a study of one source of the particle pressure is examined. The origin of the velocity fluctuations that cause particles to collide is analyzed by quantifying the fluctuation of the concentration of solid particles.

Dispersed solid-liquid mixtures are inherently unsteady. Experimental and industrial applications provide evidence to show that the velocities of both the fluid and solid phases and their respective volume fractions experience important fluctuations around their mean values. Because of this agitation, the effective coefficients of heat and mass transfer have extremely high values, a reason why these systems are of interest for many engineering applications. Multiple factors determine the nature of these fluctuations, such as the upstream and downstream conditions, the density ratio of the phases and the mean slip velocity. The interaction between the phases is complex, and significant momentum is transferred between the phases and with the boundaries.

In general, the fluctuations of the solid fraction can be divided into large and small scale fluctuations (Couderc, 1985). Large scale fluctuations include those disturbances related to 'bubbles' in fluidized beds. These large-amplitude (low-frequency) disturbances, or waves, have been studied intensively from the stability point of view (Batchelor, 1988). Fluctuations of this sort are strongly dependent on external conditions, such as the geometry of container or characteristics of the fluid distribution

system, etc. Small scale fluctuations are induced by inter-phase interactions, local hydrodynamics, and presumably particle collisions (Buyevich and Kapbasov, 1994).

Didwania & Homsy (1981) performed a detailed analysis of the flow regimes and transitions in liquid fluidized beds. The characterization of four distinct regimes was given in terms of the time and length scales of the particle motion measured by optical techniques. The regimes include (in the order of decreasing solid fraction), wavy flow, wavy flow with transverse structure, fine scale turbulent flow and bubbling states. Comparisons of their results with the present measurements will be presented in this chapter.

By experimentally measuring the variation of the solid fraction, a measure of the fluctuation can be obtained. The instantaneous cross-section averaged solid fraction was measured using an impedance volume fraction meter. This technique was first used by Kytömaa (1987). Experiments were performed in a liquid fluidized bed and in a vertical gravity-driven liquid-solid flow. The variance of the measured time-signal was obtained for different particle densities.

5.1.1 Modeling random fluctuations in liquid-solid flows

The steady behavior of fluidized systems has received a considerable amount of attention (see Di Felice (1995) for a review article). The unsteady nature of such flows has been attacked from different approaches, most of them dealing with the formation of large global fluctuations, or bubbles. Less attention has been focused on the study of the small-scale fluctuations. Buyevich and Kapvasov (1994) proposed a mathematical model to study the random small-scale fluctuations of particles in a fluid in a macroscopically uniform disperse mixture. The model assumes that momentum is transferred mainly through direct collisions. Assuming that the fluctuations in the system are isotropic and following an analysis inspired by thermodynamic theory of fluctuations, an expression for the mean square number density fluctuations is obtained. The mean square number density fluctuations are found to be related to the granular temperature and the granular chemical potential. From geometric consider-

ations, an expression for the solid fraction fluctuation as a function of the mean solid fraction is derived. Based on a Carnahan-Starling model, it is obtained

$$\overline{\nu'^2} = \nu^2 \left[1 + 2\nu \frac{4-\nu}{(1-\nu)^4} \right]^{-1} \tag{5.1}$$

where ν is the mean value of the solid fraction, and ν'^2 is the mean square solid fraction fluctuation. The authors then discuss the validity of the Carnahan-Starling model for high concentrations. An alternative expression is derived based on the Enskog model for dense gases, leading to

$$\overline{\nu'^2} = \nu^2 \left[1 + \left(\frac{\nu}{\nu_*} \right)^{1/3} \right] \left[1 + \frac{1}{3} \left(\frac{(\nu/\nu_*)^{1/3}}{1-(\nu/\nu_*)^{1/3}} \right) \right]^{-1} \tag{5.2}$$

where ν_* is the empirical value of solid fraction at close packing. The model presented by Buyevich *et al.* is of great complexity and many of the assumptions made are non-trivial.

5.2 Experiments

The experiments involve a vertical gravity driven flow using glass particles in water (with density ratio, $\rho_p/\rho_f = 2.5$), and a liquid fluidized bed using glass, steel and nylon particles of a range of diameters. Figure 5.1 shows a sketch of the experimental setup. By changing downstream conditions the solid fractions can be varied from 0.02 to 0.60. An Impedance Volume Fraction Meter (IVFM) developed by Kytömaa and Brennen (1986) and Bernier (1982) is used to measure the instantaneous volume fraction. This non-intrusive instrument is based on the measurement of the high-frequency electric impedance of the mixture and consists of two shielded stainless steel electrodes laid flush with the interior surface of the tube. The meter provides a cross-sectional average measurement of the impedance in the test section. To provide a high frequency response, the measuring electronics use a 50 kHz excitation and a double bridge signal processor. Due to the shielded configuration of the electrodes, the spatial

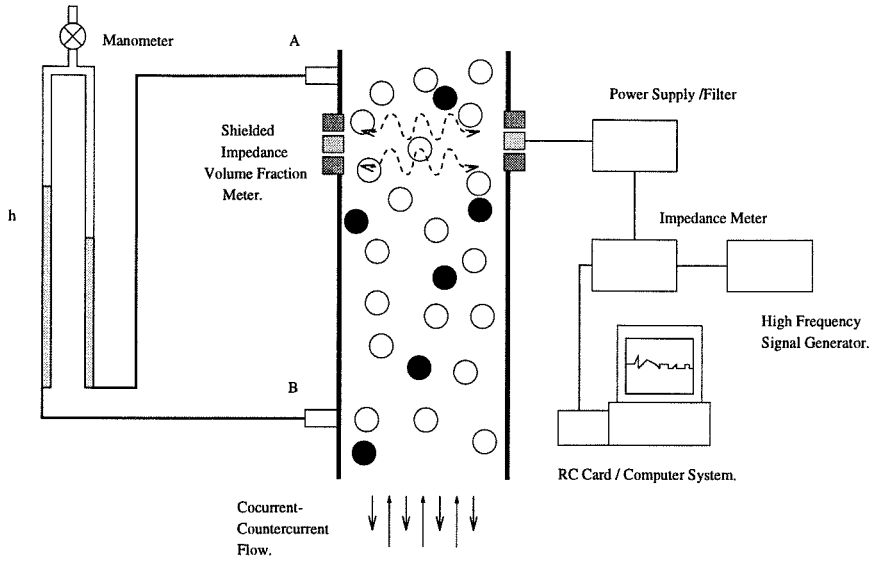

Figure 5.1: Experimental setup to measure the fluctuations of the solid fraction signal in a liquid solid flow.

resolution is a few centimeters. A set of two meters was placed in the test section, such that possible passing waves could be detected and their velocity measured. All the experiments were performed in the water loops described in Chapter 2. Sets of electrodes were adapted for use in two different test section internal diameters, 5.08 cm and 10.19 cm.

To calibrate the IVFM a manometer was connected to the test section. The solid fraction was determined from the hydrostatic pressure gradient in the two-component medium obtained from the manometer reading. If h' is the distance between points A and B and h is the difference in the manometer levels (see figure 5.1), then in the absence of frictional effects, the solid fraction is given by

$$\nu = \frac{h}{h'(\rho_p/\rho_f - 1)} \tag{5.3}$$

where ρ_p is the density of the particles and ρ_f is the density of the fluid. Figure 5.2 shows a typical calibration for 3 mm glass spheres in a 10.16 cm test section. The response of the meters is linear for the entire range of concentrations. The same linear response was obtained for all the particles tested.

The dynamic response of the meter can be quantified by obtaining the decay time

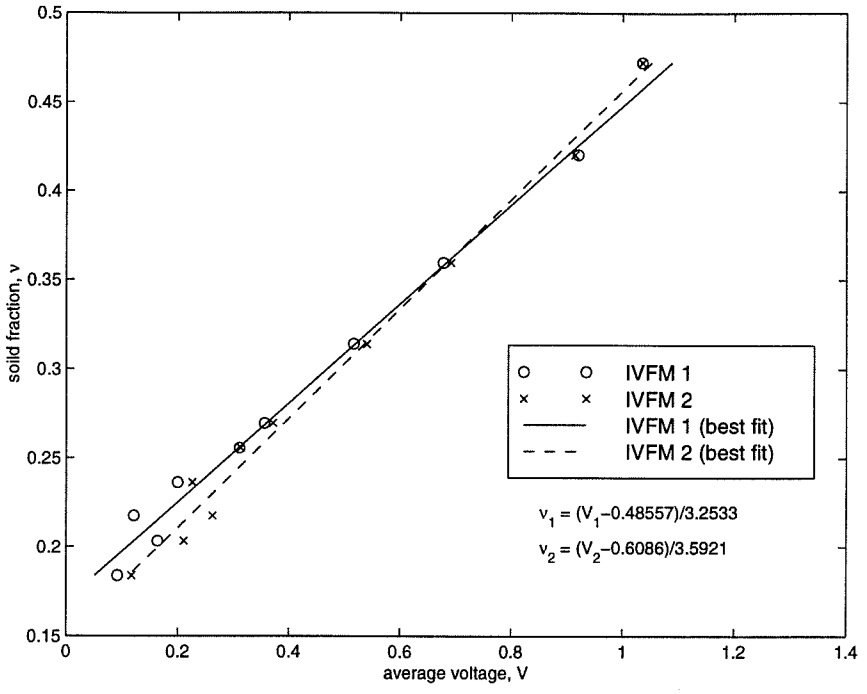

Figure 5.2: Typical calibration of the impedance volume fraction meters. 3 mm glass particles in a 10.18 cm test section liquid fluidized bed.

of the autocorrelation function of the impedance-time signal of the flowing mixtures. The dynamic response calibration is discussed in detail by Kytömaa (1987).

The root mean square (rms) fluctuation of the solid fraction, $\overline{\nu'}$, is calculated as

$$\overline{\nu'^2}^{1/2} = \sqrt{\frac{1}{N}\sum_{i=1}^{N}(\overline{\nu} - \nu_i)^2} \tag{5.4}$$

where $\overline{\nu}$ is the average solid fraction. The measurements were obtained by setting a certain sampling rate and length of sample in the data acquisition system. The sampling rate for all the results presented was chosen to be 1 kHz. Samples of at least 8000 data points (8 seconds at 1kHz) were used for the calculations.

The measurement of the unsteady component of the volume fraction was first proposed and used by Kytömaa (1987). In his investigation, the solid fraction fluctuations were used to measure small and large amplitude kinematic stability and wave propagation in two and three components flows. In this chapter, the emphasis is not on wave propagation or stability. The technique is used to measure the amount of

agitation in solid-liquid flows in order to investigate the flow regime transitions and, ultimately, to identify the generating mechanisms of the particle pressure.

5.3 Results

5.3.1 Liquid fluidized beds

For the first part of this study the experiment was set to operate in the form of a liquid fluidized bed (see Chapter 2). The particles were placed in the test section and by controlling the liquid flow, different steady state mixtures could be achieved. To eliminate the possible presence of transients, the measurement of the solid fraction was taken a few minutes after the steady state was reached. In most cases the measurement was taken a number of times to ensure repeatability.

Figures 5.3 to 5.6 show typical cases of the volume fraction signals for the case of a fluidized bed for different particle densities and diameters. The figures show, on the left column, the solid fraction measured as a function of time for different mean solid fractions. On the right, the frequency transformed signals are shown. A fast Fourier transform algorithm was used to obtain the frequency domain plots. Before the transform was applied, the mean solid fraction was subtracted in order to isolate the fluctuating component of the solid fraction time traces. The vertical axis of the frequency domain plots can be interpreted as the energy of the fluctuations.

Figure 5.3 shows the results obtained for 3 mm glass particles in a 5.08 cm diameter test section. The presence of large-scale fluctuations can be readily observed at high concentrations. These low frequency waves can be observed in the experiment as upwards moving regions of lower concentration. As the solid fraction decreases, these waves become more irregular as higher frequency fluctuations begin to appear. For most concentrations the low frequency fluctuations contain the most energy. As the concentration decreases, the fluctuation energy is distributed into a wider range of frequencies. Note the presence of a spike at 60 Hz for all cases, most likely the result of electronic noise.

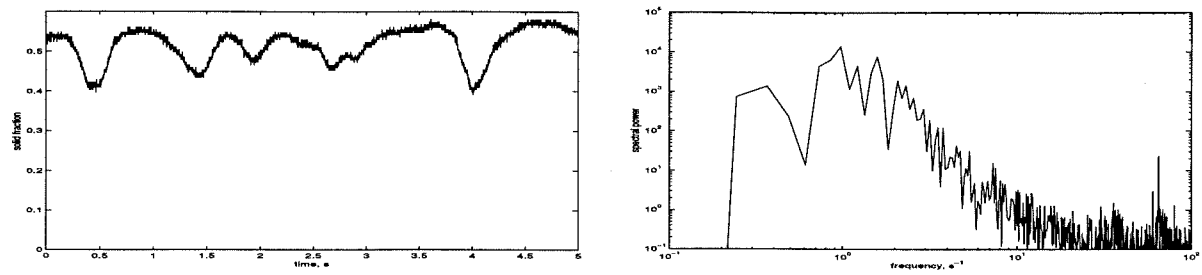

(a) $\overline{\nu} = 0.50$

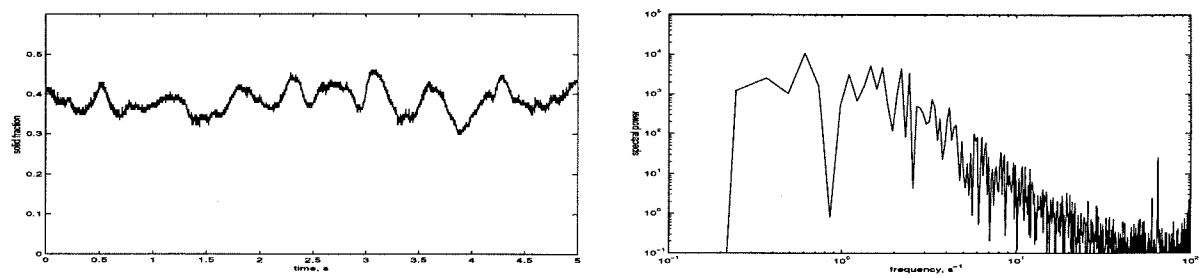

(b) $\overline{\nu} = 0.38$

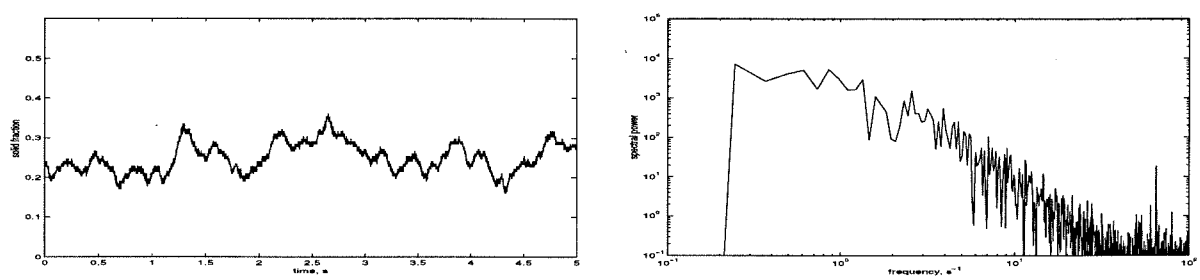

(c) $\overline{\nu} = 0.23$

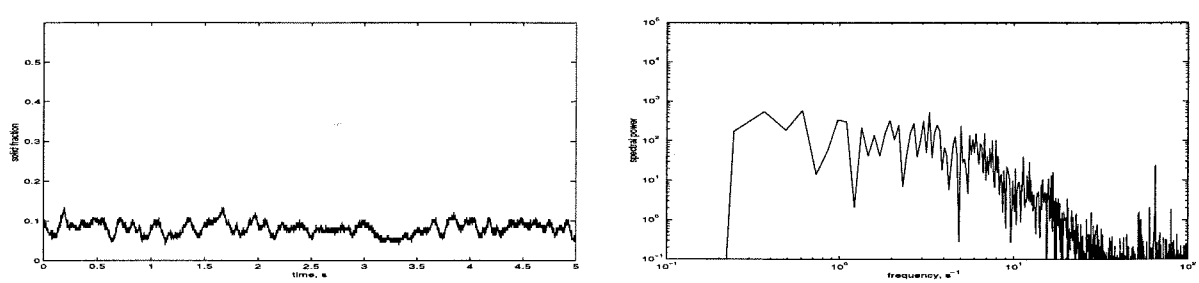

(d) $\overline{\nu} = 0.08$

Figure 5.3: Time and frequency domain volume fraction traces for a liquid fluidized 3 mm glass particles in a 5.08 cm diameter test section.

Figure 5.4 shows the results for four typical concentrations for the cases of 6 mm glass spheres fluidized in a 5.08 cm test section. For the case of the highest concentration, the large scale disturbances begin to appear. This concentration (51%) is just beyond that of the incipient fluidization for this case. As concentration decreases the large-scale fluctuations appear and seem to be of larger magnitudes than those of the 3 mm glass case. As in the previous case, as the mean solid fraction decreases the presence of low frequency fluctuations becomes less prominent and higher frequency motions begin to appear. In the case of low concentrations, the frequencies of fluctuation are distributed over a wide frequency range.

The results obtained for fluidized 6.35 mm nylon spheres are shown in figure 5.5. Large scale fluctuations are observed for most concentrations, and high frequency fluctuations appear to be less evident than in the two previous cases.

Figure 5.6 presents the measurements obtained for the 4.5 mm steel particles. Similar to the previous cases, large-scale fluctuations can be observed in concentrated beds. This large fluctuations were easily observed in the experiment as bands of low concentration traveling upwards. For this type of particles, such waves could be observed for concentrations up to 30%. The rms fluctuation values measured for this case were the largest of all the cases tested.

The rms solid fraction fluctuation, as calculated from equation 5.4, is presented in figure 5.7, for all the particles tested. Only the measurements obtained for the 5.08 cm diameter test section are presented. In a packed state, when the fluid velocity has just reached the minimum fluidization velocity, the amount of fluctuation is small. As the solid fraction decreases, the mean fluctuation increases rapidly and reaches a local maximum at concentrations of approximately 45%. The aforementioned large-scale fluctuations, or concentration waves, are the main cause of this rapid increase in the fluctuation. The magnitude of the concentration waves decreases as the solid fraction is further reduced, and the small-scale fluctuations begin to appear. Around a solid fraction of 30%, another local maximum in the mean fluctuation appears. In this range of concentrations, the small-scale fluctuations appear to be dominant. For concentrations lower than 30%, the mean fluctuation decreases again. For dilute mix-

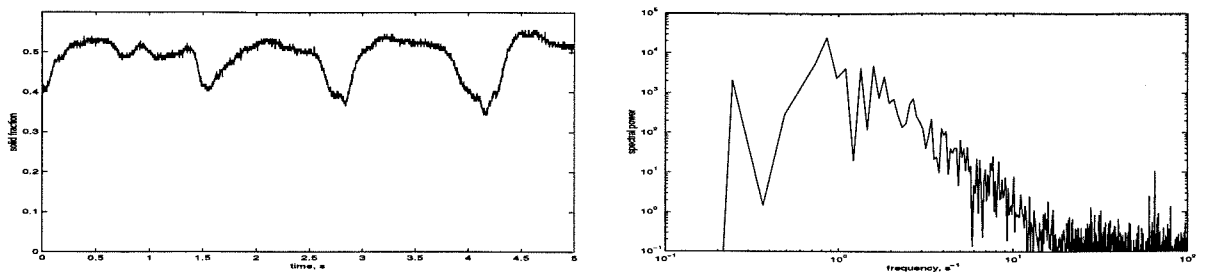

(a) $\overline{\nu} = 0.51$

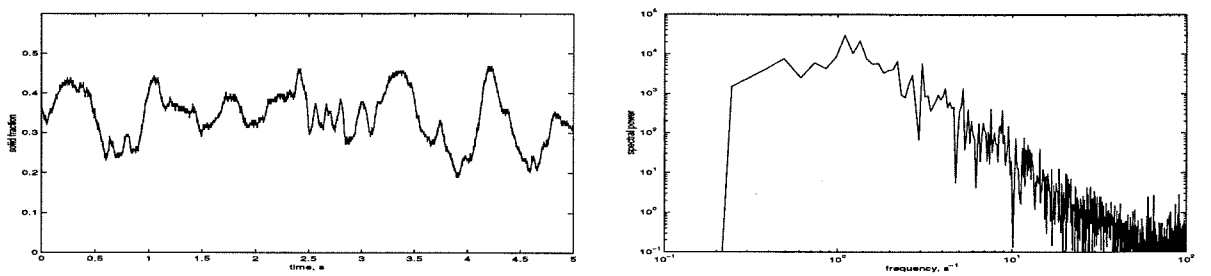

(b) $\overline{\nu} = 0.37$

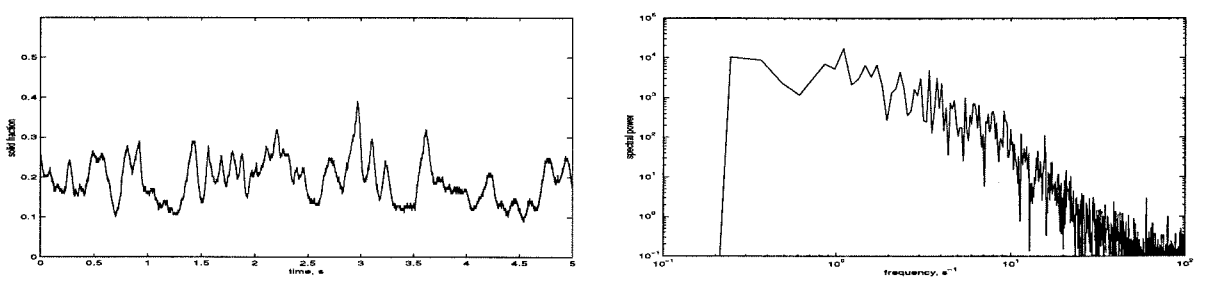

(c) $\overline{\nu} = 0.23$

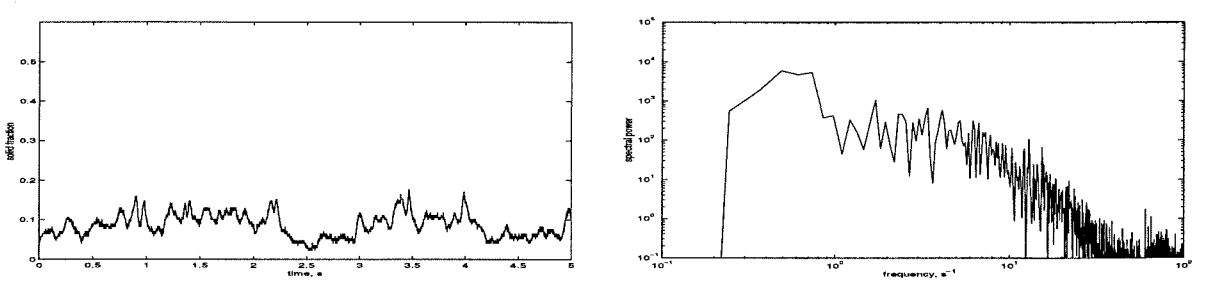

(d) $\overline{\nu} = 0.11$

Figure 5.4: Time and frequency domain volume fraction traces for liquid fluidized 6 mm glass particles in a 5.08 cm diameter test section.

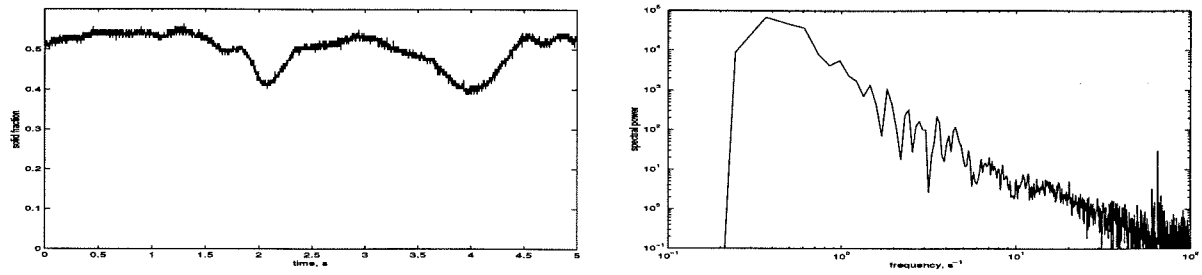

(a) $\overline{\nu} = 0.50$

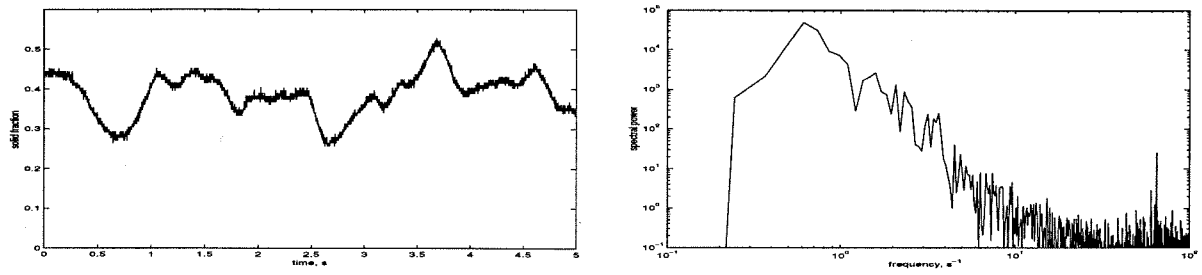

(b) $\overline{\nu} = 0.39$

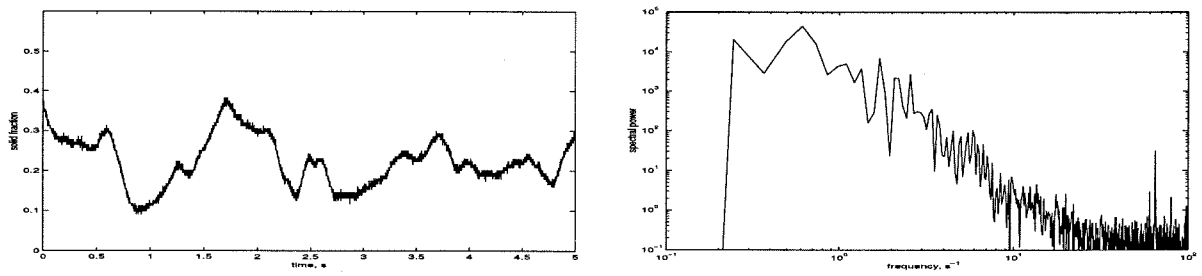

(c) $\overline{\nu} = 0.25$

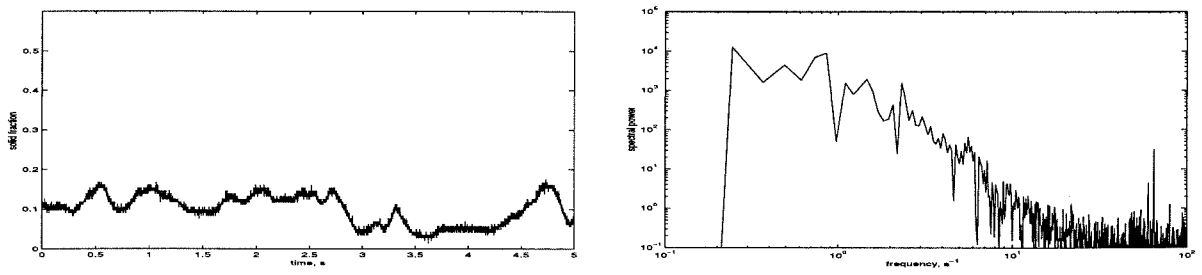

(d) $\overline{\nu} = 0.11$

Figure 5.5: Time and frequency domain volume fraction traces for liquid fluidized 6.35 mm nylon particles in a 5.08 cm diameter test section.

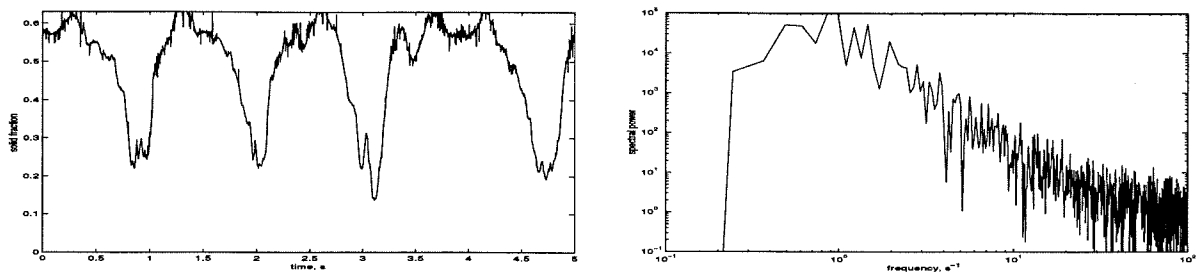

(a) $\overline{\nu} = 0.47$

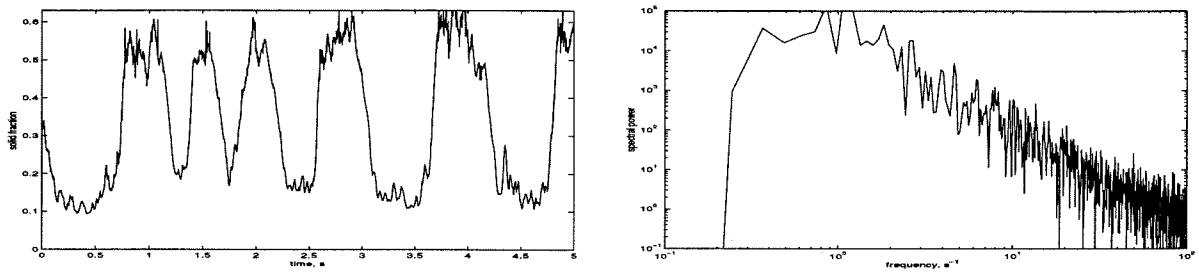

(b) $\overline{\nu} = 0.37$

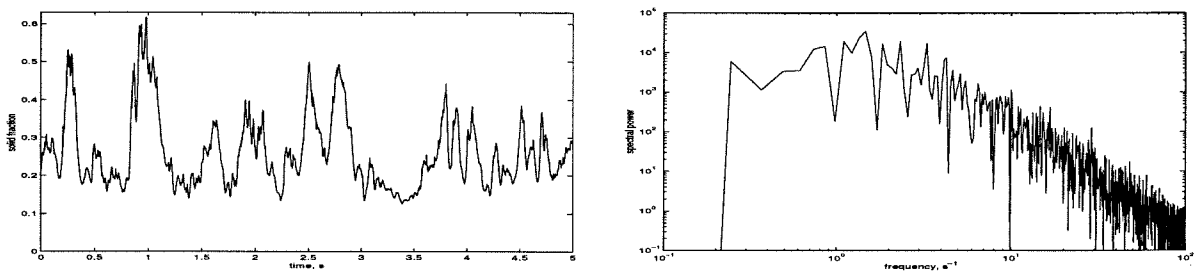

(c) $\overline{\nu} = 0.26$

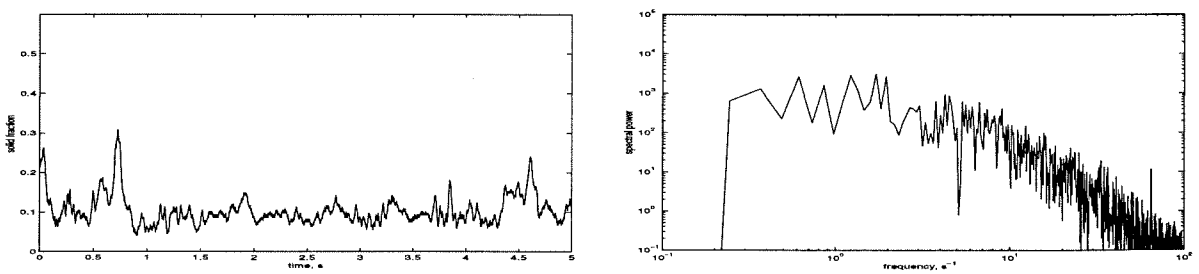

(d) $\overline{\nu} = 0.10$

Figure 5.6: Time and frequency domain volume fraction traces for liquid fluidized 4.5 mm steel particles in a 5.08 cm diameter test section.

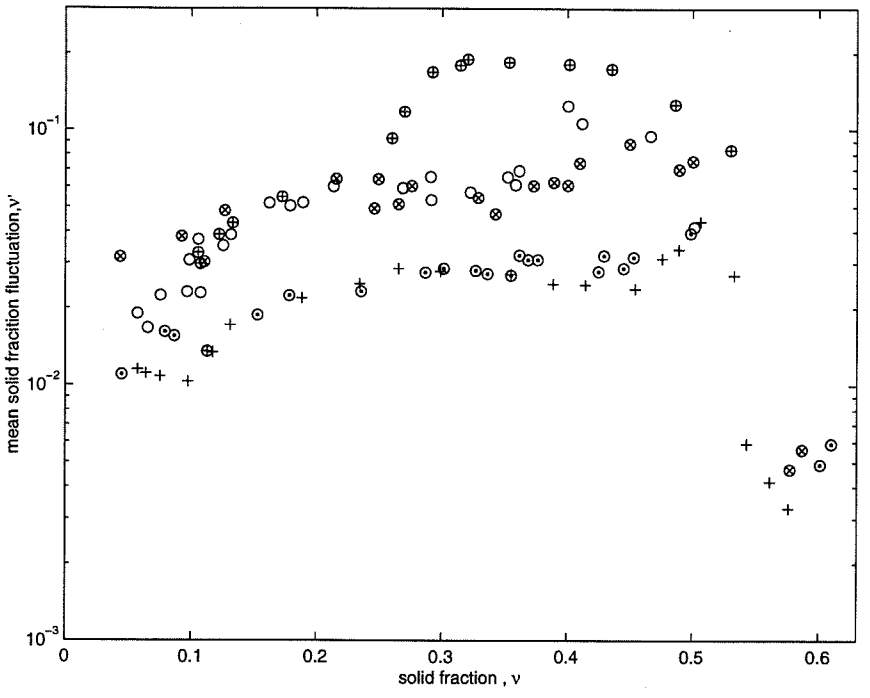

Figure 5.7: Mean solid fraction fluctuation as a function of the solid fraction. Liquid fluidized particles in a 5.08 cm test section: 3 mm glass particles (+), 6 mm glass particles (o), 4.5 mm steel particles ($\oplus$), 6.35 mm nylon particles ($\otimes$), and 3.41 mm PVC cylinders ($\odot$).

tures the agitation and the collision frequency decreases, due to the small number of particles. The same behavior was found for all of the particles tested. The magnitude of the mean fluctuation appears to be larger for particles of larger diameter, with the exception of the 4.5 mm steel particles.

To study the effects of the diameter of the test section on the mean solid fraction fluctuation, tests were performed in two distinct test sections for the same particles. Figure 5.8 shows comparisons of the measurements for 3 mm glass particles in a 5.08 cm and a 10.16 cm diameter test sections. Clearly, the results show that the larger test section has no effect on the magnitude of the mean solid fraction fluctuations, at least for this particular case.

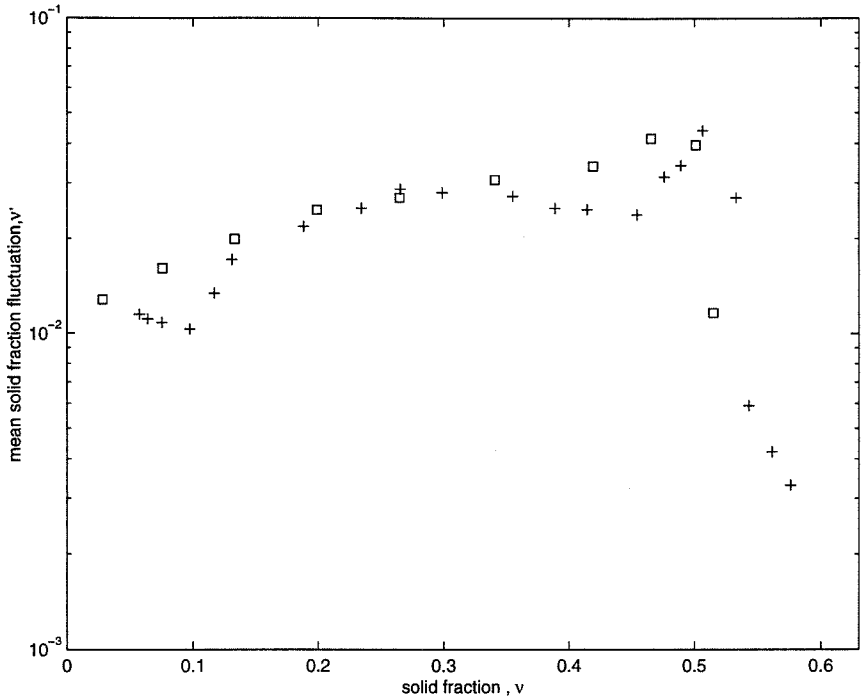

Figure 5.8: Mean solid fraction fluctuation as a function of the solid fraction. Liquid fluidized 3 mm glass particles in the 5.08 cm (+) and the 10.16 cm (□) test sections.

5.3.2 Vertical gravity driven flow

As described in Chapter 2, the test section can be modified to operate in either a vertical flow or a fluidized bed configuration. This section examines the influence of the flow direction on the magnitude of the solid fraction fluctuations. In contrast with the fluidized bed setup, the net velocity of the solid phase for this set of results is not zero. Since the experiment is gravity driven, the net velocity of the particles is always negative (negative is in the downwards direction). Depending on the valve arrangement in the experiment, the liquid could be allowed to flow in the direction of the particles (cocurrent flow) or in the opposite direction (countercurrent flow).

The total weight of the particles was measured before placing them in the upper bin of the test section (see figure 2.2) prior to an experimental run. Therefore, by measuring the total emptying time, an estimate of the velocity of the solid phase, u_s, can be obtained. The solid fraction is measured with the same set of IVFMs.

Figure 5.9 shows the measured solid fraction fluctuations as a function of the

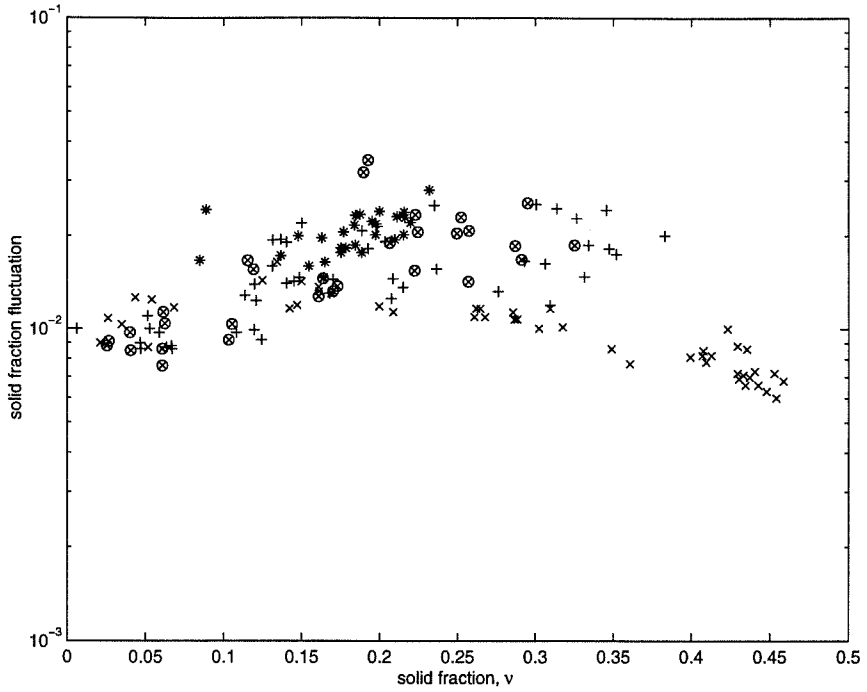

Figure 5.9: Mean solid fraction fluctuation as a function of the solid fraction. Vertical flow of 3 mm glass particles in both test sections. $\times$ cocurrent flow in 5.08 cm TS, $*$ countercurrent flow in 5.08 cm TS. $\otimes$ cocurrent flow in 10.2 cm TS, $+$ countercurrent flow in 10.2 cm TS.

solid fraction for the two test sections and for cocurrent flow and countercurrent flow. The data for all the experimental sets appears to have a maximum at approximately 25% of solid fraction. For most concentrations the mean fluctuation is larger for countercurrent flows. The measurements of the cocurrent flow in the 5.08 cm test section appear to have the smallest value of mean fluctuation.

To analyze the influence of direction of the fluid flow on the fluctuations, the results can be presented as a function of the fluid velocity. The mean fluid velocity could be calculated using the generalized version of the Richardson-Zaki relationship (equation 2.16; Kwauk, 1963). The velocity of the fluid is

$$u_f = u_t(1-\nu)^{n-1} + u_p \tag{5.5}$$

where u_t is the terminal velocity of the particles, n is the experimentally determined exponent in the Richardson-Zaki relation ($n = 2.4$ for this case), and u_p is the mean

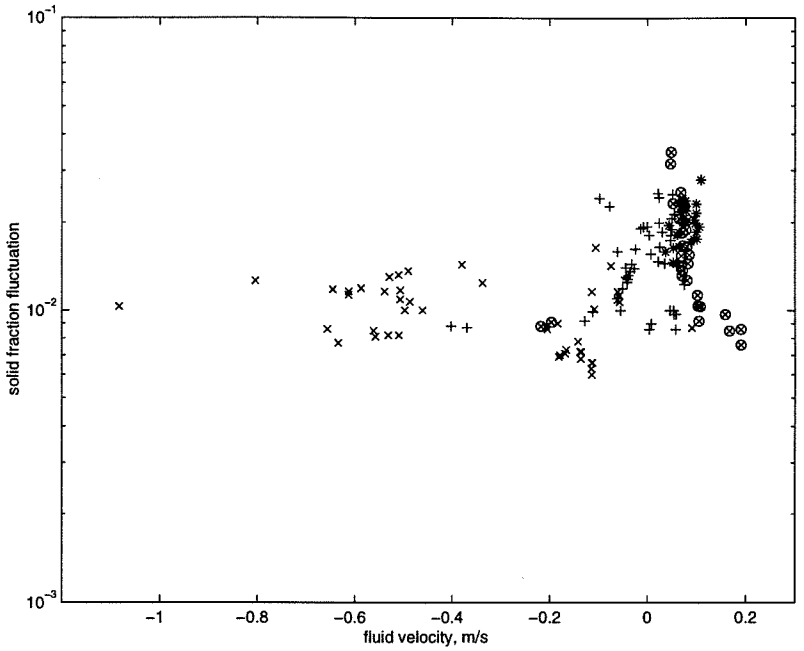

Figure 5.10: Mean solid fraction fluctuation as a function of the fluid velocity. $\times$ cocurrent flow in 5.1 cm TS, $*$ countercurrent flow in 5.1 cm TS. $\otimes$ cocurrent flow in 10.2 cm TS, $+$ countercurrent flow in 10.2 cm TS.

velocity of the particles. Figure 5.10 shows the solid fraction fluctuations as a function of the calculated fluid velocity. Since the particle motion is always in the downwards direction, a negative fluid velocity implies that the fluid is moving cocurrent with the particles. Clearly, the amount of fluctuation is larger for countercurrent flows. countercurrent flows are expected to behave similarly to a fluidized bed. This 'moving' fluidized bed is expected to experience large fluctuations. It should be noted that the fluid velocity was calculated using an empirical relation; the absolute values obtained from it are of uncertain accuracy.

5.4 Low and high frequency fluctuations

Figures 5.3 to 5.6 clearly show the two types of fluctuations. Low frequency waves can be considered a global phenomena of the particle ensemble, while high frequency fluctuations can be related to local variations of the particle-scale hydrodynamics. To study each one of these contributions to the total mean solid fraction fluctuation, a

digital filtering analysis is performed.

To eliminate the low frequency component from the solid fraction signals, a high-pass filtering algorithm is applied to the time-dependent traces. The digital filter models a high pass 4^{th} order Butterworth filter. A cut-off frequency of 3 Hz was chosen by examining the frequency-transformed signals. Figure 5.11 shows the effect of the filter on the volume fraction signals obtained for the 3 mm glass particles in a fluidized bed. On the left the original time signal is shown, and on the right the signal after the filtering. The low-frequency events appear to be completely eliminated. The low concentration case appears not to be strongly affected by the filtering algorithm.

Figure 5.12 shows the effect of the filter on the magnitude of the calculated mean solid fraction fluctuation, for the case of 3 mm glass fluidized particles. The magnitude of the mean solid fraction fluctuation decreases as a result of the filtering. The maximum that was observed at high concentrations disappears after the filtering. The measurements preserve the presence of a maximum at a concentration of approximately 30%.

The filtering algorithm was applied to the solid fraction traces of all the other particles tested. The results of the calculated mean solid fraction fluctuation as a function of solids concentrations are shown in figure 5.13. Clearly, the overall magnitude of the mean solid fraction fluctuation for all the cases is reduced by almost an order of magnitude, with the exception of the steel particles. Yet, the appearance of a maximum at approximately 30% of concentration is preserved. The dependence of the mean fluctuation on the particle size observed from the unfiltered data disappears. However, the data for the particles of greater mass appear to have larger fluctuations.

5.5 Comparisons

The model proposed by Buyevich & Kapbasov (equations 5.1 and 5.2) considers only the small scale fluctuations. Since the large scale fluctuations in the measurements can be filtered out, a direct comparison of the measurements and the predictions is possible.

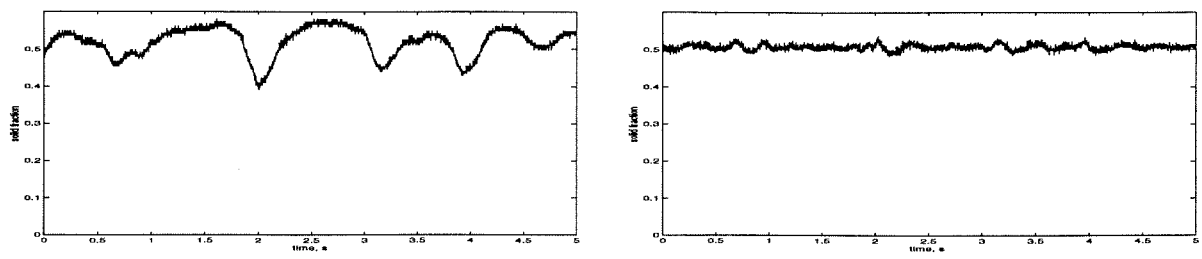

(a) $\overline{\nu} = 0.50$

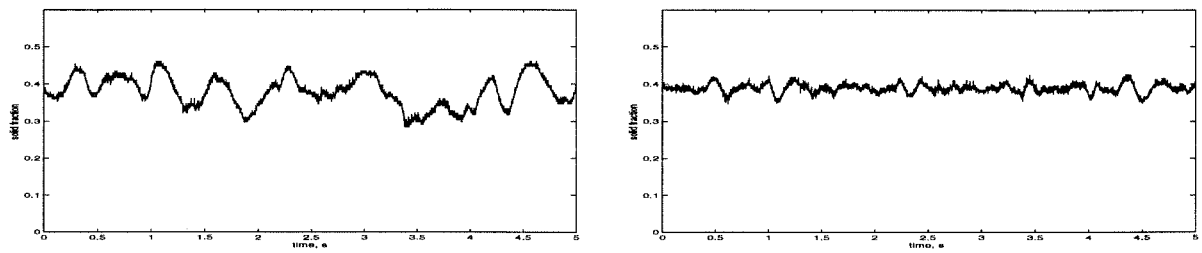

(b) $\overline{\nu} = 0.38$

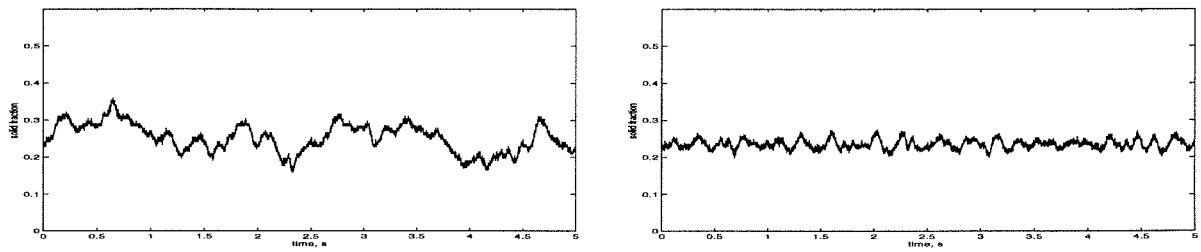

(c) $\overline{\nu} = 0.23$

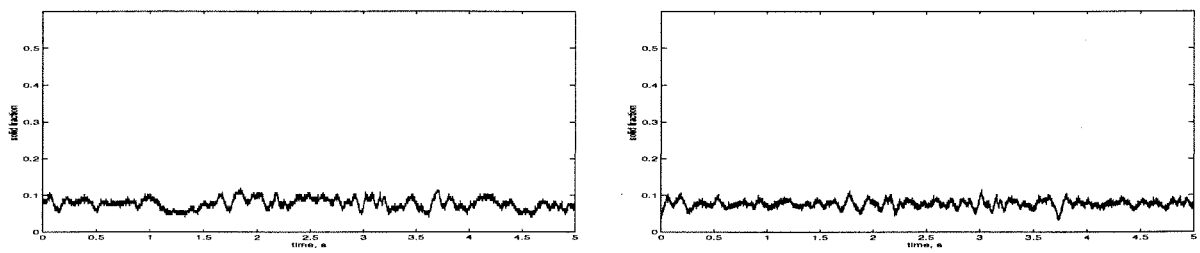

(d) $\overline{\nu} = 0.08$

Figure 5.11: Effect of the filtering. High pass 4^{th} order Butterworth digital filter, with cut-off frequency of 3 Hz. The original signal is shown on the left column, the resulting signal after the filtering. The mean solid fraction added again after filtering.

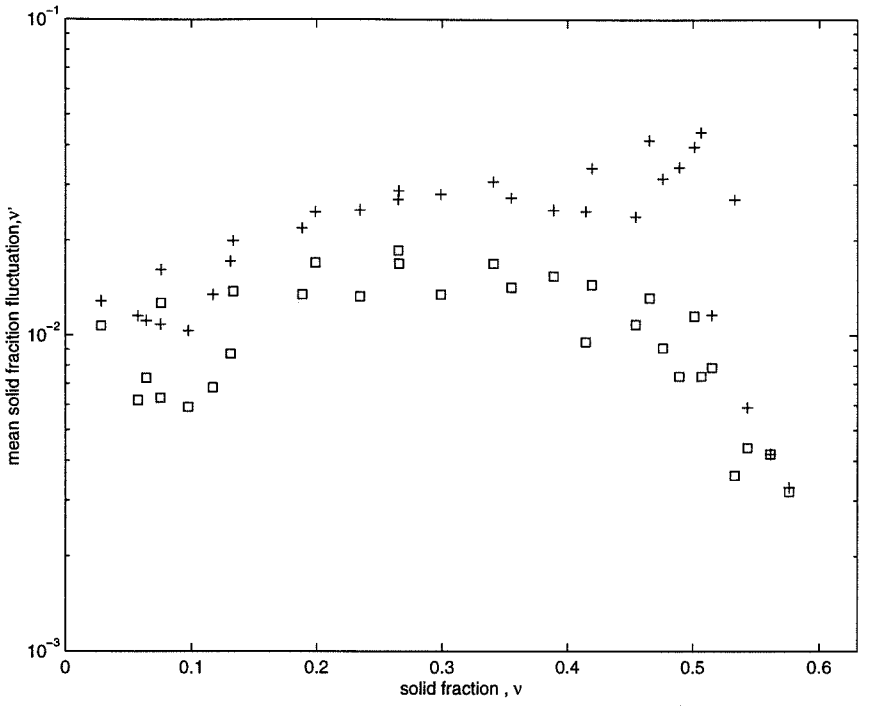

Figure 5.12: Mean solid fraction fluctuation as a function of the solid fraction, before filtering (+) and after high-pass filtering (□). Results for 3 mm glass particles in the 5.08 cm and the 10.16 cm test sections.

In figure 5.13 a direct comparison of the two curves described by equations 5.1 and 5.2 and the experimental measurements are shown. The models appear to predict the shape of the experimental measurements, but the absolute value is over-predicted by a factor of 4 or 5 and almost by an order of magnitude for the case of light particles. Note too, that the predictions do not depend on the particle properties. It is important to mention that these predictions assume that the fluctuations are isotropic, which may not be the case in the experiment. Also, the IVFM gives a cross-section average measurement of the solid fraction rather than a point-wise measurement as used in the models.

5.6 Discussion

By analyzing the non-steady component of the volume fraction signal obtained from the impedance volume fraction meter (IVFM), a measure of the agitation in a liquid-

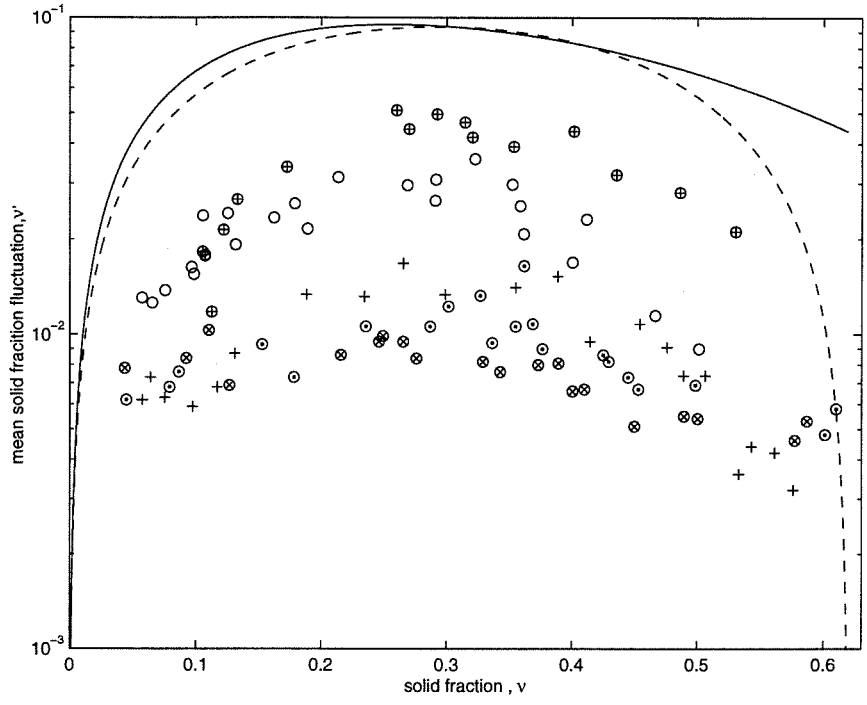

Figure 5.13: Mean solid fraction fluctuation after high pass filtering as a function of the solid fraction. All from a 5.08 cm test section fluidized bed. Compare with the unfiltered measurements in figure 5.7. The lines are the predictions from equation 5.1 (solid line), equation 5.2 (dashed line).

solid flows was obtained. The IVFM measured the cross-sectional average impedance of the mixture that is a measure of the solid concentration of particles due to the difference of impedance between the two phases. The IVFM was powered by a 50 kHz power supply to ensure a high frequency response. Experiments were performed in a liquid fluidized beds for glass, steel and plastic particles, and in a vertical gravity-driven flow for glass particles.

The value of the rms fluctuation was calculated for a wide range of concentrations for all the particles tested. The solid fraction time-dependent signals showed significant changes in the magnitude and in the nature of the fluctuations for different concentrations and particle properties. Two main types of fluctuations were identified: low frequency fluctuations and high frequency fluctuations. The low frequency fluctuations appeared as moving wave-like bands of low concentration. The high frequency fluctuations were more random in nature.

When the rms fluctuation for the fluidized beds was plotted as a function of the mean solid fraction, several regimes were observed. Between the closed packed state and 40% solid fraction, the low frequency fluctuations dominated. A maximum was observed at approximately 50% of solids concentration. The low-frequency traveling bands of low density were the main contribution for the appearance of a maximum rms fluctuation observed at 50% of concentration. For concentrations smaller than 40% the low frequency fluctuations began to loose coherence and, a higher frequency component began to appear. The rms fluctuation decreased from its maximum value at 50% solid fraction, reached a local minimum at around 40%. For decreasing concentration, the rms fluctuation began to increase again and reached a second local maximum at approximately 30% of concentration. The increase on the value of the rms fluctuation was attributed to the increase of high frequency fluctuations. For concentrations lower than 30% the rms fluctuation decreased steadily until zero concentration.

The different regimes appear to agree with the results obtained by Didwania & Homsy (1981). In their two-dimensional liquid fluidized bed experiments, several flow regimes were identified for decreasing concentrations: wavy flow, wavy flow with

transverse structure, fine-scale turbulent flow, and bubbling state. The wavy flow regime can be identified from the minimum fluidization state until 50% of solid fraction, at which the maximum rms fluctuation occurred. From 50% to 40% of mean solid fraction, the low-concentration bands began to loose coherence, which could be associated with the regime named wavy flow with transverse structure. The increase of high frequency fluctuations for solid fraction in the 30-40% range, indicate a turbulent-like behavior in accordance with the fine-scale turbulence regime. The further reduction of the rms fluctuation for concentrations smaller than 30% can be associated with the last regime, the bubbling state. The values of concentration at which the flow transitions occur in the present experiments are close, but not exactly the same, to those reported by Didwania & Homsy. The difference can be attributed to the differences in experimental setups (2-D vs 3-D) and particle used.

The results obtained for different particle sizes and densities were compared. The rms fluctuation appeared to be higher for larger particles. For the same concentration, fluidized beds with larger diameter particles had a higher value of the rms fluctuation. The only exception were the 4.5 mm steel particles, which showed the highest value of rms fluctuation for all concentrations.

To study the influence of the container dimensions on the rms fluctuations, tests were performed in two different test sections. The results obtained for glass particles showed that there was no significant influence of the test section diameter on the measured value of the rms fluctuation.

Similar measurement were performed in a vertical gravity-driven flow. Both cocurrent and countercurrent flows were studied. The same type of behavior was encountered in these flows. The flows in countercurrent configuration showed higher values of the rms fluctuation. Since flows of concentrations higher than 40% were not possible to achieve with the present experimental setup, the maximum rms value observed in highly concentrated fluidized beds was not observed in the vertical flows.

To investigate the contribution of each of the two types of fluctuations (low and high frequency) to the total rms fluctuation, a high-pass filter was applied to the time-dependent solid fraction signals. The low frequency fluctuations were filtered

out using a 4th order Butterworth digital filter with a cut-off frequency of 3 Hz. The rms fluctuation was recalculated using the filtered traces.

The recalculated value of the rms fluctuation was smaller than the original one for all solid fractions. The maximum rms fluctuation observed at 50% of solid fraction disappeared completely. The other local maximum observed at approximately 30% remained unchanged. As suspected, this result indicated that the first maximum was a result of the low-frequency fluctuations and the second maximum was produced by the high-frequency fluctuations. It is important to note that the recalculated rms fluctuation appeared to scale with particle mass rather than particle size (as seen in the un-filtered rms fluctuations). For a given solid fraction, the fluidized beds with more massive particles appeared to have higher values of the filtered rms fluctuation.

Since the effect of the high-frequency fluctuations was isolated from the total fluctuation, it was appropriate to perform a direct comparison with the model proposed by Buyevich & Kapbasov (1994). The model, in its two variations, predicted the trend of the rms fluctuation as a function of the mean solid fraction correctly; however, the magnitude of the rms fluctuation was overestimated by an order of magnitude. In their model, an isotropic state of solid fraction fluctuations was assumed. In the experiments performed in the present setup, the fluctuations were not isotropic. Also, the model predicts values of the point-wise rms fluctuation, but the measurements obtained were cross-sectional averages of the solid fraction. These differences may have led to some of the discrepancies encountered in the comparison. The model also failed to predict the dependence of the rms fluctuation on particle properties.

Chapter 6 Conclusions

6.1 Summary of results

The collisional particle pressure was measured for a vertical gravity-driven liquid-solid flow and for a liquid fluidized bed. The measurement of this property represents the first of its kind in the field of multi-phase flows. No other similar measurement has been found in the literature. Theoretical studies of liquid-solid flows often make reference to the particle pressure, and up until now it was not possible to verify the validity of the assumptions made in the construction of the models.

For concentrated mixtures the measured value of the particle pressure was small, due the limited mobility of the particles in a packed state. On the other extreme, in dilute mixtures the particles move freely and collide against the transducer at higher velocities; however, the occurrence of such collisions is more sporadic resulting in a low value of the particle pressure. The combination of these two competing mechanisms gives rise to a maximum value of the particle pressure at some intermediate solid fraction, normally at approximately 30% of solid fraction. Similar results were obtained for all the particles and test sections employed. The trends described were observed more clearly for the case of fluidized beds. The magnitude of the measured particle pressure was found to scale with $\rho_p u_t^2$, where ρ_p and u_t are the density and the terminal velocity of the particles respectively. However, the results of the normalization show that other parameters might influence the particle pressure, such as density ratio of the phases and the particle Reynolds number. The diameter of the test section was found not to have a significant influence on the results obtained. When the particle pressure was measured in a vertical flow configuration, the direction of the fluid phase did not produce a significant effect on the particle pressure.

A review of some of the existing studies that model the particle pressure was presented. Essential differences were found in the formulation of some of these models.

Some models predicted the particle pressure in a *ad hoc* manner, due to a complete lack of evidence or physical understanding of the phenomena. Other models borrow ideas from dry granular flows, with corrections to include the effects of the interstitial fluid. A direct comparison between the experiments and the existing models showed the significant differences between the various models and the experimental measurements. Future theories may rely on the physical insight provided by these measurements to construct descriptions that are closer to the true behavior of liquid-solid mixtures.

Probability density functions were constructed for the maximum pressure, collision duration and collision impulse. In concentrated flows low pressure and low impulse collisions were found to occur more frequently. As the solid fraction decreases it was observed that the probability of occurrence of higher impulse collisions increased. The analysis of the probability density function of the duration of collisions lead to the discovery of two distinct contributions to the particle pressure. Pressure pulses of two distinct durations were found in the PDF of collision duration. With the help of a visualization system, the two contributions to the particle pressure were identified and explained. By synchronizing a high-speed digital camera with the acquisition system of the pressure transducer, the pressure pulses could be correlated with the moving particles in the test section. The long-duration collisions were found to be the result of direct impacts of particles against the surface of the transducer. The short duration pulses were found to be pressure pulses generated by collisions of particles in the vicinity of the pressure transducer. The acceleration of the fluid caused by a colliding particle produced a pulse that was transmitted from the surface of the particle to the transducer through the fluid. The direct contribution was found to be the most significant contribution to the particle pressure. The existence of the 'radiated' contribution to the particle pressure had not been previously recognized.

A series of experiments was performed to further investigate the nature of the two types of pressure pulses. To generate collisions in a controlled environment, an immersed pendulum experiment was built. Controlled repeatable collisions were produced by letting a particle swing freely towards a wall, where a pressure transducer

was flush-mounted. The motion of the particles was recorded using a high speed digital camera that was synchronized with the pressure transducer acquisition system. In this way, the velocity and collision pressure could be measured and correlated. Various particle sizes and densities were employed. Measurements of the collision impulse as a function of the impact velocity were obtained and compared with the Hertzian theory of contact. Moments before contact the particles experience a significant deceleration resulting from the liquid pressure build up in the gap between the particle and the wall. The motion of the impacting particles was found to be influenced by the wall only at very small distances before contact. The coefficient of restitution was measured, and found to decrease significantly for low values of approach velocity. By comparing the measured immersed pressure impulses with those predicted by the Hertzian theory, a quantification of the effects of the fluid was obtained that indicated that the difference between the predicted Hertzian impulse and the measurement increased as the impact velocity decreased. By calculating the pressure impulses instead of the maximum pressures, the values of the elastic properties of the particles and the transducer were not needed. The measurements of the pressure impulses and the comparison with Hertzian theory had not been performed in the past for immersed collisions. The proposed pendulum experimental setup was an inexpensive, versatile and reliable way to study particle collisions.

A model to predict the particle deceleration before impact due to the fluid was proposed. The model was based on a control volume approach to predict the pressure distribution in the gap from the mass and momentum fluxes. The results obtained appear to agree well when compared with the experimental measurements.

To study the nature of the second contribution to the particle pressure the pendulum experiment was modified to operate as dual pendulum to produce binary collisions of particles. Two particles of the same diameter and density were suspended from strings and aligned. One particle, the target particle, was suspended at rest at a certain distance from the wall, where a high-frequency response pressure transducer was mounted. The second particle, the impact particle, was released from rest at some initial angle. The impact particle accelerated towards the target particle and

produced a collision. The impulsive acceleration of the target particle produced a pressure front in the liquid that was transmitted from the surface of the particle to the transducer. Tests were performed for a number of different particle densities and diameters. The measured impulse pressure was found to scale with the diameter of the particle, the density of the fluid and the velocity of impact. The magnitude of the pulses was found to decrease for increasing distances from the wall. A model based on the impulse pressure theory was proposed. The impulsive acceleration of a particle near a wall is modeled as a pair of impulse-doublets in an inviscid flow. The comparison between the experiments and the model showed good agreement. The study of the fluid pressure generated by particle collisions is new in the field of multi-phase flow. In the work presented in this thesis, the contribution of collision-generated fluid pressure pulses was recognized and modeled successfully.

To further investigate the nature of the generating mechanisms of the random motions in solid-liquid flows and of the particle pressure, the fluctuating component of the particle concentration was measured. Using a high-frequency response impedance volume fraction meter, the instantaneous cross-sectional volume fraction was measured. The volume fraction meter was flush mounted in the test section of a fluidized bed and a vertical flow. The rms fluctuation was measured for different particle sizes and densities for the entire range of concentrations. Two different diameter test sections were used. For the case of fluidized beds, the rms fluctuation was found to have two local maxima when plotted as a function of the solid fraction. The first maximum occurred at concentrated mixtures and was attributed to the effect of large-scale fluctuations. The other maximum appeared at intermediate concentrations and was a result of the small-scale fluctuations. The diameter of the test section was found to have little effect on the mean value of the fluctuation. The tests performed in a vertical gravity driven flow showed that a maximum mean fluctuation at large concentrations did not appear. When the liquid flow was counter-current with the particles, the amount of fluctuation was larger. Since two types of fluctuations were observed, an analysis of their contributions to the total fluctuation was performed. By high-pass filtering the time signals the large scale fluctuations were eliminated and the

fluctuation recalculated. The maximum attributed to the large-scale fluctuations was completely eliminated for the filtered data. A comparison of the measurements with a model found in the literature was performed. Although the model predicted the right trend in the rms fluctuations as a function of concentration, it over-predicted its magnitude by an order of magnitude. An order of magnitude analysis was performed to obtain a correlation between the value of the mean solid fraction fluctuation and the mean solid velocity fluctuation. The analysis showed that the mean solid velocity fluctuation is proportional to the mean solid fraction fluctuation.

6.2 Comments on general issues

The main objective of the investigation presented in this thesis is to shed some light to the basic phenomena that govern the behavior of liquid-solid mixtures. The approach followed was to perform simple experiments at a particle size level to help understand the principles that contribute to the complex behavior associated with multi-component flows.

The measurement of the particle pressure could have important implications in the development of future models of liquid-solid mixtures. The results may also be of interest for more practical applications, since the particle pressure could be associated with topics such as mixing, erosion, mass and heat transfer. The mechanics of particle-particle and particle-wall interactions investigated in this work serve as building blocks for theoretical models or computer simulations. The measurement of the fluctuating component of the concentration and velocity could help researchers understand the changes observed in the global behavior of these mixtures.

Many issues remain to be resolved. Although the particle pressure was found to scale with $\rho_f u_i^2$, the particle Reynolds number and the density ratio of the phases appeared to influence the results. A more in depth investigation of these effects remains to be performed.

A significant amount of variance was associated with the results obtained for individual particle-wall and particle-particle collisions. Extreme care was taken to

ensure that the experiments were performed under controlled conditions. Yet, results for the same nominal parameters were found to vary, in some cases, by a factor of 2 or 3. The influence of the surface roughness and liquid properties remain to be explored. Although physical contact appeared to occur when the surfaces collided, it is still unknown whether the fluid is completely drained from the gap. The mechanics of rebound were found to be dominated not only by the flow in the gap but rather by the entire flow field around the sphere. A better model for immersed particle collisions should include the influence of the fluid flow field around the particle. Inclined and non-normal immersed collisions remain to be explored.

The relation between the solid fraction fluctuations and the fluctuations in the solid and liquid phases could be further investigated. However, simultaneous velocimetry of both phases appears as a great challenge for experimentalists.

The measurement techniques and instrumentation used in this thesis for the study of liquid fluidized beds and vertical flows could be used to study other flow geometries and, with the pertinent modifications, other particle flow regimes could be studied.

Bibliography

ABU-ZAID, S. AND AHMADI, G. 1995 A thermodynamically consistent rate-dependent model for turbulent two-phase flows. *Int. J. Non-Linear Mechanics*, **30**, 509–529.

AHMADI, G. 1987 On the mechanics of incompressible multiphase suspensions. *Adv.Water Res.*, **10**, 32–43.

AHMADI, G. AND MA, D. 1990 A thermodynamic formulation for dispersed multiphase turbulent flows - I. basic theory. *Int.J.Multiphase Flow*, **16**, 323–340.

AVALONE, E.A. & BAUMEISTER III, T. 1896 *Mark's Standard Handbook for Mechanical Engineers* New York, McGraw-Hill, 9th ed.

BAGNOLD, R.A. 1954 Experiments on a gravity-free dispersion of large spheres in a Newtonian fluid under shear. *Proc.Roy.Soc.*, **225**, 49–63.

BALLAMUDI, R.K., KOOPMAN, D.C., MANIAS, E. AND BITSANIS, I.A. 1994 Crystallization at solid-liquid interfaces. *Abs.Pap.ACS*, **207 (2)**, 192.

BARNOCKY, G. AND DAVIS, R.H., 1988 Elastohydrodynamic collision and rebound of spheres: Experimental verification. *Phys.Fluids*, **31** (6), 1324–1329.

BATCHELOR, G.K. 1967 *An Introduction to Fluid Dynamics* Cambridge University Press, Cambridge, U.K.

BATCHELOR, G.K. 1988 A new theory of the instability of a uniform fluidized bed. *J.Fluid Mech.*, **193**, 75–110.

BEN-AMMAR, F., KAVIANY, M. & BARBER, J.R. 1992 Heat transfer during impact. *Int.J.Heat Mass Transfer*, **35**,1495–1506.

BERNIER, R.N., 1982 Unsteady two-phase flow instrumentation and measurement. PhD thesis, California Institute of Technology, Pasadena, California.

BULTHUIS, H.F., PROSPERETTI, A. & SANGANI, A.S. 1995 'Particle stress' in disperse two-phase potential flow. *J.Fluid Mech.*, **294**, 1–16.

BUYEVICH, Y.A. & KAPBASOV, S.K. 1994 Random fluctuations in a fluidized bed. *Chem.Eng.Sc.*, **49**, 1229–1243.

CAMPBELL, C.S. 1990 Rapid granular flows. *Annu. Rev. Fluid Mech.*, **22**, 57–92.

CAMPBELL, C.S. AND WANG, D.G. 1990 Particle pressures in gas-fluidized beds. *J.Fluid Mech.*, **227**, 495–508.

CHAPMAN, S. 1939 *The mathematical theory of non-uniform gases.* Cambridge University Press, Cambridge, U.K.

CLIFT, R., GRACE, J.R., & WEBER, M.E. 1978, *Bubbles, Drops and Particles.* Academic Press, London.

COOKER, M.J. AND PEREGRINE, D.H. 1995 Pressure-impulse theory for liquid impact problems. *J.Fluid Mech.*, **297**, 193–214.

COUDERC, J.P. 1985 Incipient fludization and particulate systems. In *Fluidization* (ed. J. Davidson, R. Clift, and D. Harrison), London, Academic Press, second edition.

DAVIS, R.H., SERAYSSOL, J.M. & HINCH, E.J. 1986 The elastohydrodynamic collision of two spheres. *J.Fluid Mech.*, **163**, 479–497.

DIDWANIA, A.K., & HOMSY, G.M. 1981 Flow regimes and flow transitions in liquid fluidized beds. *Int. J. Multiphase Flow*, **7**, 563–580.

DI FELICE, R. 1995 Hydrodynamics of liquid fluidization. *Chem. Engng. Sc.*, **50**, 1213–1245.

FOSCOLO, P.U., DI FELICE, R. & GIBILARO, L.G. 1989 The pressure field in an unsteady-state fluidized bed, *AICHE Journal*, **35**, 1921–1926.

FOSCOLO, P.U. & GIBILARO, L.G. 1987 Fluid dynamic stability of fluidized suspensions. *Chem.Eng.Sci.*, **39**, 1485–1500.

GOLDSMITH, W. 1960 *The theory and physical behavior of colliding solids* London, Edward Arnold Publishers LTD.

HAPPEL, J. & BRENNER, H. 1965 *Low Reynolds Number Hydrodynamics* Prentice-Hall, New York.

HARRISON, D., DAVIDSON, J.F. & DEKOCK, J.W. 1961 On the nature of aggregative and particulate fluidization. *Trans. Instn. Chem. Engrs*, **41**, 13.

HESTRONI, G. 1989 Particles turbulence interaction. *Int.J.Multiphase Flow*, **15**, 735–746.

HOCKING, L.M. 1973 The effect of slip on the motion of a sphere close to a wall and of two adjacent spheres. *J.Eng.Math.*, **7**, 207–221.

HWANG G.J. & SHEN H.H. 1993 Fluctuation energy eqautions for turbulent fluid-solid flows. *Int.J.Multiphase Flow*, **19**, 887–895.

ISHII, M. 1975 Thermo fluid dynamic of two-phase flow. In Scientific and Medical Publications of France. Eyrolles, Paris.

JACKSON, R. 1963 The mechanics of fluidized beds: Part I: the stability of the state of uniform fluidization. *Trans.Inst.Chem.Eng.*, **41**, 13–41.

JACKSON, R. 1985 Hydrodynamic stability of fluid-particle systems. In *Fluidization* (ed. J. Davidson, R. Clift, and D. Harrison), London, Academic Press, second edition.

JIN, C. 1996 Generic stability model and experimental study of liquid-fluidized beds. PhD thesis. University of Southern California, Los Angeles California.

JOHNSON, J.K. 1987 *Contact Mechanics*, Cambridge University Press, Cambridge, U.K.

KEENING, V.M. 1997 Self-induced turbulence in solid-liquid flow PhD thesis. Washington State University, Pullman Washington.

KOCH, D.L. 1990 Kinetic theory for a monodisperse gas-solid suspension. *Phys. Fluids A*, **2**, 1711–1723.

KYTÖMAA, H.K. 1987 Study of the structure in multicomponent flows. PhD Thesis, California Institute of Technology, Pasadena California.

KYTÖMAA, H.K. & BRENNEN, C.E. 1986 Some observations of flow patterns and statistical properties of three component flows. *J.Fluids. Eng.*, **110**, 76–84.

KYTÖMAA, H.K. & SCHMID, P.J. 1992 On the collision of rigid spheres in a weakly compressible fluid *Phys.Fluids A*, **4** (12).

KUMAR, S., HART, D.P. & BRENNEN, C.E. 1990 Granular pressure measurement in fluidized beds. In *ASME Cavitation and Multiphase Flow Forum*, Toronto, Canada.

KWAUK, M. 1965 Generalized fluidization, Part I: Steady state motion. *Scientia Sinica*, **12**, 587–612

LAMB,H., SIR 1945 *Hydrodynamics* New York, Dover Publications.

LANDWEBER, L. & SHAHSHAHAN, A. 1992 Added masses and forces on two bodies approaching central impact in an inviscid fluid. J.SHIP RES., **36**, 99–122.

LIAN, G., ADAMS,M.J. & THORNTON, C. 1996 Elastohydrodynamic collision of spheres. *J.Fluid Mech.*, **311**, 141–152.

LIU, C.H., NAGEL, S.R., SCHECTER,D.A., COPPERSMITH, S.N., MUJUMDAR, S., NARAYAN, O. & WITTEN, T.A. 1995 Force fluctuations in bead packs. *Science*, **269**, 513–515.

LUNDBERG, J. & SHEN, H.H. 1992 Collisional restitution dependence on viscosity. *J.Eng.Mech.*, **118**, 979–989.

MCLAUGHLIN, M.H. 1968 An experimental study of particle-wall collision relating of flow of solid particles in a fluid. *Engineer Degree Thesis*, California Institute of Technology, Pasadena California.

MEI, R. 1994 Flow due to an oscillating sphere and an expression for the unsteady drag on the sphere at finite Reynolds number, *J.Fluid Mech.*, **270**, 133-174.

MILNE-THOMPSON,L.M. 1950 *Theoretical Hydrodynamics* Macmillan Co., New York.

NEDDERMAN, R.M. 1992 *Statics and Kinematics of Granular Materials* Cambridge University Press.

NEEDHAM, D.J. & MERKIN, J.H. 1983 The propagation of a voidage disturbance in a uniformly fluidized bed. *J.Fluid Mech.*, **131**, 427–454.

NOTT, P.R. & BRADY, J.F. 1994 Pressure-driven flow of suspensions: simulations and theory. *J.Fluid Mech.*, **275**, 157–199.

PROSPERETTI, A. & JONES, A.V. 1984 Pressure forces in disperse two-phase flow. *Int.J.Multiphase Flow*, **10**, 425–440.

ROCO, M.C. AND ADDIE, G.R. 1987 Erosion wear in slurry pumps and pipes. *Powder Technol.*, **50**, 35–46.

SANGANI, A.S., MO, G., TSAO, H.K. & KOCH, D.L. 1996 Simple shear flows of dense gas-solid suspensions at finite Stokes numbers. *J.Fluid Mech.*, **313**, 309–341.

SUNDARARAJAKUMAR, R.R. & KOCH, D.L. 1996 Non-continuum lubrication flows between particles colliding in a gas. *J.Fluid Mech.*, **313**, 283–308.

TSAO, H.K. & KOCH, D.L. 1995 Simple shear flows of dilute gas-solid suspensions. *J.Fluid Mech.*, **296**, 211–245.

TÜZÜN, U. AND WALTON, O.R. 1992 Micromechanical modeling of load-dependent friction in contacts of elastic spheres. *J.Phys.D.*, **25**, A44–A52.

WALLIS, G.B. 1969 *One-dimensional two phase flow.* New York, McGraw-Hill Book Company.

ZENIT, R. & HUNT, M.L. 1997 Influence of fluid properties on submerged collision of particles. In *ASME International Symposium of Liquid-Solid Flows*, Vancouver, Canada.

ZENIT, R., HUNT, M.L. & BRENNEN, C.E. 1997 Collisional particle pressure measurements in solid-liquid flows. To appear *J.Fluid Mech.*

ZHANG, D.Z. & PROSPERETTI, A. 1994 Averaged equations for inviscid disperse two-phase flow. *J.Fluid Mech.*, **267**, 185–219.

Appendix A: Discussion on the reverberations of the pressure pulses

During the measurements of the particle pressure (Chapter 2) a certain amount of reverberation was observed to occur after a pressure pulse was captured. In the traces obtained for the measurement of direct collisions in Chapter 3, the reverberations were also present. This oscillating pressure was observed also for the case in which the pressure pulses are transmitted through the liquid (Chapter 4). The reason for this has been attributed to the dynamics of the membrane after the collision, but their exact description is not clear. It is important to note that these reverberation are not observed in dry collisions.

Direct collisions

Figure A.1 shows two typical cases of a 6 mm glass particle colliding directly against the pressure transducer for two different impact velocities. On the left the pressure-time signal is shown, and on the right the frequency-transformed data is shown. Note that in this case the amount of reverberation appears to be larger for a larger collision impulse. Figure A.2 shows two typical pressure pulses for a direct collision of a 4.5 mm steel particle. A secondary reverberation can be observed in the pulse for the highest value of collision impulse.

Indirect collisions

The same type of reverberance was found in the liquid pressure front experiments. In these experiments the particles do not contact the transducer and yet the reverberance is still observed. Figure A.3 shows two typical pressure pulses resulting from the binary collision of a pair of 6 mm glass particles, and figure A.4 shows the case of 4.5 mm steel particles. Although the steel particles collided at higher velocities, the amount of reverberation was found to be larger for the 6 mm glass case.

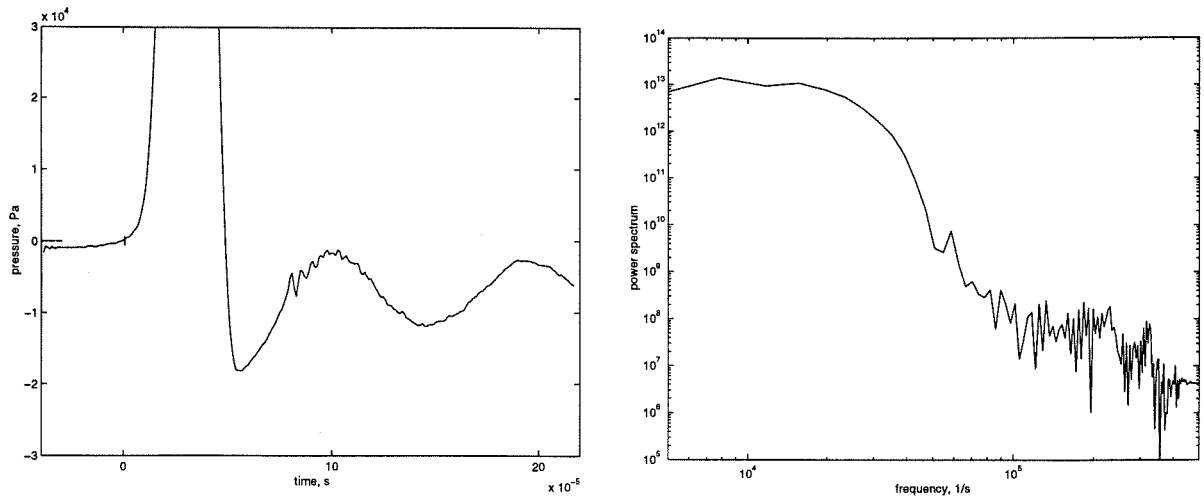

(a) u_i= 129 mm/s, I=3.61 Pa.s

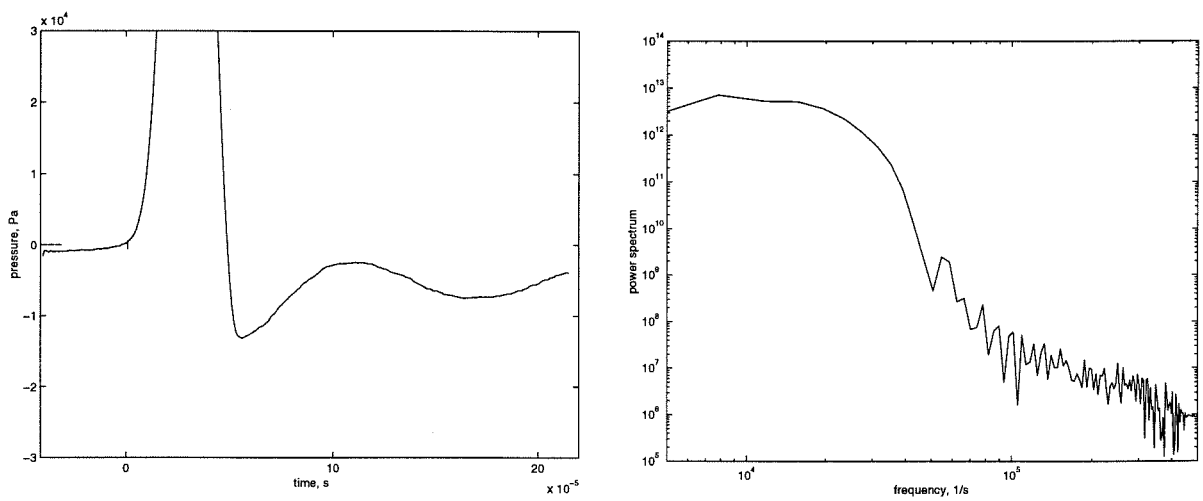

(b) u_i=94 mm/s, I=2.58 Pa.s

Figure A.1: Time and frequency domain pressure traces (left and right columns respectively) for a direct collision of a 6 mm glass particle in water.

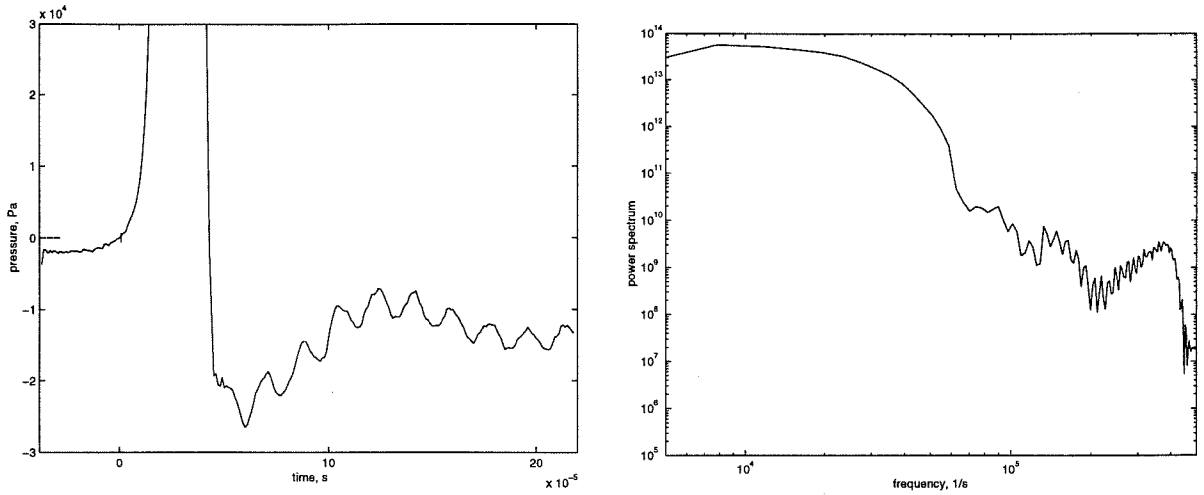

(a) u_i= 224 mm/s, I=7.64 Pa.s

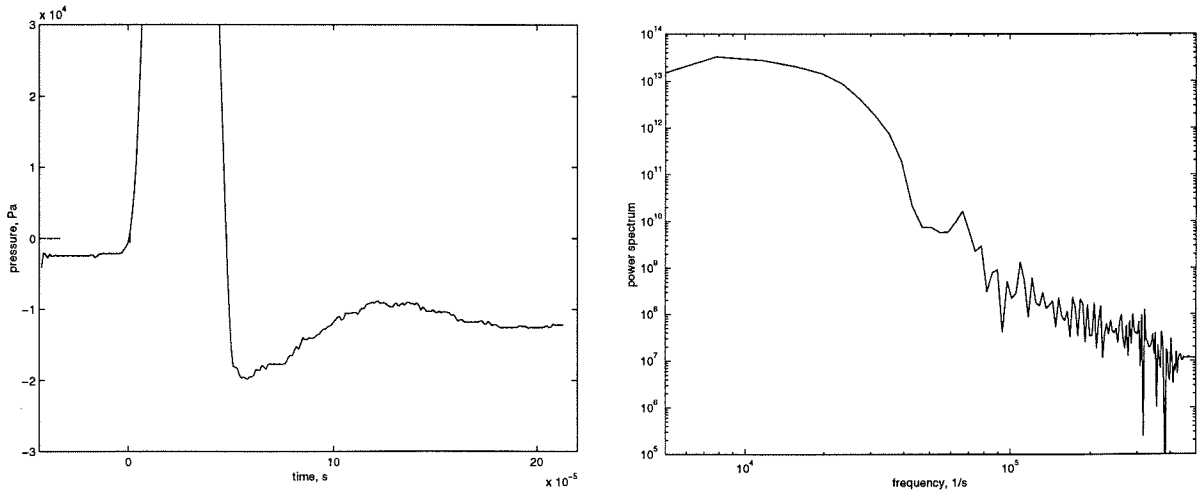

(b) u_i=133 mm/s, I=5.53 Pa.s

Figure A.2: Time and frequency domain pressure traces (left and right columns respectively) for a direct collision of a 4.5 mm steel particle in water.

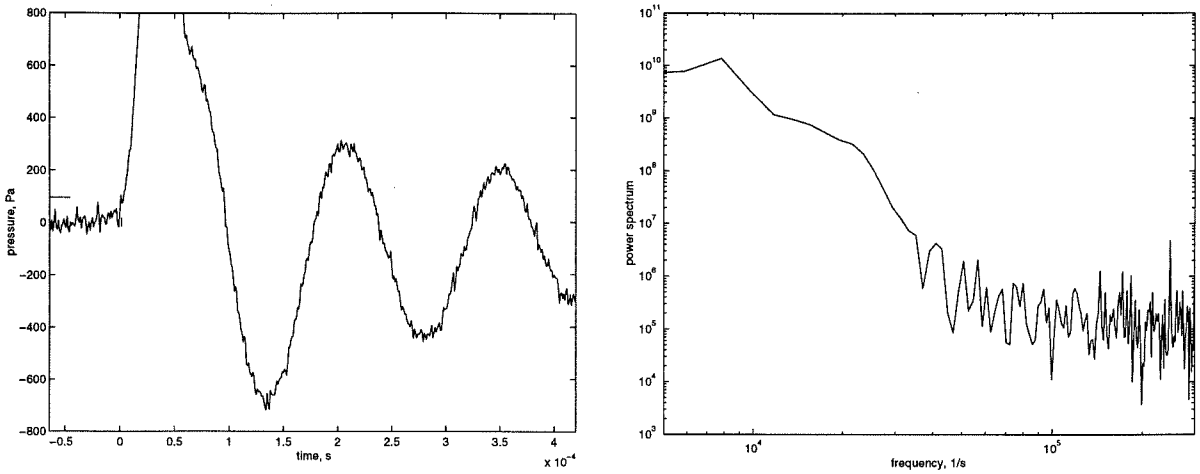

(a) b/d=0.66, u_T= 70 mm/s, I=0.085 Pa.s

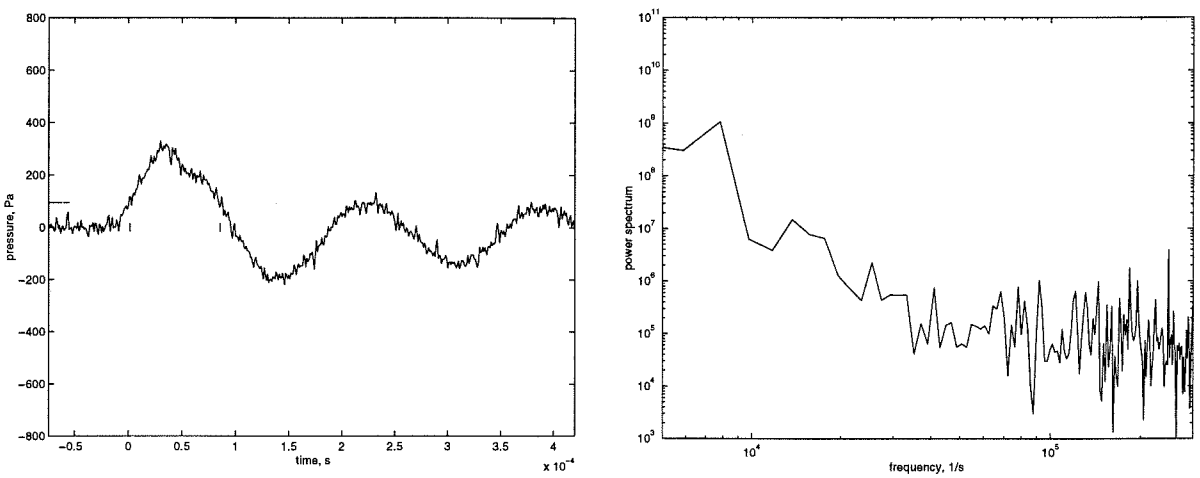

(b) b/d=1.33, u_i=70 mm/s, I=0.018 Pa.s

Figure A.3: Time and frequency domain pressure traces (left and right columns respectively) for a fluid pressure pulse due to a collision of two 6 mm glass particles in water.

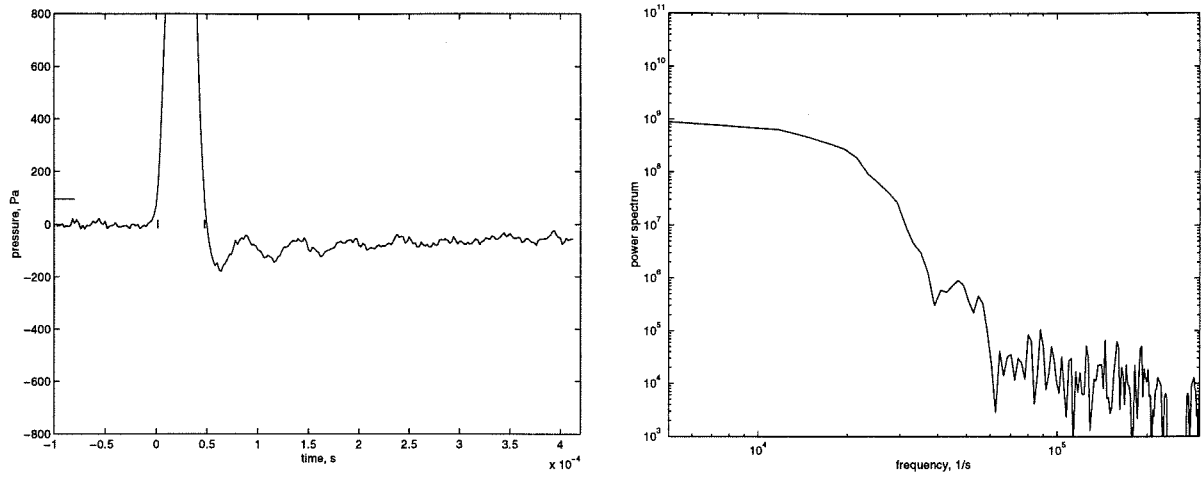

(a) b/d=0.66, u_τ= 93 mm/s, I=0.061 Pa.s

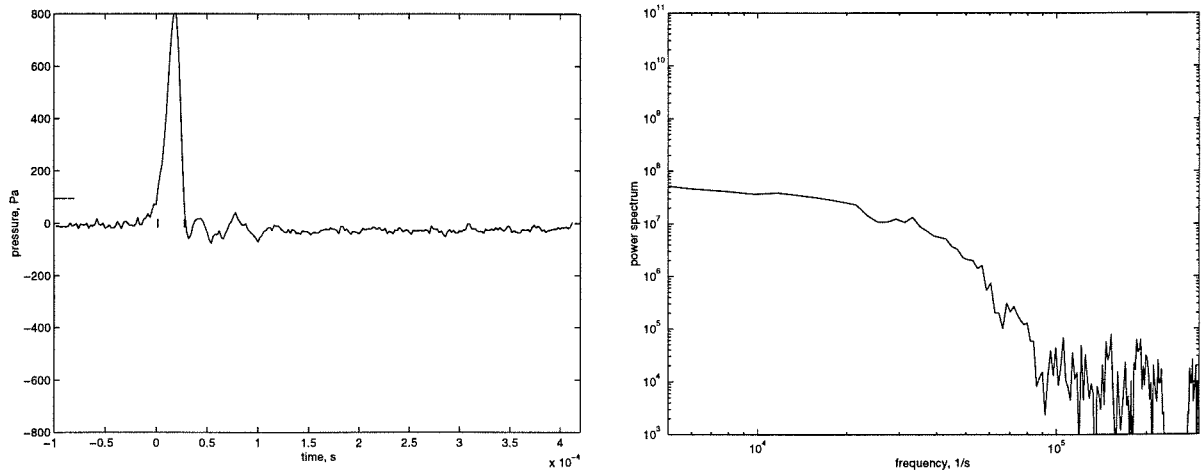

(b) b/d=1.33, u_i=93 mm/s, I=0.013 Pa.s

Figure A.4: Time and frequency domain pressure traces (left and right columns respectively) for a fluid pressure pulse due to a collision of two 4.5 mm glass particles in water.

Appendix B. Notes on the dependence of particle properties on the duration, maximum pressure and impulse of a collision

Based on the Hertzian theory of contact, a simple analysis is followed to show how the collision pressure, duration of collision and the collision impulse depend on the properties and size of particles.

The Hertz law of contact is a force-deformation relation which describes the static compression of two isotropic elastic bodies whose surfaces are perfectly smooth and can be approximated by two paraboloids in the vicinity of the contact point. The impact of spheres can be modeled based on the Hertzian law providing the contact process can be assumed to be quasi-static. Figure B.5 shows a sketch of the impact problem. As soon as the spheres, in their motion towards one another, come into contact at point O, the compressive forces F begin to act and therefore change the velocity of the spheres. Since the force-displacement expressions are known from the Hertzian analysis, the particle deceleration during impact can be obtained:

$$\ddot{\alpha} = -F/m_* \tag{B.1}$$

where α is the displacement, F is the compressive force and m_*, the average mass ($m_* = (m_1 m_2)/(m_1 + m_2)$). After some manipulation (see Johnson (1987) for details) it can be shown that the maximum compression force during impact

$$F_m = N\left(\frac{5m_* u_i^2}{4N}\right)^{3/5} \tag{B.2}$$

where u_i is the impact velocity and N is

$$N = \frac{4}{3\pi}\frac{1}{k_1 + k_2}\sqrt{\frac{a_1 a_2}{a_1 + a_2}}$$

where k_j is a parameter that groups the elastic properties of sphere i (see equation

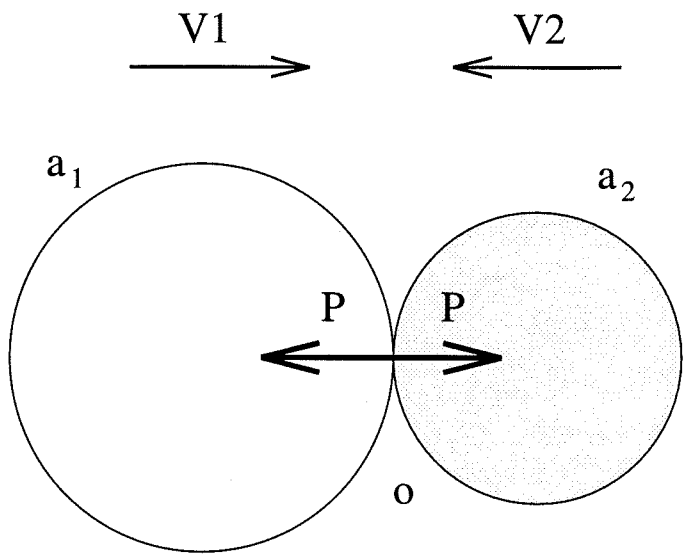

Figure B.5: The Hertz impact problem, $u_i = V_1 - V_2$.

2.13). The duration of collision is given by

$$\tau = 3.21 u_i^{-1/5} \left(\frac{m_*}{N}\right). \tag{B.3}$$

The collision impulse (as defined in equation 2.10) is

$$I = 2.047 u_i m_*. \tag{B.4}$$

Duration of collision

Comparing the case of a collision of two particles with the same diameter and properties with the case of a particle colliding against the wall at the same velocity, the following ratio can be formed:

$$\frac{\tau_{p-p}}{\tau_{p-w}} = 0.871 \left(\frac{k_p + k_p}{k_p + k_w}\right)^{2/5} \tag{B.5}$$

where the subscript p denotes the particles and w the wall. Three cases can be considered:

- Particles and wall with the same elastic properties

$$\frac{\tau_{p-p}}{\tau_{p-w}} = 0.871$$

which implies that a collision between identical spheres has a duration which is 13% shorter than in the case of a sphere colliding with a wall with the same properties.

- The wall is much more stiffer than the particles. In such a case $E_w \gg E_p$, which implies that $k_w \ll k_p$, and therefore

$$\frac{\tau_{p-p}}{\tau_{p-w}} = 1.148$$

implying that a particle to particle collision is 15% longer than that of a particle with the same properties colliding against a rigid wall.

- The particle is stiffer than the wall. For $E_w \ll E_p$, $k_w \gg k_p$, thus

$$\frac{\tau_{p-p}}{\tau_{p-w}} = 0.871 \left(\frac{2k_p}{k_p + k_w} \right)^{2/5}$$

in which case if

$$k_w = 2k_p \Rightarrow \tau_{p-p}/\tau_{p-w} = 0.74$$

$$k_w = 10k_p \Rightarrow \tau_{p-p}/\tau_{p-w} = 0.44.$$

So, in this case particle-particle contacts are of shorter duration.

Figure B.6 shows the ratio of τ_{p-p} to τ_{p-w} as a function of E_p/E_w.

Maximum compression force

Comparing the maximum compression forces for the same cases as above,

$$\frac{Fm_{p-p}}{Fm_{p-w}} = 0.574 \left(\frac{k_p + k_w}{k_p + k_p} \right)^{2/5}. \tag{B.6}$$

- Particles and wall with the same elastic properties,

$$\frac{Fm_{p-p}}{Fm_{p-w}} = 0.571$$

- $E_p \gg E_w$, particle more stiffer than the wall,

$$\frac{Fm_{p-p}}{Fm_{p-w}} = 0.574 \left(\frac{k_p + k_w}{k_p} \right)^{2/5}$$

for

$$k_w = 2k_p \Rightarrow Fm_{p-p}/F_{p-w} = 0.675$$

$$k_w = 10k_p \Rightarrow Fm_{p-p}/F_{p-w} = 1.135$$

- $E_p \ll E_w$, particle softer than the wall,

$$\frac{Fm_{p-p}}{Fm_{p-w}} = 0.435$$

Figure B.6 shows the ratio of Fm_{p-p} to Fm_{p-w} as a function of E_p/E_w.

Collision Impulse

Note that the collision impulse is independent of the elastic properties of the contacting surfaces. Therefore,

$$\frac{I_{p-p}}{I_{p-w}} = 0.5. \tag{B.7}$$

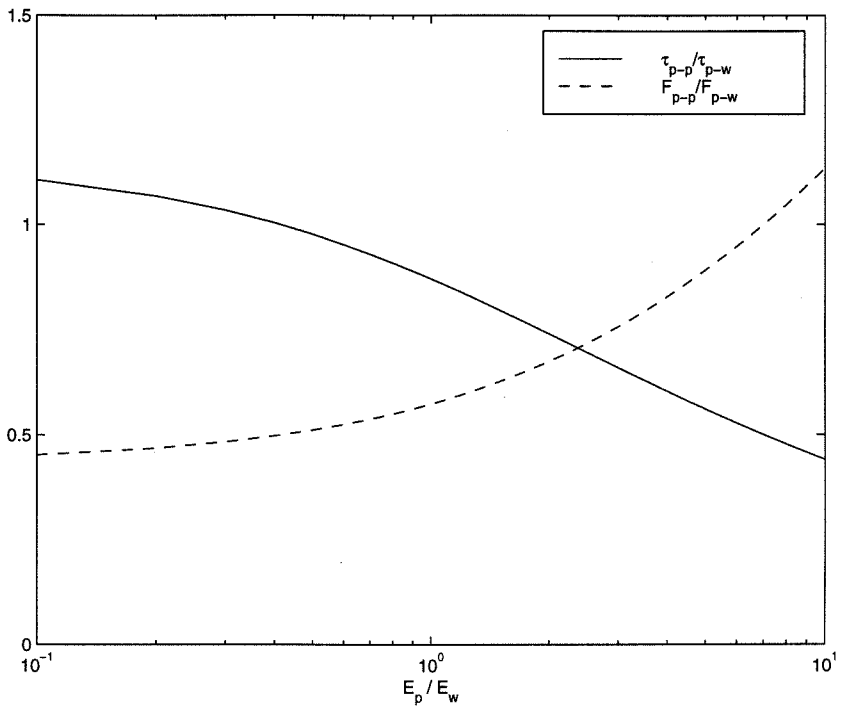

Figure B.6: Ratio of duration of collisions, τ_{p-p}/τ_{p-w}, as a function of ratio of elastic properties, E_p/E_w (solid line), and ratio of maximum compression forces F_{p-p}/F_{p-w} as a function of ratio of elastic properties (dashed line).